PRODUCTION OF CHARM MESONS BY HIGH ENERGY NEUTRONS

BY

CALVIN LEROY SHIPBAUGH

B.A., Rice University, 1980
M.S., University of Illinois, 1982

THESIS

Submitted in partial fulfillment of the requirements
for the degree of Doctor of Philosophy in Physics
in the Graduate College of the
University of Illinois at Urbana-Champaign, 1988

FERMILAB LIBRARY

Urbana, Illinois

PRODUCTION OF CHARM MESONS BY HIGH ENERGY NEUTRONS

Calvin Leroy Shipbaugh, Ph.D.
Department of Physics
University of Illinois at Urbana-Champaign, 1988

The charmed mesons $D^{*\pm}$, D^0, and $D_s^{\pm}$ have been observed in neutron-nucleus collisions at the FNAL Tevatron. A sample of 134 ± 19 events was investigated in the decay $D^{*\pm} \rightarrow D^0\pi^{\pm}$ with the subsequent decay mode $D^0 \rightarrow K^+K^-$. The cross section per nucleon for $D^{*\pm}$, at most probable energy $\sqrt{s} = 35$ GeV, was measured to be:

$$\frac{d\sigma(\bar{x}_f)}{dx_f} \cdot BR \;=\; 2.11 \;\pm\; .43\,(\pm .63)\mu\text{b/nucleon}$$

for $0.0 < x_f < 0.14$ ($\bar{x}_f = .07$). The branching ratio (BR) is defined as:

$$BR \equiv BR(D^* \rightarrow D\pi) \times BR(D \rightarrow K^+K^-).$$

The dependence of the cross section per nucleus on number of nucleons in the target was fit to a form A^{α} and it was found that $\alpha = .96 \pm .17$. A sample of 64 ± 16 $D_s^{\pm}$ events was investigated for the decay $D_s^{\pm} \rightarrow \phi\pi^{\pm}$. The differential cross section for $D_s^{\pm}$ production averaged over the particle and antiparticle states is:

$$\text{BR} \cdot \frac{1}{2}\left(\frac{d\sigma(D_s^+)}{dx_f} + \frac{d\sigma(D_s^-)}{dx_f}\right) = 2.85 \pm 0.80 \;\pm .86\ \mu\text{b/nucleon at } x_f = 0.175$$

where the first error is statistical and the second error is systematic. The branching fraction is defined as $BR \equiv BR(D_s \rightarrow \phi\pi)$, and a linear A dependence was assumed. An estimate of relative cross sections is:

$$\frac{\frac{d\sigma}{dx_f}(D_s)}{\frac{d\sigma}{dx_f}(D^*)} = 0.19 \pm 0.09 \text{ at } x_f = 0.$$

ACKNOWLEDGEMENTS

Hadronic charm measurements reveal much about QCD. The analysis of charm physics was the primary E400 objective, and the use of a hadronic beam made the investigation quite involved. E400 was a collaboration of numerous individuals. Although I cannot herein explicitly credit all who participated in the experiment, I wish to acknowledge in this section those from E400 who were specifically involved with that part of the charm effort connected with this thesis.

I foremost thank my advisor, and spokesman for the experiment, Jim Wiss. His experience made possible a large number of accomplishments by E400, such as the $D_s^{\pm}$ research. I feel inclined to point out that the good results of this thesis are a reflection of his advice; I take sole responsibility for any flaws that may remain in the thesis.

John Cumalat made the world's first observation of the very interesting decay mode $D^0 \rightarrow K_s^0 K_s^0$. Mike Diesburg measured a distinct D^0 mode which helped to confirm the cross section of the modes I studied. Jean Slaughter gave me guidance on the repair of hadron calorimeters.

I commend my fellow UI students for their dedication to science. They chose to help uphold the E400 prime directive and help make E400 a success even at the personal sacrifice of quick degrees. The UI graduate students, prime movers in everything from on-line programming to repairing the detector hardware to analysis and charm studies, are paragons of what research assistants should be. I am indebted to Tom Kroc for his careful analysis of the magnetic fields and work on the Monte Carlo event generator. John Filaseta, now an assistant professor at Northern Kentucky University, contributed greatly to the on-line data acquisition and the mapping of the magnetic fields.

He originated several bright concepts which the group explored during the analysis – in fact, he was the first E400 researcher to find and study charm baryon production. I thank the elder Illinois graduate students who showed me the ropes when I began research in high-energy – Mike Lamm, Chris Olszewski, Paul Nienaber, and Sam Denham. I am also glad to have had the opportunity to have worked with Glen Jaross and Karen Lingel.

I thank Jerry Wray and Dave Lesny for operating a highly efficient and user-friendly system for the UI high energy group. I also thank Betty Chu for her role in maintaining operations. I give recognition to the efficiency and helpfulness of the office personnel, Jeannine Adomaitis and Deborah Oberg. I recognize the support I was given by the rest of the high energy faculty and staff during the time I was performing this thesis.

I give thanks to those who have given me support and friendship over the years. I give my appreciation above all to Khadija Zizi, who is bright, charming and earned her Ph.D. in a dazzling, short time. Her combination of wit and wisdom provided inspiration and insight. I also pay respects to several others – Pat Goalwin, Craig Gustafson, Nalini Rau Murthy, Pete Nelson, Paul Pachura, Mike Rugg, Robert Smet, Randy Smith, and Howard Teems. I remember the teachings of Robert Diffenbaugh, James Ferguson, Max Fordyce, and Wally Stoffel. This thesis is a reflection of the many years of support given to me by my relatives, especially my parents Paul and Marguerite; I have a special memory of the little whiskered ones – Dinah, Sam, and Tom.

This research was funded in part by the U.S. Department of Energy under contract DE-ACO2-76ERO-1195.

TABLE OF CONTENTS

page

CHAPTER 1. Introduction 1

CHAPTER 2. The Experiment 11

2.1 Introduction 11

2.2 The Beam and Target 12

2.3 The Detector 14

2.4 The Čerenkov Counters 17

2.5 The Trigger 19

CHAPTER 3. Data Reduction 35

3.1 Introduction 35

3.2 Tracking and Vertexing 36

3.3 Particle Identification and Čerenkov Analysis 40

3.4 Physics Reduction 47

CHAPTER 4. The $D^{*\pm}$ Signal 58

4.1 Introduction 58

4.2 The Monte Carlo 60

4.3 Determination of the Nuclear Dependence 64

4.4 Determination of the $D^{*\pm}$ Cross Section 65

CHAPTER 5. The $D_s^{\pm}$ Signal 80

5.1 Introduction 80

5.2 Monte Carlo Results 81

5.3 Determination of the $D_s^{\pm}$ Cross Section 84

5.4 Comparison of the $D_s^{\pm}$ with other Charm Mesons 86

5.5 Correlation of the $(\phi\pi^+)$ Submass with Antiprotons . . . 88

CHAPTER 6. Conclusions 108

APPENDIX A. Calculation of the Čerenkov Light Function . . 116

APPENDIX B. Calculation of the E400 Cross Section 124

APPENDIX C. Calculation of the $D_s^{\pm}$ Angular Distribution . . 131

REFERENCES 132

VITA 134

CHAPTER 1

Introduction

The existence of the charm flavor of quark was first proposed in 1964, shortly after Gell-Mann and Zweig introduced the quark model to explain the growing spectroscopy of known mesons and baryons. Bjorken and Glashow proposed[1] the existence of a fourth quark on grounds of symmetry – four quarks to complement the four leptons known at the time. The charm quark was given firmer theoretical ground in 1970 by Glashow, Iliopolous, and Maiani (GIM theory[2]), which used the property of charm to explain the absence of strangeness-changing neutral currents. Charm was observed[3,4] in 1974 in the form of a charm-anticharm quark dubbed the J/ψ. In 1976, open-charm was observed[5].

I have chosen to investigate several properties of certain charm particles. These properties will include measurements of the charm cross section, consistency comparisons of the various cross sections, dependence of the cross section on nucleon number of the target, and the ratio of particle to antiparticle. I will now motivate my choices of charm particle measurements.

There is a considerable amount of theoretical uncertainty about the production of charm particles in hadronic beams. According to hard parton collision models fusion takes place between a parton in the incident neutron and a parton in one of the nucleons in the target nucleus. In this model[6] QCD matrix predictions for the cross section depend on the charm quark mass, center of mass energy of the fundamental subprocess involved, and the parton distributions within the nucleus. This will be elaborated on in Chapter 4 when a discussion of the Monte Carlo is given. One of the fundamental cross sections involves fusion of a gluon from the target and a gluon from the projectile nucleon. This is known as gluon-gluon fusion, and has

the three Feynman diagrams shown in Figure 1.1(a). Cross section predictions for the gluon-gluon model are given in reference 7. There can also be a low order process which is quark-antiquark annihilation, shown in Figure 1.1(b). It is anticipated that at high energy the gluon-gluon fusion process will dominate over the quark-antiquark process, because at high s the parton distribution can reach low x and still be above charm production threshold. At low x the number of gluons should dominate the number of quarks (because of the effect of conserving color charge when creating parton pairs in the sea) and thus g-g fusion should dominate the cross section.

There are also models in which the charm quarks are "intrinsically" part of the nucleon (Brodsky's intrinsic charm model), and mixtures of the intrinsic and parton-parton models. Such an idea attributed to Bjorken is that a charm quark might be produced centrally by parton-parton collisions and then stick to valence quarks in the projectile and target, creating higher x_f than in straight gluon-gluon fusion.

The parton-parton models should have a cross section dependence on the atomic weight that goes like A^1 if it is assumed that there is the same number of partons (gluons or quarks) in each nucleon. With this assumption, if the neutron is incident on a target with A nucleons per nucleus then there are A times as many partons to interact with so the cross section should increase linearly with A. This is to be contrasted, for instance, with the geometrical dependence of $A^{2/3}$ (from crudely assuming a constant density nucleus) which is generally observed in high energy diffractive cross sections. There is also the possibility of anomalous A-dependence in which the exponent can even exceed a value of one. Thus, the A-dependence of charm production is of theoretical interest for the purpose of comparing production models. It is also necessary for the experimentalist to know the A-dependence to determine the cross section per nucleon.

A large motivation to studying charm hadroproduction cross sections comes from the desire to compare production models. I observe cross sections that are an order of magnitude larger than those reported by LEBC[8], and the typical gluon-gluon model predictions. I must add that my cross sections are measured with the assumption that the A-dependence is linear (which is consistent with my measurement of the A-dependence). Even a ten percent variation of this assumption can result in a 30 % variation in the cross section. If the A-dependence is anomalously high, then the cross sections are lower than I report. If the A-dependence has a value of less than one for the exponent, on the other hand, the cross sections are larger than I report. Results from the ISR[9] indicate large cross sections for charm baryon production. Since, generally speaking, mesons are produced more copiously than baryons these experiments also appear to be inconsistent with LEBC.

I must also note that it is necessary to know the particle to antiparticle ratio when measuring them together and reporting on the cross section for a particular choice of sign. This value is also of interest simply because we use a beam consisting of particles (neutrons produced by protons) rather than a mix of particles and antiparticles. These ratios are good to know because if the production is found to be symmetric then valence effects which could discriminate between the charm and anticharm quark are not important.

The production of charm mesons is interesting, and I choose to study mesons rather than baryons.

Figure 1.2(a) shows a quark diagram representing the decay $D^0 \rightarrow K^-\pi^+$. This is said to be a Cabibbo-favored process because the angle θ_C (known as the Cabibbo angle), which measures the mixing of different quark flavors, has a measured value of .23 radians and thus the factor $\cos\theta_C$ which relates the decay of a charm quark to a

strange quark is greater than the factor $\sin\theta_C$ which relates the relatively suppressed decay of a charm quark to a "d" quark.

In addition to the Cabibbo-favored decay mechanism, the D^0 can also decay by the Cabibbo suppressed mechanisms, represented by Figures 1.2(b) and 1.2(c), into a pair of oppositely charged pions or kaons. These latter two decay modes are expected to be less probable than $\bar{D}^0/D^0 \to K^{(+/-)}\pi^{(-/+)}$ by the identical factor $\tan^2\theta \approx .05$ in each case if SU(3) symmetry is exact. However, when these states were first observed by MARK II it was learned that the relative ratios were:

$$\frac{\Gamma(D^0 \to K^+K^-)}{\Gamma(D^0 \to K^-\pi^+)} = 0.122 \pm 0.018 \pm 0.012$$

and

$$\frac{\Gamma(D^0 \to \pi^+\pi^-)}{\Gamma(D^0 \to K^-\pi^+)} = 0.033 \pm 0.010 \pm 0.006.$$

These observations led quickly to a number of theoretical discussions[10,11,12] of the enhancement of the suppressed $D^0 \to K^+K^-$ decay mode, which primarily were concerned with the implications of final state interactions. This has made it interesting[13] to compare the $D^0 \to K^+K^-$ mode with other Cabibbo suppressed decay modes. This mode is also of experimental interest because it involves two strange particles and is expected to have (and does have) much lower backgrounds than the non-suppressed modes. This makes it an easier mode to see.

I observe a large sample of $D^0 \to K^+K^-$ (135 ± 19 events) by accepting a sample of $D^{*\pm} \to D^0\pi^\pm$. The narrow $D^{*\pm} - D^0$ mass difference provides an analysis cut which strongly enhances the ratio of signal-to-background. Our experiment E400 also has excellent ability to distinguish particle identification by the use of Čerenkov analysis. This enabled me to further enhance the signal-to-noise beyond that of the background formed by the plentiful pions. The relatively large branching fraction for this decay

mode has also fortuitously made it easier to observe a signal than would otherwise have been the case.

With this large sample, I am able to measure the dependence of the hadronic cross section on the atomic weight of the target. I am also in a position to compare my observation with that of another E400 researcher[14], who has observed the Cabibbo-suppressed decay $D^0 \rightarrow K_s^0 K_s^0$ by also taking advantage of the $D^{*\pm} - D^0$ mass difference. The $D^0 \rightarrow K^0 \bar{K}^0$ decay channel is of particular interest because it is expected to occur primarily via the W exchange diagrams shown in Figures 1.3(a) and 1.3(b). The Cabibbo factors for these two diagrams have the opposite sign which might lead to a partial cancellation of the two amplitudes and thus a small width for $D^0 \rightarrow K^0 \bar{K}^0$. In particular, the ratio $\frac{\Gamma(D^0 \rightarrow K^0 \ \bar{K}^0)}{\Gamma(D^0 \rightarrow K^+ K^-)}$ has been predicted by Pham[15] to be 0.5 due to the effects of final state rescattering.

I am able to evaluate $\sigma \cdot BR$ for the hadroproduction of the $D^{*\pm}$. If I use the accepted value[16] for the branching fraction of $D^0 \rightarrow K^+ K^-$, I can provide an estimate for the total cross section. I am encouraged by this value, because it is consistent with the preliminary findings of another E400 researcher[17] who has been studying the more copious $D^0 \rightarrow K_s^0 \pi^+ \pi^-$ with the $D^{*\pm} - D^0$ mass difference cut.

Note that the original observation of the Cabibbo-suppressed decay $D^0 \rightarrow K^+ K^-$ (made by MARK II[18] in 1979) reported 22.1 $\pm$ 5.2 events. Although this is small, in order to observe this decay mode it is necessary to have a large sample of D^0's and the ability to distinguish between charged pions and kaons. The other major observation[19] of this charm decay mode was reported by MARK III in 1985. They observed 118 $\pm$ 15 events, which is a sample size close to the 135 $\pm$ 19 events I report observing. There have been no clear reports for hadroproduction of this mode.

I have also chosen to report on the observation of a sample of $D_s^{\pm}$'s containing 64

$\pm$ 16 events. This is certainly not the strongest such signal seen, but previous reports of this signal in hadroproduction have been much weaker.

This observation is the first statistically strong evidence for $D_s^\pm$ hadroproduction. With this observation I can make comparisons of the relative production rates ($\sigma \cdot BR$) of strange and non-strange charm mesons. Although I do not consider the branching ratio for $D_s^\pm \rightarrow \phi\pi^\pm$ to be well-established, if I use the current best-estimate value of 3.6 % I can estimate the value of the ratio and provide a crude estimate for the total $D_s^\pm$ cross section for hadroproduction.

This is not a Cabibbo suppressed decay, but I can make a comparison of the cross section described above for $D_s^\pm$ production with that for $D^{*\pm}$ production. This ratio is of interest, for instance, in comparing with the result found from other production mechanisms (e.g., e^+e^- annihilation). Bjorken has suggested this ratio is a feasibility measurement for whether hadronically produced $D_s^\pm$'s can be used as a factory for the production of tau neutrinos from $D_s^\pm$ decays.

The first clean observation of the $D_s^\pm$ was made in 1983 by CLEO[20]. That collaboration observed 104 ± 19 $D_s^\pm \rightarrow \phi\pi^\pm$ events at a mass of $1970 \pm 5 \pm 5$ MeV/c^2. Subsequent observations[21,22,23,24] have confirmed that this is the correct mass value for the $D_s^\pm$.

The CLEO analysis used two key features which I also must demand:

(1) A clear ϕ signal was demonstrated.

(2) The spin of the ϕ is one, but its component along the axis defined by the π direction is zero in the ϕ rest frame, as is described in Appendix C.

CLEO was conducted in e^+e^- annihilation. Until now there has been no strong observation[23,24] of $D_s^\pm$ production with a hadronic beam. The ACCMOR report[24]

involved only three events, and LEBC has only presented a limit[25]. Although I am reporting on the most commonly observed decay mode of the $D_s^{\pm}$, the branching fraction for this decay mode is not well determined. It is not well determined primarily because there are no established resonances in e^+e^- that go exclusively into $D_s^+D_s^-$. The current world average value is given as 3.6 %, but it should be noted that TASSO[22] has reported a high value of 13 ± 5 %.

Because we observe a $D^{*\pm}$, $D_s^{\pm}$, and (a much weaker) $D^{\pm}$ signal it is possible under certain assumptions (see chapter 6) to estimate what part of hadronic production into charm mesons is through production of $D^{*\pm}$'s and what part through direct production of $D^{\pm}$'s. This value can be compared to values obtained in other beams, such as e^+e^- annihilation.

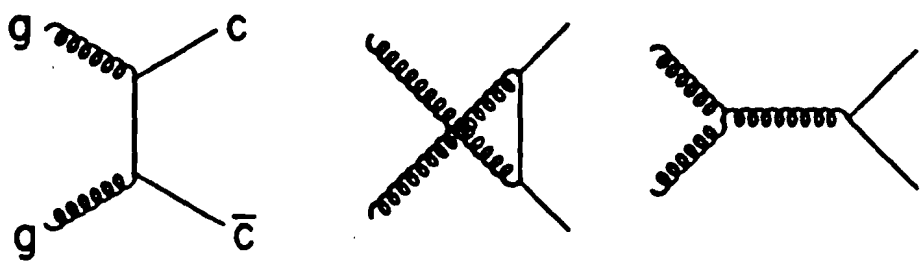

(a)

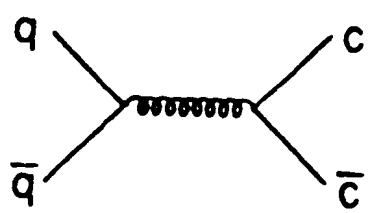

(b)

Figure 1.1 Lowest-order QCD diagrams:

(a) are gluon-gluon fusion diagrams, and (b) is quark-antiquark annihilation.

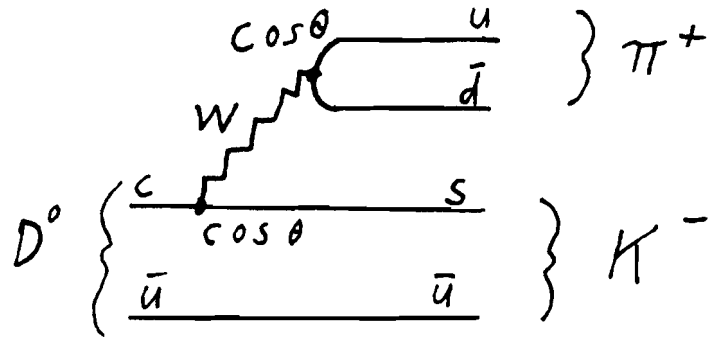

(a)

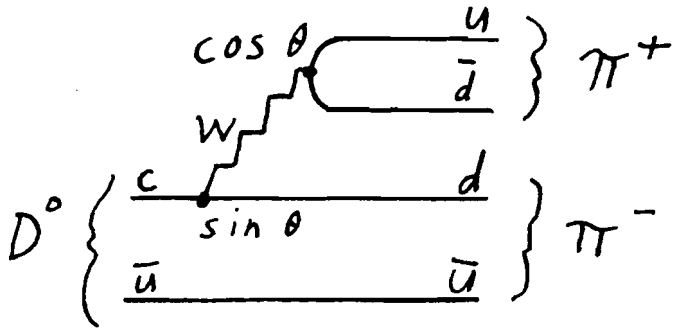

(b)

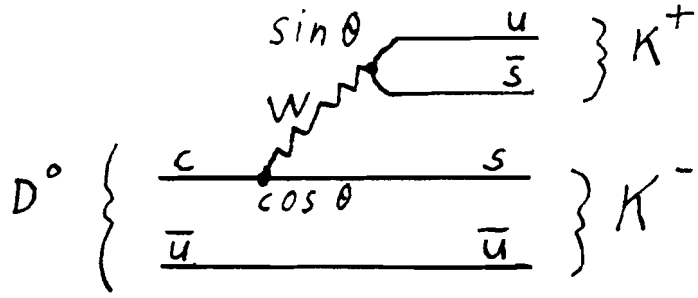

(c)

Figure 1.2 Quark diagrams for D^0 decay modes.

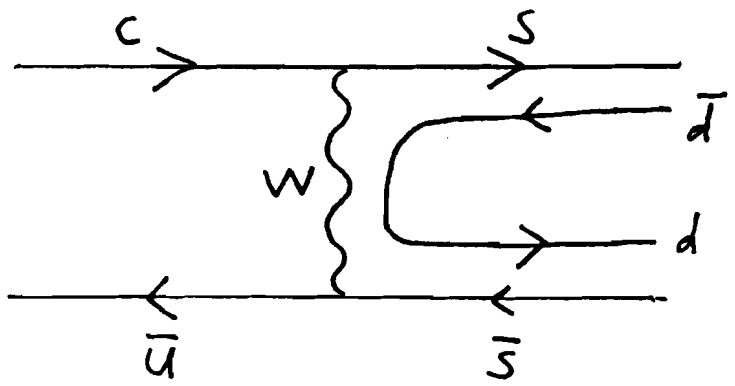

(a)

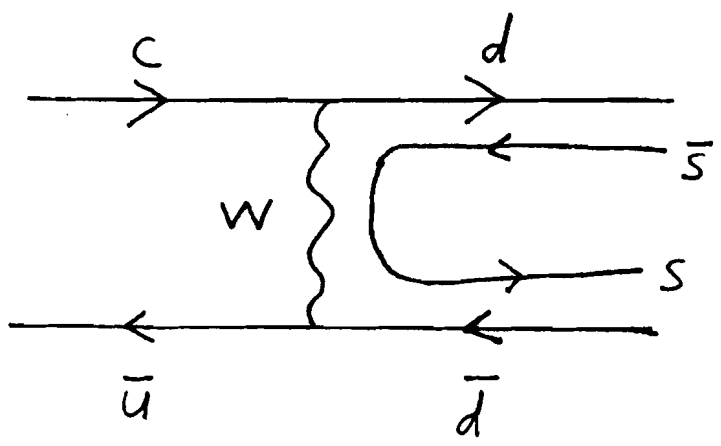

(b)

Figure 1.3 Quark diagrams for W exchange of $D^0 \to K^0\bar{K}^0$.

CHAPTER 2

The Experiment

2.1 Introduction

Experiment E400 at Fermi National Accelerator Laboratory was conducted at the site of the broad-band neutral beamline known as Proton East. The experiment was proposed originally in 1975, after the discovery of the J/ψ in 1974. The goal of E400 was to search for particles produced in association with the J/ψ. By Zweig's rule, it was expected that particles produced in association with the J/ψ might be charmed. E400 goals included a measurement of the inclusive properties of charm production such as the Feynman-x and $P_\perp$ distributions.

It was expected that hadronic charm would have large backgrounds, so devices were required to isolate charm events from ordinary hadronic events. One of the methods for charm enhancement exploited the fact that charm would decay in such a way as to include kaons rather than just pions, thus E400 had strong Čerenkov identification to separate kaons from pions. Another method used to achieve charm enhancement exploited the finite lifetime of charmed particles. E400 built a vertex chamber with sufficient resolution to allow the decay products of charm secondaries to be distinguished from the primary vertex. Because hadronic charm events have high multiplicities, it was necessary to build all the detectors with high granularity.

Several experiments were conducted in Proton East immediately prior to the engineering run of E400 (October 1981 to May 1982), and these established the arrangement of the E4XX spectrometer. After analyzing the performance of the detector by use of preliminary data collected from the engineering run, E400 was ready to obtain its large data set beginning November 1983. The Tevatron first came on-line in February 1984, and E400 continued to collect data until the end of the run in June

1984. Three data reduction passes were then conducted until July 1986, and then charm analysis studies followed.

2.2 The Beam and Target

The beam used in E400 consisted primarily of neutrons. Following the encouraging success of the precursor photoproduction experiment E87 at detecting open-charm, E400 was ready to begin a statistical study of charm hadroproduction. The goals included not only a measurement of the relative cross sections of various species, but also a decision to include a target consisting of several distinct pieces with differing atomic weights. The purpose of the segmented target was to provide a measurement of the A dependence of hadronically produced charm cross sections.

The neutrons were produced as secondaries from interactions of the 800 GeV proton beam supplied by the Tevatron with a beryllium production target located 500 feet upstream of the E400 experimental target. A schematic of the beamline is shown in Figure 2.1. The general production mechanism is considered to be a diffractive charge exchange of the incident proton with a target nucleus. The resulting neutron spectrum thus had a maximum of 800 GeV, and was found to have a peak energy of 640 GeV with a roughly triangular shape shown in Figure 2.2.

Lead flippers of one radiation length were used to attenuate the photon component to the neutral beam. Because the interaction length of lead is greater than the radiation length, the photons are degraded in energy by conversions at a faster rate than the neutron loss. There were six of these flippers inserted under conditions of smooth data taking for the 800 GeV run. The photons produced an e^+e^- shower, and bending magnets steered the pairs away from the direction of the experimental target. The photons which emerged from the shower were not only spread out to large angles, but were of relatively low energy. A minimum energy trigger was used to eliminate events these photons could have caused.

Collimators were used both before and after the lead flippers to direct a neutron beam with a divergence of the order of tens of microradians onto our experimental target. This typically resulted in a lateral spread on the order of a centimeter. The remaining halo to this central beam consisted of muons from upstream meson decays, low energy photons from π^0 decays, and a sample of the relatively long lived K_l. The K_l spectrum has been previously measured[26] and compared with the neutron spectrum. The K_l's are of lower typical energy than the neutrons and were reduced by the minimum energy threshold to a few percent of the beam.

The experimental target shown in Figure 2.3 was composed of three segments – tungsten, silicon, and beryllium. Table 2.1 shows the thickness, amount of radiation length, and amount of neutron absorption lengths of the three segments. These segments are separated by approximately 2.5 cm each. The tungsten target introduced the greatest amount of radiation length, so to minimize the problem of multiple coulomb scattering (which makes it difficult to trace particles back through the detector to their origin) the tungsten was placed on the upstream end of the target.

There was an additional thin segment of Si (600μm) placed on the most downstream end of the target such that the beryllium target was sandwiched between the two silicon segments. This thin segment, called Si33, was designed to be incorporated as part of the trigger requirement for selecting an event. Its function was to detect tracks coming from the target. Si33 was divided into three longitudinally segmented slabs. The larger Si target was divided into 10 longitudinally segmented slabs, all of equal thickness. Each slab acted as a semiconductor detector for measuring multiplicity by a pulse height analysis of the energy deposited. The individual slabs were also segmented transversely into four parts in order to reduce the noise (capacitance per slab). The original purpose of this "active" target was to aid in the identification of the location of the secondary charm vertices by noting which slabs, if any, experienced

an increase in multiplicity, according to the pulse height analysis. This pulse height information was not used, because the overall event multiplicity (15 charged particles) was so high that the increase of two or three tracks in the multiplicity from a typical charm decay was not sufficiently striking to resolve the presence of charm in an event for various technical reasons (e.g., wide angle tracks strike only the first couple of slabs).

2.3 The Detector

I will describe the coordinate system of the detector in terms of the system used in the analysis. Z denotes the direction of the incident beam. Y points vertically up, while X is a horizontal direction such that X, Y, and Z form a left-handed coordinate system. Figure 2.4 shows the detector components in this system from the "top" view, or X (non-bend) view. Figure 2.5 shows a view from the side, or the Y (bend) view. Table 2.2 gives the location of the individual devices (with respect to an arbitrary origin chosen to be at the center of the most downstream magnet, M2). The detector had an acceptance in the forward direction with the aperture of M1 limited to accepting tracks in the X view within $\pm$ 100 milliradians and in the Y view within $\pm$ 200 milliradians. M2 is restricted to tracks in the X view falling within $\pm$ 40 milliradians and $\pm$ 50 milliradians in the Y view.

The detector consisted of an active target, secondary vertex detector, magnetic spectrometer, gas Čerenkov system, several banks of scintillation counters, electromagnetic and hadronic calorimetry, beam dump, and proportional counters. Immediately following the target region was the vertex detector consisting of nine planes of multi-wire proportional chambers (MWPC's), with 250 μm wire spacing in three views which differ from one another by a 60° rotation. The center of this MWPC device was located 4.688 inches downstream from the center of the beryllium segment of the experimental target. The main magnetic spectrometer consisted of two analyz-

ing magnets with three stations of MWPC's between the magnets and two stations of MWPC's following the second magnet. The calorimetry devices followed the final main spectrometer wire chamber. A concrete and steel beam dump after this stopped all particles except muons, which could then be detected by two banks of proportional counters and two hodoscopes of horizontal and vertical scintillation counters.

The high resolution MWPC (D5) was known as a vertex detector because it allowed tracks to be extrapolated with a 60 μm transverse root-mean-square error and a Z-direction error (for a typical 50 GeV/c particle) of 1.5 millimeters, which is typical of decay distances expected for the short lived charm particles and could thus be used to isolate the secondary vertices of charm particle decays from the vertex of the primary nuclear interaction. This type of lifetime analysis was applied to previously published charm baryon states, but was not necessary to isolate the charm meson states covered in this thesis.

The five main MWPC's (P0 - P4) had two-millimeter wire spacings (P3X had three millimeter spacing), and consisted of three views each. Each wire chamber had one view in which the individual wires ran vertically (X plane – the non-bend view), and two stereo views in which the individual wires were at a small angle inclined either above or below the positive horizontal direction (V, U planes) which gave information in the bend view. In our coordinate system, one could then find an individual X-Y position in terms of a linear combination of the number of wire spacings by counting which wire in U and which in V was "on", and adjusting for the view by the inclination angle θ, where $\tan\theta = 0.2$. A program called the reconstruction program looked for straight line projections in X, and kink projections (because of the magnet) in U and V. Linear combinations of U and V projections were used to find Y projections. The U and V projections which were orthogonal to this gave information that could be compared to the X wire information to find tracks which were matched in all three

projections (to eliminate false tracks). The reason that high-energy experiments often use three views instead of two mutually perpendicular views is that with only two such views it is easier to create spurious hit ("on") locations and confuse the pattern recognition.

The individual wire locations of MWPC hits were read out for detailed off-line track reconstruction, but bands of wires were read out by the "or" of individual wires within a band for quick on-line tracking for trigger decisions. There were 32 bands per plane of variable width depending on track density – there were eight wires per band in the central region. The read-out was sent to a Time to Digital Converter, which then were recorded in a system of Time Recorder Modules (TRM's).

The downstream magnet was used to bend particles that had been deflected to outward trajectories back into the fiducial volume of the detector. The magnet kicks were adjusted so that the system is dispersionless (track X-Y location doesn't depend on momentum, just on angle) near P4. In particular, the two magnets have opposite polarities and impart transverse kicks of .4 and .58 GeV/c to charged particles traversing their length. The small angle approximation gives the bend angle $\delta\theta$ in terms of the momentum p and the "kick" by:

$$\delta\theta = \frac{kick}{p} \tag{1}$$

The more downstream magnet, M2, was located 250 inches downstream of the experimental target to allow neutral kaons and lambdas space in which to decay.

The neutron energy was obtained by summing the output of the three calorimeters. The front calorimeter was a 22 radiation length array of 120 lead glass blocks to measure electromagnetic energy. Immediately following was a second calorimeter of six absorption lengths of steel and scintillator to measure hadronic energy. Both detectors contained a beam hole of approximately 3.8 cm radius. The summed re-

sponse of these calorimeters formed the minimum energy trigger which eliminated the K_l contamination from the beam. A third calorimeter, constructed of six absorption lengths of tungsten and scintillator, was used to measure energy passing through the beam hole but was not used in the trigger.

The lead glass was used to obtain the total event energy by the following expression:

$$E_{TOT} = 1.05 * E_{HAD} + E_{LG} + E_{BD} + 1.5 * E_{STUB} + 10. \text{ (in GeV)}$$

where E_{HAD}, E_{LG}, E_{BD}, and E_{STUB} represent the energy deposited in the hadron calorimeter, the lead glass, the beam dump calorimeter, and the sum of all stub momenta below 25 GeV, respectively. The factor of 1.05 for the hadron calorimeter is a correction for the hadronic energy deposited into the lead glass. E_{STUB} has a factor 1.5 to account for neutral pions. The constant of 10 added takes into account energy lost by particles not accepted past M1.

2.4 The Čerenkov Counters

Charged particle identification in E400 was accomplished primarily by information from three gas-filled threshold Čerenkov counters – C0, C1, C2. These counters were kept at a pressure slightly exceeding one atmosphere to prevent contamination from air. Each counter contained 34 individual cells linked to its own photomultiplier. The pulse outputs were sent to 10-bit ADC's.

Figure 2.6 shows a view of C0 looking down on the beam, and Figure 2.7 shows a view of the C0 cell locations on the mirror plane. The University of Illinois constructed C0, which was placed between P0 and P1 and was thus the only Čerenkov counter which could provide identification for those tracks which were at too wide an angle or too low in momentum to pass the aperture of M2. The individual cells used 10-inch deep light collection cones to collect the Čerenkov light directed at them. The photomultiplier tubes could not be placed in the path of the particles (secondary

interactions, multiple scattering) but were placed on the left and right faces of the counter (with respect to looking in the direction of the beam). C0 was unique due to the presence of a 45° mirror placed on the back (downstream side) with apex in the middle of the counter. The distance from the back plane of C0 to the front was 26 inches, and the distance from the apex of the mirror to the back plane was 14 inches. This caused the depth of radiator to vary from 26 inches at the edge to 12 inches in the middle.

The 16 outer cells contained RCA 4522 phototubes which have a five-inch photocathode which allowed a large collection cone (seven by six inches) to be used in the relatively unpopulated region of C0. The inner region of C0 consisted of 18 cells with X-Y dimensions of four by five inches and four by four inches (for the six cells whose image on the mirror plane border the apex). These used the higher resolution (the one photoelectron peak is resolved better) RCA 8850, which have a two-inch photocathode. This granularity was needed because the central region was hit with more tracks than the outer region.

Before the start of the 800 GeV run the radiator in C0 was switched from Freon-12 to isobutane to reduce the total amount of radiation length of the radiator from 1.58% to .45%. The mylar windows on the end of the counter contributed an additional .24% of a radiation length while the alzac of the mirror contributed .6%. The gas change also had the effect of lowering the pion threshold from nominally 3 GeV/c to 2.8 GeV/c. C0 had the lowest threshold of the three counters, so it could distinguish among the lower energy tracks which strike the M2 aperture.

C1 and C2 were built by FNAL and placed downstream of M2. They were designed with higher thresholds than C0 to discriminate among the higher energy tracks which get all the way through the detector. Figure 2.8 shows their common mirror plane geometry. Figures 2.9 shows the bend and non-bend views of the trigger

counter C2. C2 has 180 inches of radiator consisting of 80 % helium and 20 % nitrogen and has nitrogen flush layer next to the phototubes to prevent the diffusion of the mobile helium atoms into the phototubes (which would cause an afterpulsing contamination). C1 had 68 inches of radiator filled with nitrogen.

C1 and C2 were threshold counters, but instead of using a 45° mirror and light collection cones, they collected their light by a focusing design. Thus, a ring image of photons was projected from an essentially flat mirror onto the photocathode of the phototubes with a radius equal to the Čerenkov cone half-angle times the focal length. For a typical cell in either counter the focal length was roughly 40 inches. In C2 the pion threshold was 10.8 GeV/c, which gave a 13 milliradian Čerenkov cone half-angle for a $\beta = 1$ track and a ring radius of about .5 inches. In C1 the lower pion threshold of 5.9 GeV/c resulted in a ring radius of about one inch due to the resulting larger Čerenkov cone half-angle.

2.5 The Trigger

Because E400 was interested in a wide range of charm spectroscopy and production measurements, the trigger had to be relatively unbiased. Therefore, E400 used a data acquisition system that would quickly record large samples of data and then allow detailed event selection cuts to be performed as desired in an off-line analysis study. The trigger had two stages – a quick Master Gate, and a slower examination of several device ADC's (e.g., the calorimeter). In addition, a charm enhancement trigger known as the M7 was used. This was the slowest trigger.

The first level trigger, the Master Gate (MG), required the presence of an interaction. This was accomplished by requiring that a signal be registered in a scintillation counter T on the upstream side of M1 in coincidence with two distinct signals registered in a hodoscope of scintillation counters just downstream of P4, known as the HxV array.

The port that was used to select the slightly biased, charm enhanced events was known as Pin 4. This pin required that there be at least two tracks in the main spectrometer system, according to the band hits, and a minimum energy sum.

A logic box ("Confusion Logic") compared the output signals from the HxV array with the signal from T. If one and only one of the two scintillation devices was "on", then the Confusion Logic would flag the on-line computer to inhibit the acceptance of triggers until the detectors could recover. If both detectors were signaled "on", then a MG would be sent from Confusion Logic to the on-line computer which would then inhibit further triggers for 300 ns until a more detailed logic (DC logic) analyzed the event.

There were several possible derivable triggers from demanding, vetoing, or ignoring 16 hardware busslines. These triggers were implemented by a device called Pin Logic, in which any of the 16 hardware busslines could have been demanded, vetoed, or ignored. There was, for instance, an energy bussline which was formed from the ADC output of the lead glass and hadron calorimeter which would signal if more than 265 GeV of energy had been deposited in these devices. Another bussline existed which required that Si33 be "on" to ensure an interaction was coming from the direction of the experimental target.

Pin 2 simply required a MG. Pin 4 required the energy bussline mentioned above and a multiplicity bussline. The specific requirement of this minimum multiplicity bussline was that there were at least four band hits in P0, P1, and P2 and at least two band hits in P3 and P4. This high multiplicity requirement was imposed in the 800 GeV.

About 20% of the data was taken at the end of the run with an additional upper multiplicity limit imposed on Pin 4. Specifically, P3 and P4 were required to have fewer

than eight band hits each. This low multiplicity trigger turned out to be effectively set against events with greater than 15 tracks, and was not generally useful in the measurement of charm cross sections. The results I present in this thesis will have cross sections measured using the high multiplicity Pin 4 trigger (whose upper limit is a multiplicity of 19 tracks).

The individual pins were prescaled to pass only a fraction of the events they accepted. It was necessary to set a large prescale (1/128) against Pin 2 in order to choose most of the data to be of the charm enhanced Pin 4 variety (no prescale). In practice, 6 to 7% of the E400 data sample was taken under Pin 2.

A hodoscope of 1/8 inch scintillation counters known as CH2 was added to the downstream side of C2. The active area of the CH2 scintillators matched the geometry of the C2 photocells. CH2 participated in a specialized trigger level controlled by a processor known as the M7. The role of the M7 was to insure that a pattern of wire hits (loosely akin to a track; full track reconstruction is too time consuming to be performed at this level) was not due to a pion that was below threshold, but rather a kaon. This was accomplished by making a crude determination of the pattern momentum using TRM lines. M7 acts as a kaon trigger by looking at coincidence registers to determine if C2 is "off", C1 "on", and CH2 indicates that a track was indeed responsible for this. This required that the TRM information identified the track to have a momentum above 22 GeV/c.

The digitized detector information was stored in four two-megabyte buffers during a spill, and read-out to magnetic tape between spills. E400 collected 4000 events per spill with a duty cycle of about one minute from the accelerator. A 6250 bpi tape was filled in about 20 minutes. The system was controlled by FASTBUS. A more detailed description of the data acquisition system is provided in Tom Kroc's thesis.

Two tape drives were used in the data collection to reduce the loss of beam time from the large volume of tape mounts conducted over the course of the experiment. Including an earlier run, there were 1600 6250 bpi tapes of data collected. Although a low level analysis was begun on this set of data during the run, the data reduction phases required considerable amounts of cpu time. The data reduction is discussed in detail in the next chapter.

Table 2.1 Amounts of target material.

	microns	$\frac{g}{cm^2}$	% absorption length	% X_0
W	300	.58	.21	8.6
Si	2000	.51	.85	2.4
Be	4000	.74	.98	1.1

Table 2.2 E400 geometry.

DEVICE	Z POSITION* (cm)	Z LENGTH (cm)	ACTIVE AREA
D5 Triplet No. 1	6.67	0.82	50 mm x 50 mm
D5 Triplet No. 2	11.91	0.82	50 mm x 50 mm
D5 Triplet No. 3	17.16	0.82	50 mm x 50 mm
T1 Counter	30.48	0.64	7.62 cm x 7.62 cm
M1 Magnet	132.3	101.6	38.1 cm x 84.0 cm
M1 Plate Hole	50.54	12.7	35.6 cm x 20.3 cm
P0 Center	221.5	—	44.7 cm x 70.4 cm
P1 Center	307.8	—	49.0 cm x 78.2 cm
C0 Center	381.0	66.1	71.1 cm x 91.5 cm
P2 Center	443.5	—	76.7 cm x 112.8 cm
OE Counter	504.7	55.9	112 cm x 142 cm
OE Hole	504.7	55.9	50.8 cm x 35.56 cm
M2 Magnet	632.5	182.9	50.8cm x 61.0 cm
Oμ Counter	758.8	0.64	152.4cm x 185.4 cm
Oμ Hole	758.8	0.64	50.8 cm x 61 cm
P3 Center	795.0	—	83.3 cm x 112.8 cm
C2 Center	1045.7	460.0	104 cm x 168 cm
CH2 Counter	1291.6	0.64	104 cm x 168 cm
P4 Center	1320.8	—	100.6 cm x 153.6 cm

* Z position is measured from the Be target center to the device center.

Table 2.2 (continued)

DEVICE	Z POSITION* (cm)	Z LENGTH (cm)	ACTIVE AREA
C3 Center	1437	203	104 cm x 168 cm
H x V Counters	1549	0.64	106.6 cm x 160 cm
LG Device	1592	58.4	107 cm x 167.6 cm
LG Hole	1592	58.4	6.35 cm x 12.7 cm
HC Device	1772	198.7	157 cm x 198 cm
HC Hole	1772	198.7	15.2 cm x 15.2 cm
BDC Device	1901	60	20.3 cm x 20.3 cm
P-Tubes Upstream Bank	2108	10.2	152 cm x 227 cm
μH Counters	2270	0.64	180 cm x 224 cm
P-Tubes Downstream Bank	2353	10.2	152 cm x 227 cm
μV Counters	2376	0.64	180 cm x 224 cm

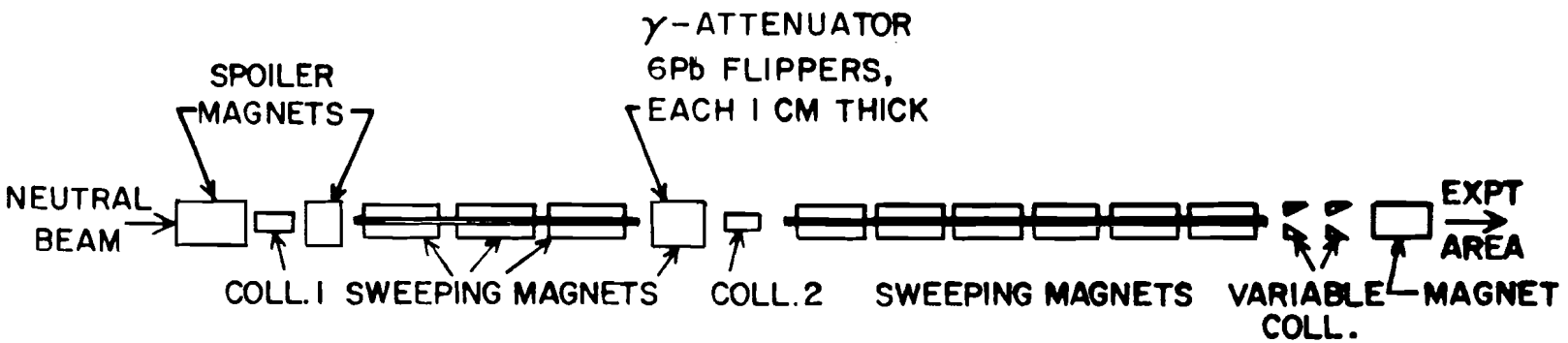

Figure 2.1 The beamline.

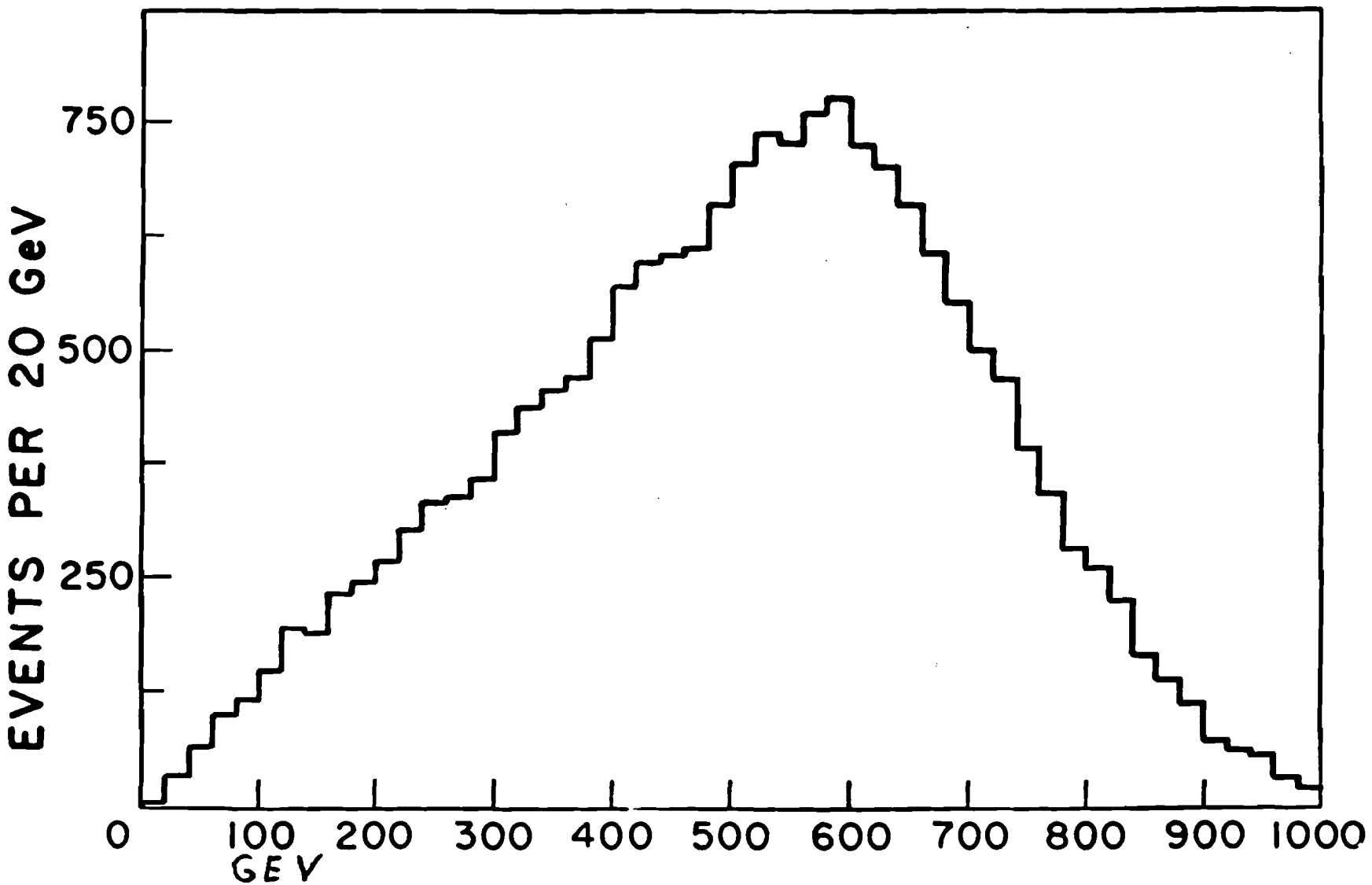

Figure 2.1 The beamline.

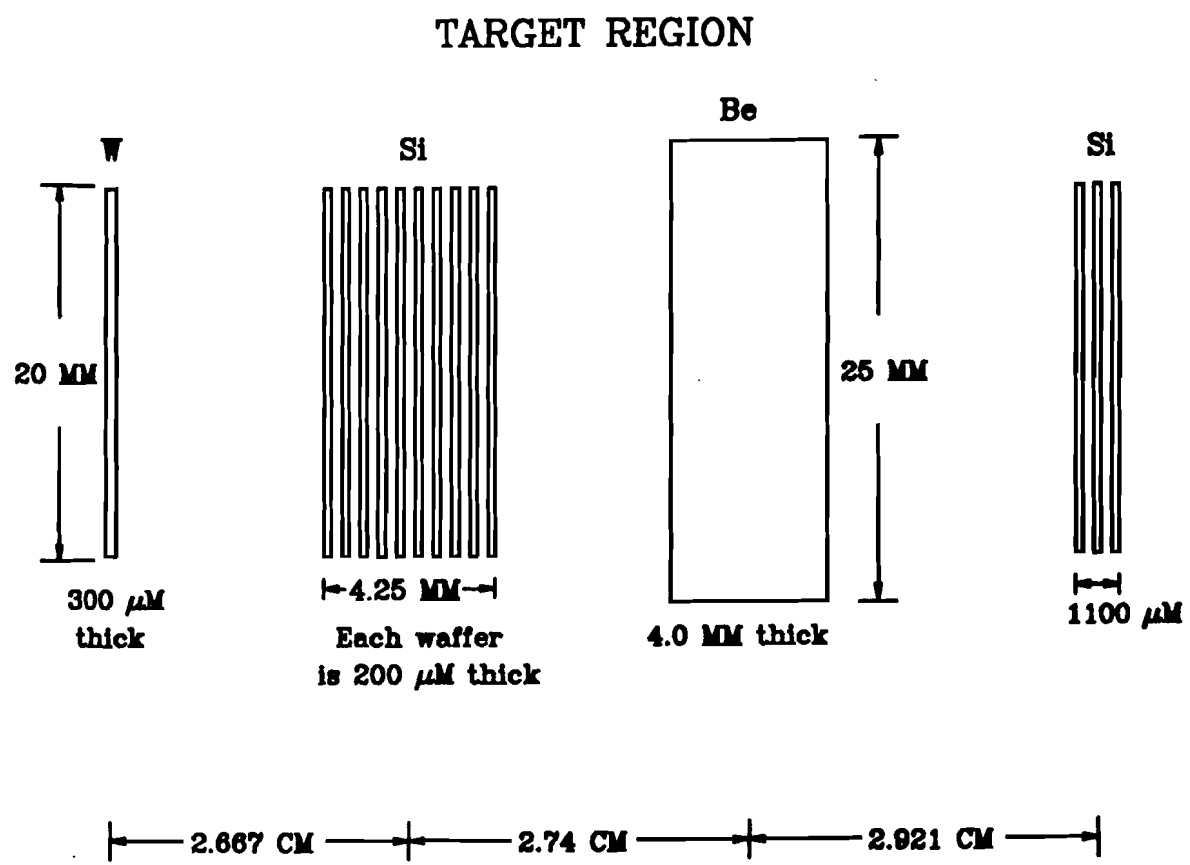

Figure 2.3 The target.

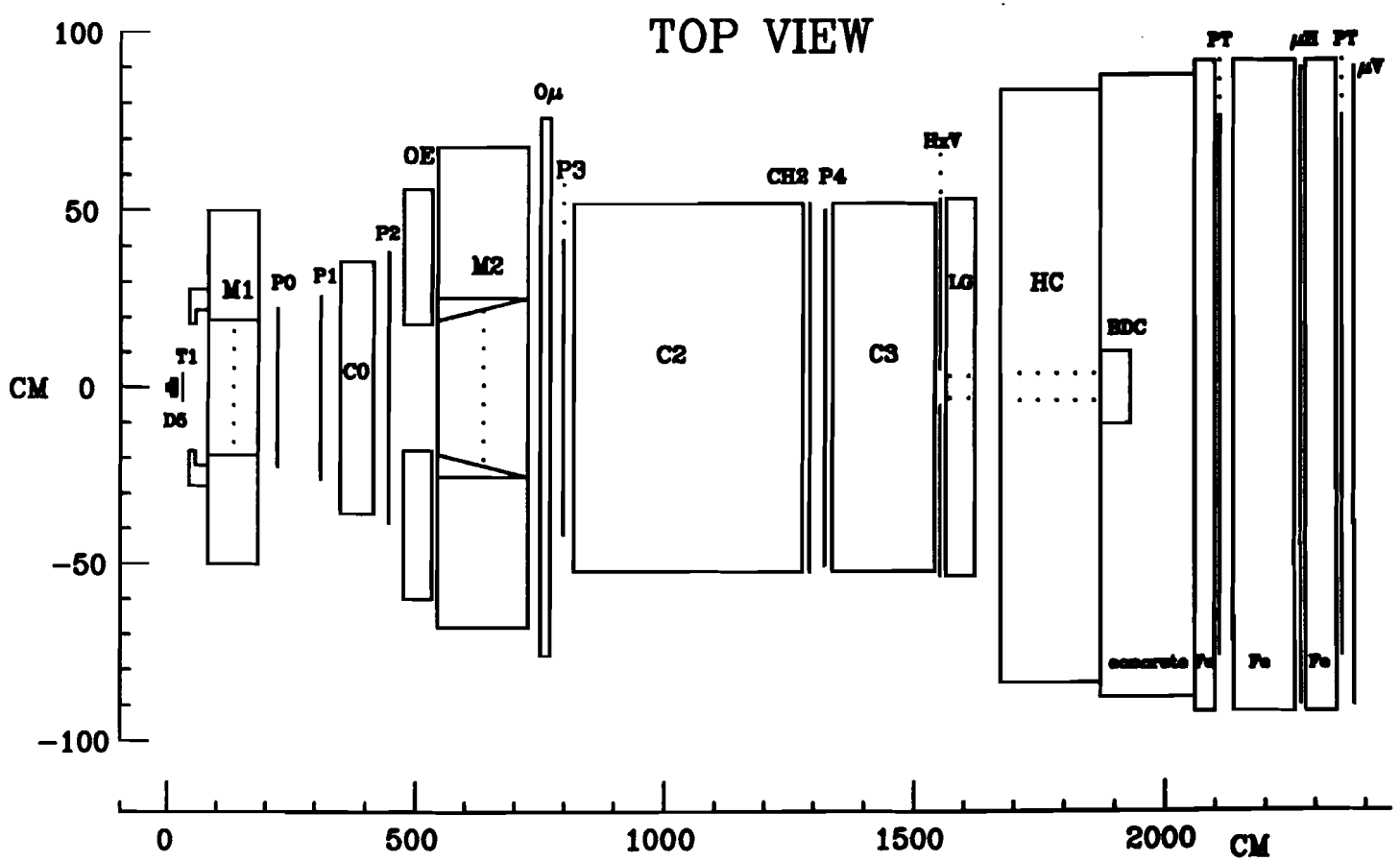

Figure 2.4 The non-bend view.

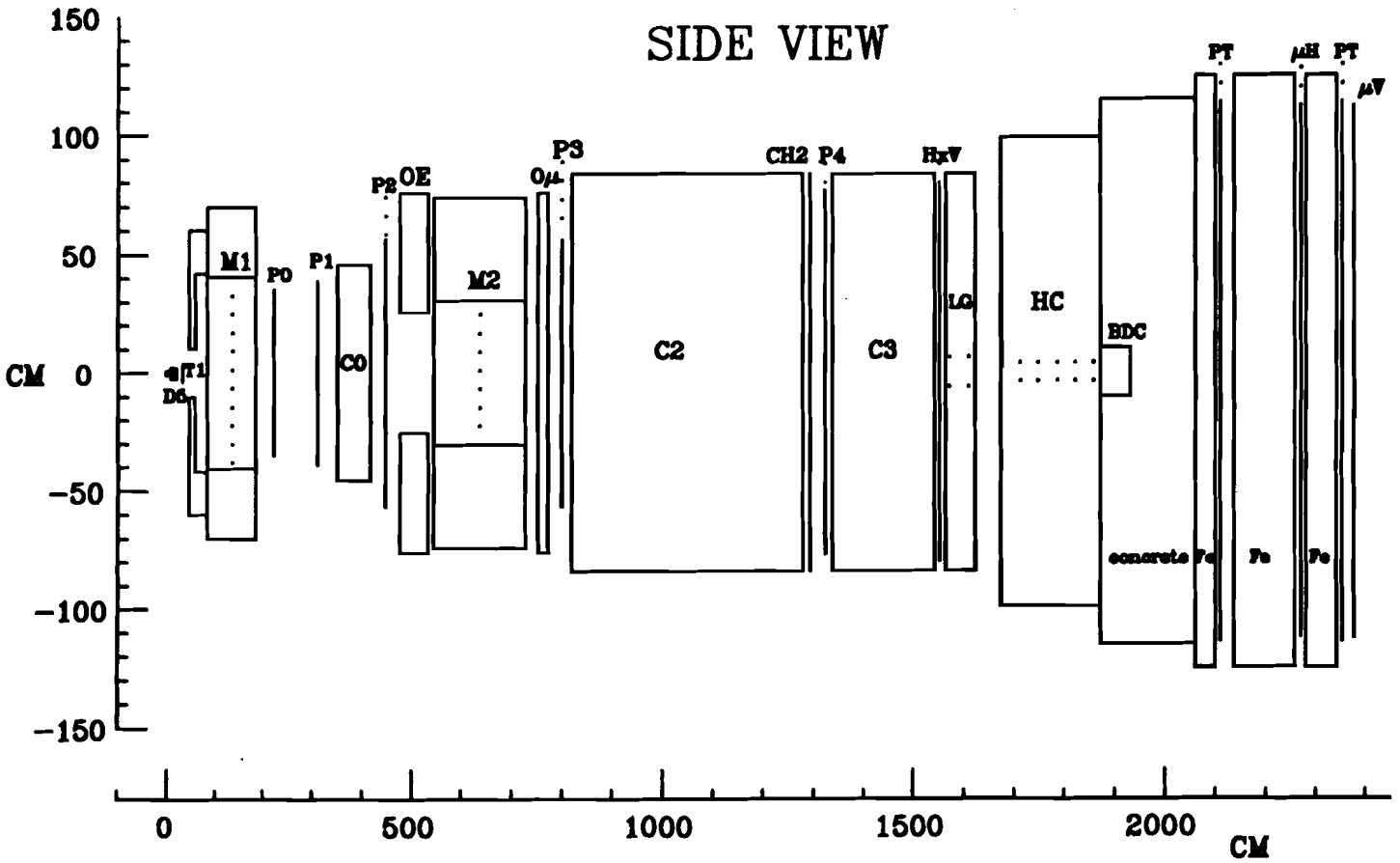

Figure 2.5 The bend view.

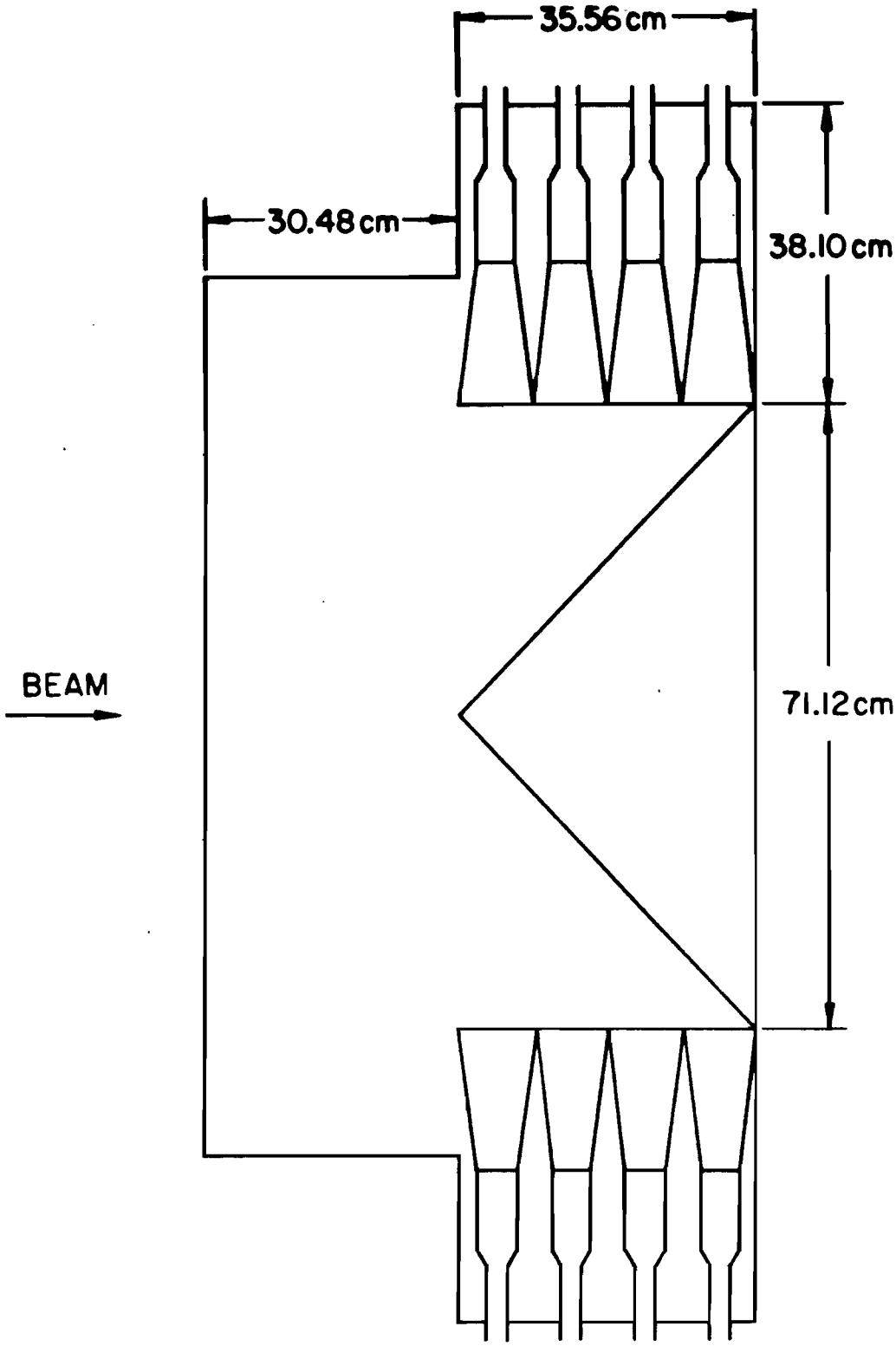

Figure 2.6 C0.

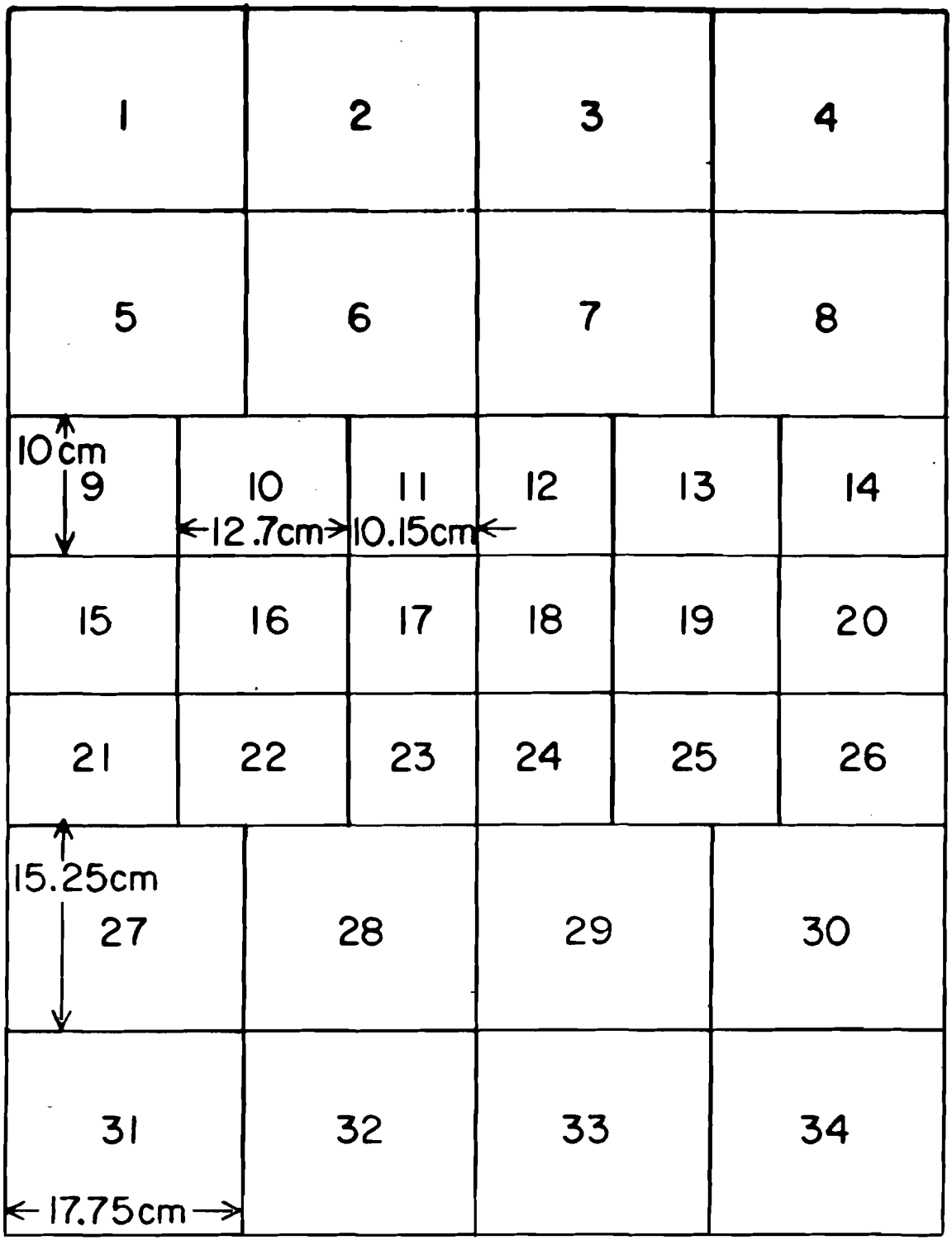

Figure 2.7 The C0 mirror plane.

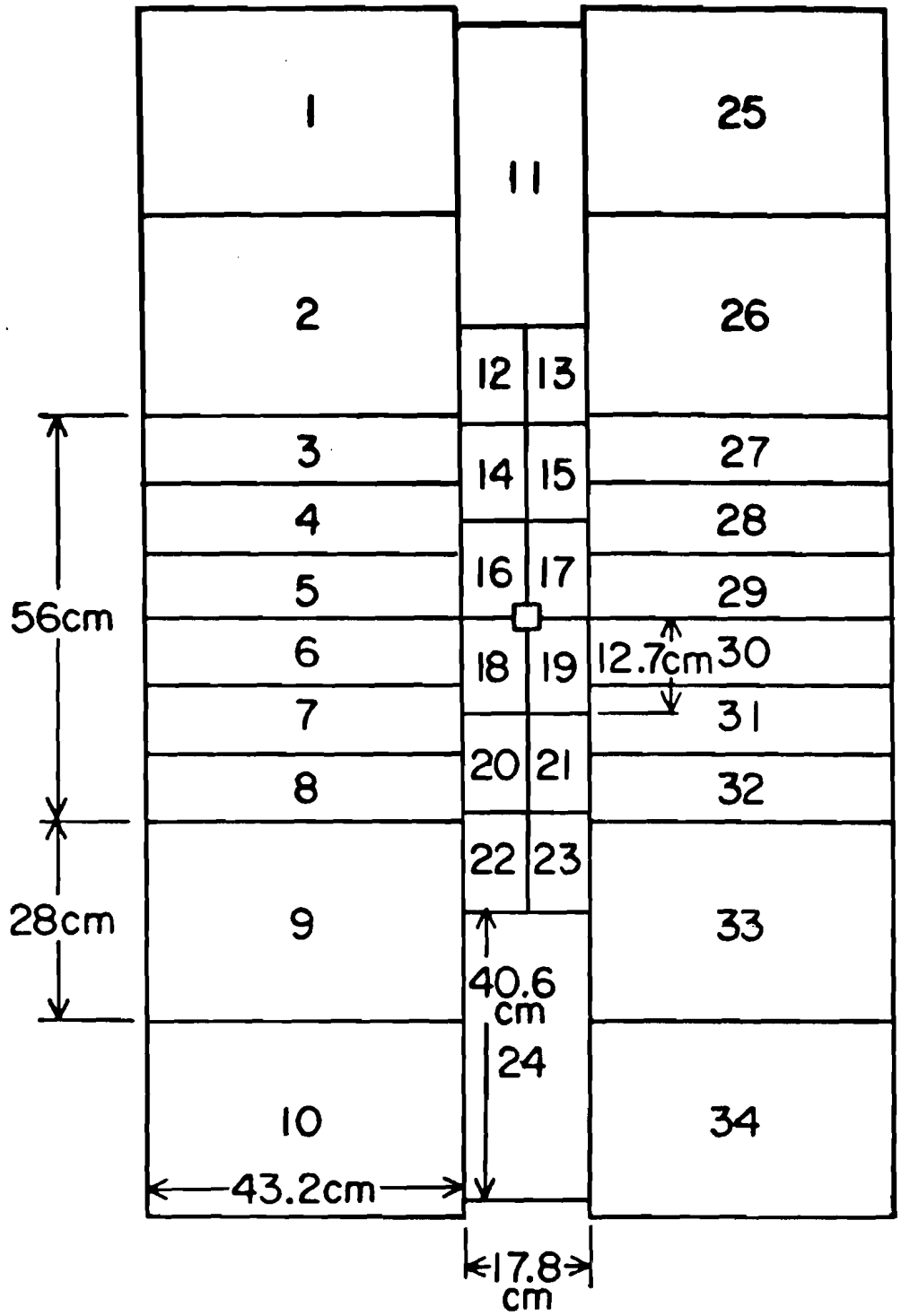

Figure 2.8 The C1, C2, and CH2 cell design.

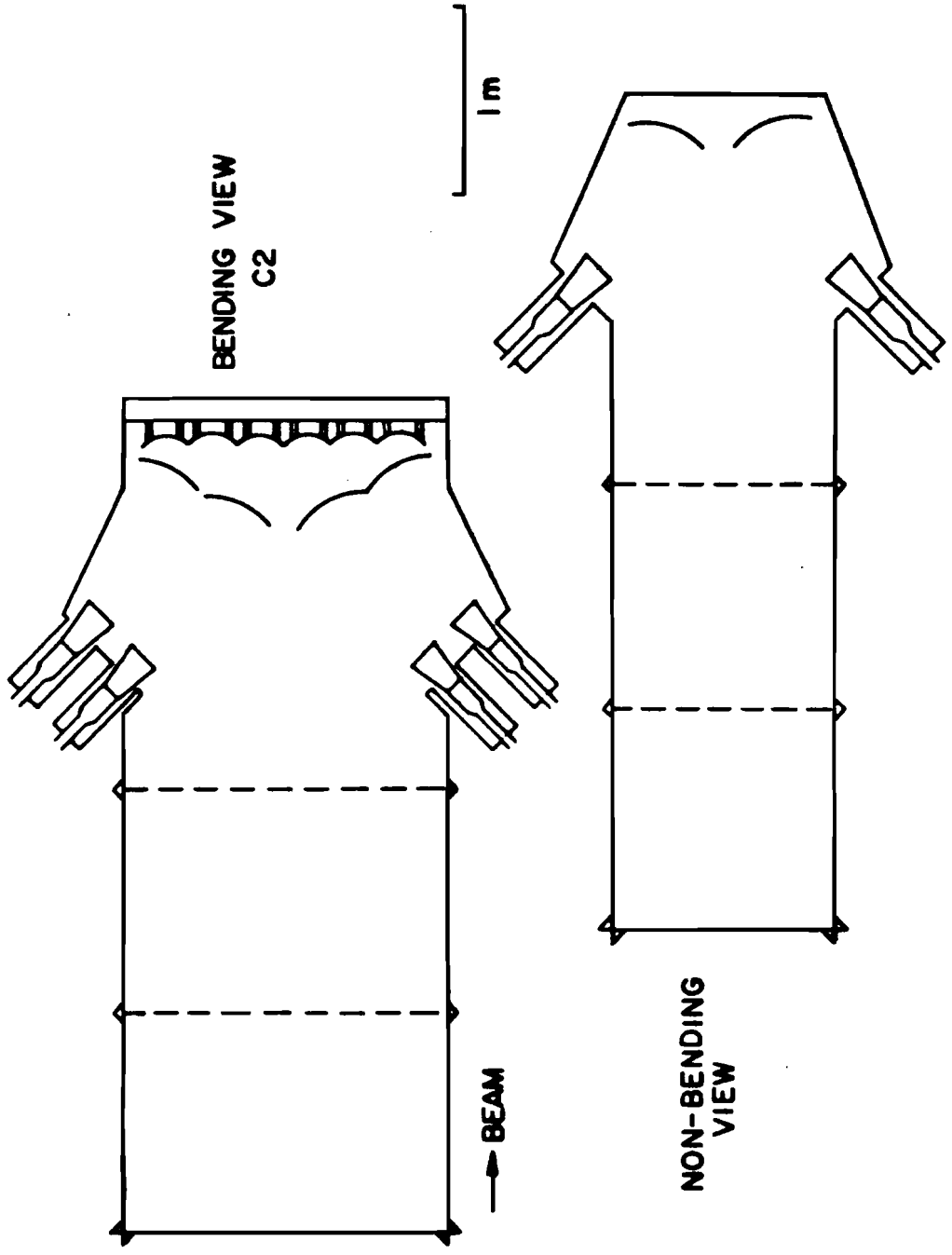

Figure 2.9 The trigger counter (C2).

CHAPTER 3

Data Reduction

3.1 Introduction

E400 accumulated a total of 1200 6250 bpi magnetic tapes worth of raw data during the course of the 800 GeV running used in this thesis. This sample represented roughly 45 million events, and such a large volume is due in part to the relatively unbiased trigger discussed in the previous chapter, and also due to the desire to gather a large statistical sample of the relatively rare charm events (which are expected to have production cross sections roughly three orders of magnitude less than general hadronic processes). It was necessary to process this large sample of raw data into a format which the experimentalist could analyze, and to further reduce this formatted sample to a more manageable size containing events satisfying certain interesting physics criteria to be described.

This data was processed on the FNAL CYBERs for speed. There were three basic data processing phases during which the formatting occurred:

1. Pass 1 – Pattern recognition and track reconstruction.
2. Pass 2 – Vertexing, momentum analysis, particle identification, and calorimetry.
3. Pass 3 – Improvement of the momentum and position resolution by use of the Vertex Chamber and TRM's.

These three phases processed information from tape to tape with a one-to-one correspondence so that at the end of any phase there were still 1200 tapes. To create a more manageable volume, a specialized skimming of tapes was decided upon.

This was known as the physics skim. This final major phase of the data reduction was completed in July 1986 and resulted in a collection of 350 analyzable tapes out of the original 1200 raw tapes. The skimming criteria (section 3.4) were

drawn from Pass 2 information, and these skimmed tapes were then processed through Pass 3. This reduced sample of data could then be skimmed by individual researchers, and small data files could be taken to the various institutions for examination on the slower (but convenient) VAX. I used the ROAR program developed at Illinois by Wiss and Avery to condense the physics skim to a few tapes, or even disk files, containing only certain information about an event which was deemed necessary to reconstruct invariant charm masses and select signal preferentially to background.

3.2 Tracking and Vertexing

The raw data tapes contained as primary information the wire hits of the MWPC's and ADC counts from the numerous photomultipliers associated with individual devices of the E400 detector. This information was then processed by a reconstruction program which converted wire hits into charged particle trajectories by a pattern recognition algorithm, and also removed any ADC count that was below threshold. The reconstruction program was run on samples of the raw data tapes each day of taking data to give warning of "dead" wires in the MWPCs, or malfunctions in the data acquisition or individual photomultiplier assemblies.

Once charged tracks are found, groups of them can be traced backward through the detector to determine a common origin known as the vertex. The primary vertex is presumably the site of the neutron-nucleus interaction. Secondary vertices are possible, such as the site at which a charmed particle decays into several particles or the site at which one of the strange V^0 particles decays into a pair. Although vertexing (and the momentum analysis vital to vertexing) was performed in Pass 2 while track reconstruction was performed in Pass 1, the two problems are related conceptually (both are topological) and analytically (through momentum analysis, each aids determination of the other).

The reconstruction program takes information on the 15 wire plane Z locations, wire spacings, and central wire numbers from the raw data tapes, and iterates a fitting routine to find track parameters by minimizing the χ^2 per degree of freedom. The resulting tracks were divided into two basic categories:

1. Full tracks – these trajectories, known as "inner", remain within the fiducial volume of the detector downstream of M2 and intercept at least P3 and probably P4.
2. Stubs – these trajectories, known as "outer", do not pass downstream of M2 but do intercept P0, P1, and P2.

Because there are inefficiencies and spurious hits, the program must be flexible about adding or subtracting hits and comparing the result.

The pattern recognition program first searches for full tracks by forming a straight line through the X projection of the wire hits. The next step is to use bend-view information from the U and V planes to form line projections, which can be matched with the X projection. These resulting line segments in the bend view were formed by fitting a line segment from P0 to P2 joined to a line segment from P3 to P4 at the bend center of M2. In general, the two line segments for a given candidate track will be essentially collinear in the X view but form a kink in the bend plane. There are five main outputs of the Pass 2 program which describe a track and are used in reconstructing specific charmed state invariant masses:

1. X_0 – the x-coordinate of the track at the bend point of M2.
2. Y_0 – the y-coordinate of the track at the bend point of M2.
3. X' – the x-slope of the track on the upstream side of M2.
4. Y' – the y-slope of the track on the upstream side of M2.
5. δ' – the bend angle between the upstream and downstream segments.

The magnitude of the track momentum is estimated by dividing the magnet's effective "kick" by the bend angle.

Full tracks were refit in Pass 2 with a better wire chamber geometry and magnetic field mappings for M1 and M2, and momenta were then recomputed. This took into account the nuances of fringe field effects at P0 and P3, magnet rotation angles, weak focusing effects, bend center corrections, and helical path corrections. These are discussed in detail in Tom Kroc's thesis.

Stubs were not accepted downstream of the M2, and were conventionally assigned a zero M2 bend angle. No momentum could have been assigned to stubs by the crude kink approximation during Pass 1 processing, but stub momentum was determined during Pass 2 by pinning stub origins to the primary vertex and determining their bend angle through M1.

The original BOBCAT program was used in a diagnostics package to find the X, Y, and Z location of the primary vertex. This was designed to quickly find a crude vertex by tracing full tracks back to the target region, and minimizing the χ^2 of the X and Y centers of groups of trajectories formed by requiring each trajectory to be within .15 inch of a neighboring trajectory. This was used to check if the beam was grossly mistargeted. For data reduction, a resurrected version of a vertex program written by J.J. Russel for E87 was adopted and christened the BOBKAT (only the homonym remains). The vertex was found by tracing full tracks back to the target region using both bend and non-bend information. As with BOBCAT, there were sometimes tracks which were resolvable from the plurality cluster. In these cases, their X, Y, and Z locations were also determined from a χ^2 minimization and these were made available by a sequentially numbered flag word signaling the dominance (number of tracks) of the cluster. However, to be considered as part of a possible primary vertex a track must fall within the transverse dimensions of the target segment at its midplane Z

location. The error on the vertex location is too large to allow the individual target segments to be resolved by Pass 2 information.

The vertex resolution and track momenta were improved upon in the Pass 3 processing by using information from the vertex chamber and the TRM's. Main spectrometer wire hits were redetermined from the drift times indicated by the TRM's wire groupings of P1, P2, P3, and P4. These main spectrometer tracks were then linked with tracks found from fitting the wire hits of the 18 planes of the vertex chamber (D5). 85% of those main spectrometer tracks which could be assigned to a primary vertex were successfully linked with D5. The momentum resolution of the full tracks was much better than was the case for the stubs because of the longer lever arm of the tracks. The resolution was

$$\frac{\sigma_p}{p} = K \times 10^{-4} \cdot p \tag{1}$$

where for tracks K=2 and for stubs K=14. Thus, the resolution values for a 100 GeV track is 2% or stub is 14%.

The location of a vertex found from the full Pass 3 processing had a transverse rms resolution of about 60μm and longitudinal resolution of about 1500μm for a typical 50 GeV/c track. This was about an order of magnitude more refined than the result of the Pass 2 vertex determination. This allows the individual target segments to be resolved.

There are also trajectories originating downstream of P0 – V^0 tracks, which might be associated with long-lived neutral particle decays and are not directly associated with the primary event vertex. These are indicated as leftovers once the pattern recognition has settled on a set of full tracks and stubs. The remaining unused hits must reconstruct as a pair of tracks originating from a vertex. One of the trajectories is required to possess momentum information (i.e., be accepted upstream of M2).

In addition to these V^0's identified by the reconstruction program there are also such topologies which originate upstream of P0, and can be associated with either K^0 or Λ decays. The tracks from these decays separate in M1, and during Pass 2 processing these trajectories are removed from the group used to determinate the primary vertex. As with reconstruction V^0's one track in the pair must be a full track so that momentum information from M2 can be derived.

3.3 Particle Identification and Čerenkov Analysis

Particle identification was accomplished by E400 at the level of the Pass 2 program, primarily by use of a Čerenkov analysis package. There were several types of particle identification which E400 employed, or in principle could have employed. The method which was relevant to this thesis employed Čerenkov analysis of charged particles. In particular, for the purposes of this thesis I required the Čerenkov analysis to distinguish between charged kaons and charged pions. Identification of other categories of particle type (mass) were largely unimportant to the particular states I observed.

I now give a brief overview of the other types of particle identification which could in principle be analyzed. The type of neutral particle identification which E400 undertook was the V^0 analysis previously described. This was not directly relevant to the states I observed, but was used by some other researchers. There was no package written to attempt to resolve neutral pions by using the lead glass, but that does not affect this thesis. There was an analysis package in Pass 2 which identified muons using the proportional counters and two banks of muon scintillation hodoscopes (all placed downstream of a large beam dump), but muons are also not relevant to this thesis. Although outer electrons could in principle have been distinguished by an analysis of the 16 radiation length electron photometer placed on the upstream side of

M2, there was also electron identification provided by the Čerenkov analysis. Electron identification is also not directly relevant to this thesis, although I did reject particles definitely identified as electrons by the Čerenkov routines from the sample of pions which I used.

The inputs to the Čerenkov analysis were the particles' momenta, Čerenkov mirror plane intersections of the charged particles, and ADC counts. The three counters employed were threshold counters. They were used to register whether or not a given charged particle was fast enough to have generated a Čerenkov light cone which could then be detected by a photomultiplier tube, whose output current was sent to ADC's for digital recording. The Čerenkov effect[27] occurs when a charged particle traverses a dielectric at a speed in excess of the speed of light in that medium. The angle of emission θ_C for Čerenkov light is given by:

$$\theta_C = \arccos \frac{1}{\beta n} \tag{2}$$

where n is the index of refraction. E400 exploits this threshold effect by measuring the momentum of a charged particle with the spectrometer, and then testing if light has been generated by the value of phototube ADC results ("off" versus "on") and comparing this result with the threshold momentum expected for particles of a particular mass ($p = \gamma m \beta c$ implies a higher threshold momentum for a higher mass).

The starting point of the Čerenkov analysis was an algorithm (explained in Appendix A) which decided how Čerenkov light was expected to be distributed when a track falls near the boundary of several Čerenkov cells, and requires the X-Y determination of the track-mirror plane intersection. At this point some hypothesis must be assumed concerning the identity of the particle in order to determine θ_C, and consequently the maximum radius the Čerenkov cone projects onto the mirror plane at

the point of intersection. The next step was to process the ADC information describing which cells are "on" and compare this with the set of cells which are cells were expected to be "on".

E400 developed two independent algorithms to handle the task of comparison. CERAL, developed by FNAL, was one of the two algorithms. It used the raw pulse height information to yield an observed number of photoelectrons for each cell. In general, one photoelectron registered 120 counts above pedestal. The expected number of photoelectrons for CERAL for a given cell caused by a given track was calculated separately for four particle identification assumptions – electron, pion, kaon, or proton. Tracks were analyzed as clusters which pointed together at a group of adjacent cells, and the individual tracks within a cluster were looped over for all four identity hypotheses. A given hypothesis was rejected if the observed light information from a cell did not match the expected light value. CERAL was the slower of the two algorithms

The final judgement of the track identity was stored in the variable ISTATP, which was a 4-bit word with the following basis:

No bits "on": Indeterminate.
Bit 1 is "on": Consistent with being an electron.
Bit 2 is "on": Consistent with being a pion.
Bit 3 is "on": Consistent with being a kaon.
Bit 4 is "on": Consistent with being a proton.

It is seen that a particle could be tagged with a unique identity, consistent with several particle types, or totally confused, or in rare cases be inconsistent (when the separate Čerenkov counters flagged opposing particle identification combinations). When ISTATP is 15 all four bits are on and the particle identity is totally confused.

The other algorithm used for light comparison, known as LOGIC, is the older of

the two and was developed at the University of Illinois. It is currently being used by E687 (a heavy flavor photoproduction experiment at FNAL). LOGIC assumed that all tracks are pions for the purpose of estimating the amount of light falling in cells. LOGIC did not use a pulse height method but rather a less elaborate and therefore faster digital on-off technique. The observed current from a cell was said to indicate that the cell was "on" if the ADC value was at least 10 counts above pedestal. For a very few noisy cells, 20 counts above pedestal was required. The final judgement LOGIC made of the particle identification was stored in the variable ISTATL. The interpretation of ISTATL was the same as ISTATP.

ISTATL was arrived at by the logical "and" of three index words (one four-bit particle identification for each Čerenkov counter), hence the name LOGIC. The counters have different thresholds, so it is worthwhile to combine their information. An index word was essentially a two-dimensional array in which the indices were the momentum region the particle fell into (as determined by the pion, kaon, and proton thresholds for the counter), and a status word indicating whether or not the track could be considered above threshold for a given counter. These status words determined if a given track in a given counter (C0, C1, or C2) was observed to be "off", "on", "confused", or "out of the fiducial volume" of the counter. The category of "on" indicated that the track under consideration was identified as generating sufficient light to turn "on" cells in that counter. A variable known as PEOF was the number of unconfused photoelectrons that would have been generated by a track under the pion hypothesis for tracks which were actually classified as "off". A minimum requirement of 2.5 photoelectrons was used in particle identification in E400. The third category simply states that there is too much interference from possible light contribution of nearby tracks to decide that the given track was indeed responsible for light which was observed. The fourth category was relevant to C1 and C2 principally, for which

stubs were not accepted.

In principle LOGIC can use the ISTATL information from a first pass to improve the starting point of a second pass through the light comparison routines if there is ambiguity as to the identity of the particle. However, in practice iterations were found to improve the identification only on the order of once per thousand events. The iteration capability was therefore flagged off to save cpu time.

I now will explain the algorithm by which LOGIC determined if a track was responsible or not for turning "on" a given cell. For a given track, the starting point was determination of the which cell the track hit, what its neighbors were, and the distances from the intersection to the affected cell boundaries. The code then looped over all the cells struck, starting with the principal cell in which the track fell. The "out of the fiducial volume" category is decided at this stage simply by whether or not there is any cell in the counter which accepts the track. Care was taken not to allow a track to be lost to this category by falling between the cracks. Also, a border distance (determined by the projection of the Čerenkov cone of light half angle on the mirror plane) was added to the outermost cells as part of the fiducial volume.

The photoelectron yield expected for the principal cell and adjacent cells was calculated under the pion hypothesis. The array SMPE kept the sum of expected photoelectrons on a cell by cell basis, summed over all possible tracks. The number of photoelectrons for a cell due to a particular track under consideration was stored in TKPE. If the expected light in a cell was less than .05 photoelectrons, information from that cell was considered unimportant (noise). A check was made over all concerned cells to see if they were physically observed to be "on". If not "on", then PEOF was incremented by the light expected to fall in that cell. When all cells were checked, if the track was not flagged as in the "on" category then the value of PEOF was consulted.

If it is above 2.5, the track is said to be in the "off" category otherwise it was called "confused." The value of 2.5 was determined by a study of the signal-to-background and number of events of ϕ signals.

I now discuss the effects of confusion from other tracks. When a cell was physically "on" a difference DIFF was formed between SMPE and TKPE. This indicated how much of the light falling on the cell was actually expected from tracks other than the track under consideration. If DIFF exceeded .2 photoelectrons (SDIFF), the cell was ignored by saying it was too "confused," which meant that at least two-tenths photoelectrons were expected from other tracks. The track fell into the "on" category only if the cell was physically "on" and less than .2 photoelectrons was expected from all other tracks.

Figures 3.1, 3.2, and 3.3 are threshold curves for protons from lambda decays in the data for C0, C1, and C2, respectively. They show the fraction of protons which are identified as belonging to the "on" category as a function of momentum provided that the track is identified as either "on" or "off" – i.e., "don't knows" are excluded. The curves turn-on quickly and are effectively fully on above threshold. The accidental turn-on rates below threshold are low for the two downstream counters C1 and C2, but high for the upstream counter C0 which is heavily struck by electron stubs. Table 3.1 contains the pion, kaon, and proton threshold information derived from the fits to the proton threshold for C0, C1, and C2 during the 800 GeV running. Figures 3.4, 3.5, and 3.6 show the respective threshold curves generated by the Monte Carlo simulation program. Note that the Monte Carlo is doing a good job of reproducing the thresholds given, the accidental turn-ons observed in data, and the high efficiency above threshold.

To test the ability of the Čerenkov algorithms to correctly identify charged par-

ticles, clean samples of V^0's were used. The K_s^0 decays into a pair of pions and so the pion-kaon determination can be checked. The Λ decays into a pair of oppositely charged protons and pions. The invariant mass plots of the V^0's are shown in Figures 3.7(a) and 3.7(b) – they have been strongly cleaned. Experimental checks of Čerenkov algorithms, including for example Figures 3.1 to 3.3, come from clean V^0 samples.

Because of kinematics, the proton is the faster of the two particles in the Λ decay. To isolate the proton from the π in Λ decays, the proton was required to have 5 GeV/c more momentum than the π . The protons were required to have momenta in the range where unambiguous proton Čerenkov identification is possible (i.e., between 10 and 80 GeV).

A comparison is made of the particle identifications resulting from the two V^0 samples for both LOGIC and CERAL in Table 3.2. The efficiency of the Čerenkov routines is fairly good. A proton is incorrectly called a non-proton in about 14 to 18 % of the cases, and a pion is misinterpreted as a definite kaon only .2 to .6 % of the time and called a non-pion of any sort 6 to 8 % of the time.

LOGIC has more success than CERAL at flagging definite protons, but CERAL is better at flagging definite pions. The two routines are similar in kaon misidentifications, but there are no states which can be kinematically cleaned to a sufficient extent to allow a direct determination of the kaon efficiency. The two algorithms should in general be used in a complementary fashion by the logical "or" of their judgement words, ISTATP and ISTATL.

It is important for the charm analysis sections to know that about 80% of the tracks are identified as consistent with being a pion.

3.4 Physics Reduction

The physics reduction was done from Pass 2 tapes to save time. Pass 3 then improved the momentum needed to reconstruct the charm invariant masses, and the vertex resolution was sufficiently improved to allow some researchers to use life-time techniques to isolate the secondary charm vertices.

The following criteria were decided upon by committee:

1. A clean K_s. (Demand that the invariant mass $M_{\pi\pi}$ falls within 30 MeV of 497.67 MeV/c^2 for conventional V^0's or within 40 MeV/c^2 for reconstruction V^0's.)
2. A clean Λ. (Demand the mass $M_{p\pi}$ falls within 20 MeV/c^2 of 1115.6 MeV/c^2 for conventional V^0's or within 25 MeV/c^2 for reconstruction cases, and demand that the faster track be identified as a Čerenkov definite proton or an ambiguous kaon-proton when one of the decay trajectories points back to the primary vertex.)
3. Phi Skim. (Demand two oppositely charged particles be Čerenkov identified as either definite kaons or kaon-proton ambiguous and that their invariant mass fall within 20 MeV/c^2 of 1020 MeV/c^2.)
4. D* candidate skim. (Demand the mass $M_{K\pi}$ is within 150 MeV of 1864.7 MeV/c^2 and $M_{K\pi\pi} - M_{K\pi} < 165$ MeV/c^2. The kaon and the first pion must be oppositely charged; the the kaon must be Čerenkov identified as a definite kaon or kaon-proton ambiguous. The pion candidates are unqualified and can be any Čerenkov identification, including kaon or kaon-proton ambiguous. Unless otherwise stated, this can be assumed throughout.)
5. D* candidate skim. (Demand a clean K_s and require the $M_{K_s\pi\pi}$ mass to be within 150 MeV/c^2 of 1864.7 Mev/c^2 with the pions having opposite charges. Also demand $M_{K_s\pi\pi\pi} - M_{K_s\pi\pi} < 165$ MeV/c^2.)
6. D^+ candidate skim. (Demand a Čerenkov identified definite kaon and that $M_{K\pi\pi}$ is within 150 MeV/c^2 of 1869.4 MeV/c^2. Also require that the pions have the same sign, and the event multiplicity is less than 12.)
7. Λ_c candidate. (Demand that a definite proton, a definite kaon or kaon-proton ambiguous track, and an oppositely charged pion give an invariant mass $M_{pK\pi}$ within 150 MeV/c^2 of 2282 MeV/c^2. Also require the event multiplicity is less than 12.)
8. Λ_c candidate. (Demand that a clean K_s and a track flagged as a definite proton or kaon-proton ambiguous give an invariant mass $M_{K_s\pi}$ that falls within 150 MeV/c^2 of 2282 MeV/c^2.)
9. A "good" muon. (Demand that a single track fires 3 of the 4 muon planes and that the track has $p_\perp > 1.0$ GeV/c.)

10. A "kink". (A $\Sigma^{\pm}$ candidate).
11. Oppositely charged pair of definite kaons.
12. Kaon - proton pair. (Both tracks are identified as definites and must have the same charge.)

Certain specific charm states were searched which the group decided would be of interest and most likely to be found. Other skims were included because some thought they would be natural participants in certain other charm processes. Both particle and antiparticle combinations were selected for the charmed candidates. The kinematic mass selection cuts were chosen to be as broad as possible, but limited by the constraint of keeping the tape volume low.

Table 3.1 Čerenkov Thresholds.

	C0	C1	C2
Pion	2.71	5.74	10.78
Kaon	9.59	20.31	38.11
Proton	18.22	38.61	72.44

1. Momentum in GeV/c
2. 800 GeV run.

Table 3.2 Checks on Čerenkov algorithms.

COMPARISONS ON PROTONS FROM LAMBDAS		
Track's Status Word	LOGIC	CERAL
Inconsistent	10.4%	11.3%
Definite Kaon	6.3%	5.0%
Non - Proton	18.1%	13.6%
Definite Proton	33.7%	20.0%
P/K Ambiguous	21.4%	32.5%
Confusion	15.6%	19.8%

COMPARISONS ON PIONS FROM KSHORTS		
Track's Status Word	LOGIC	CERAL
Inconsistent	2.5%	8.2%
Definite Kaon	0.2%	0.6%
Definite Proton	0.8%	0.5%
P/K Ambiguous	3.3%	2.3%
Non - Pion	7.5%	5.6%
Definite Pion	12.5%	21.1%
Confusion	19.6%	19.9%

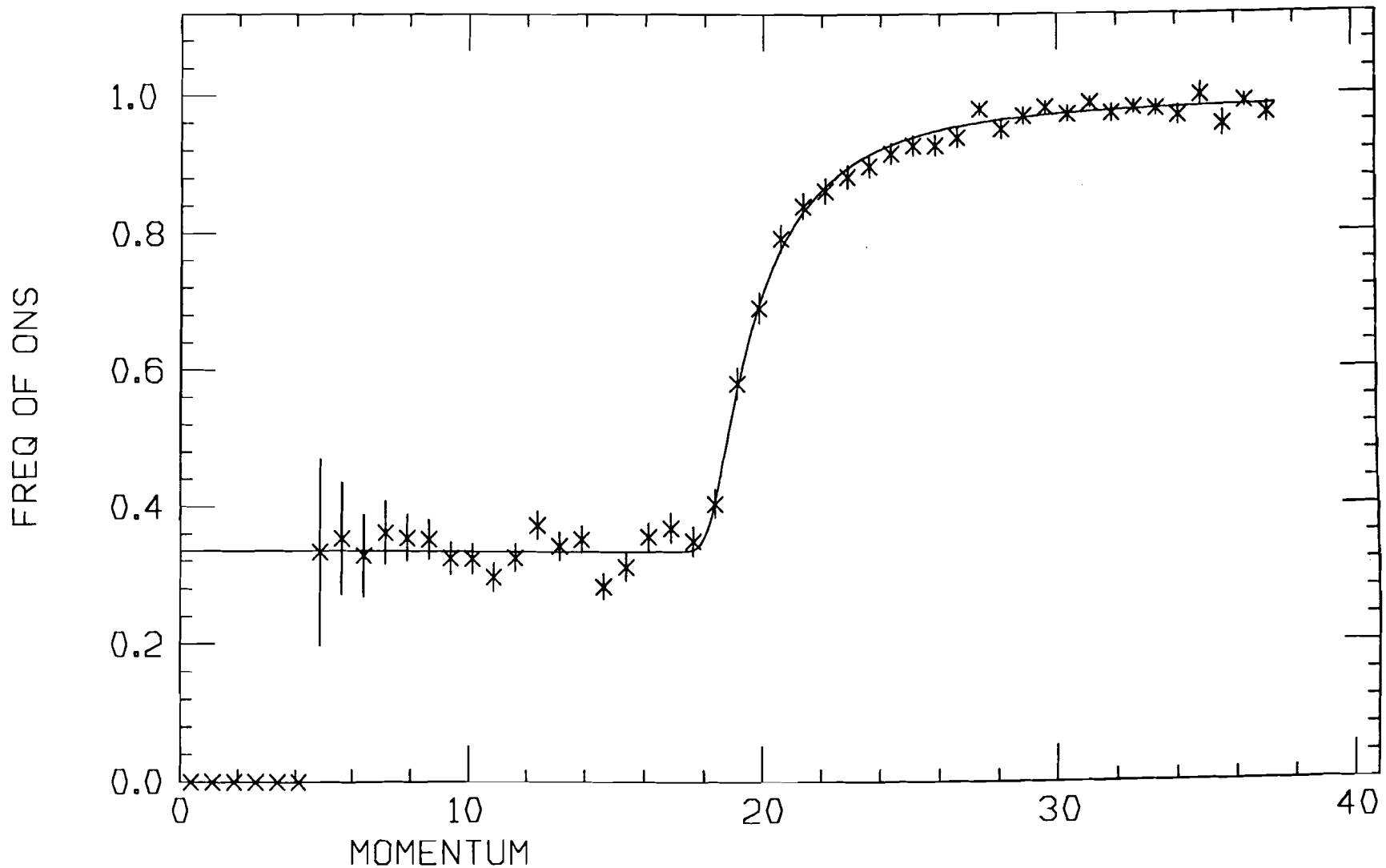

Figure 3.1 C0 threshold curve for data.

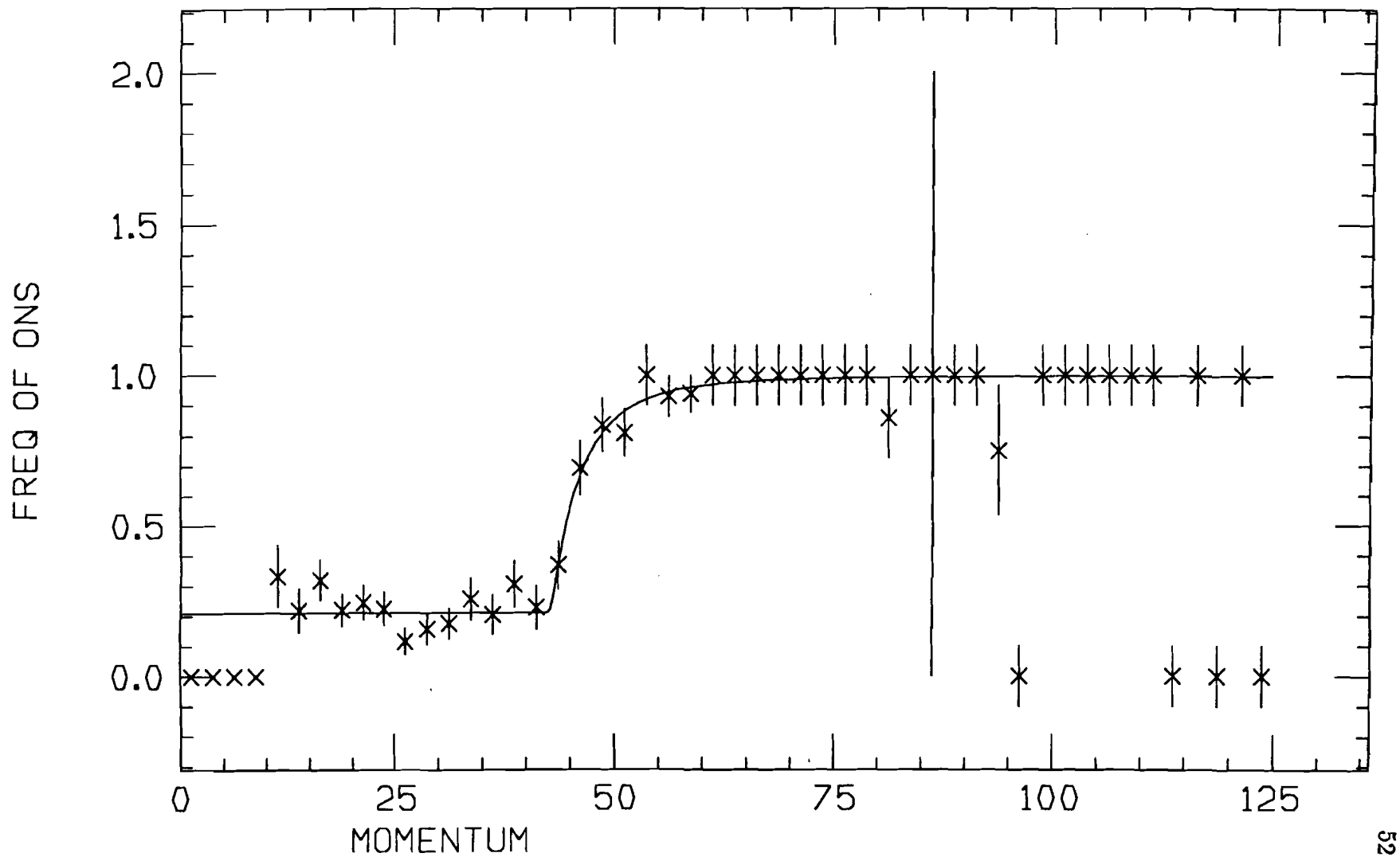

Figure 3.2 C1 threshold curve for data.

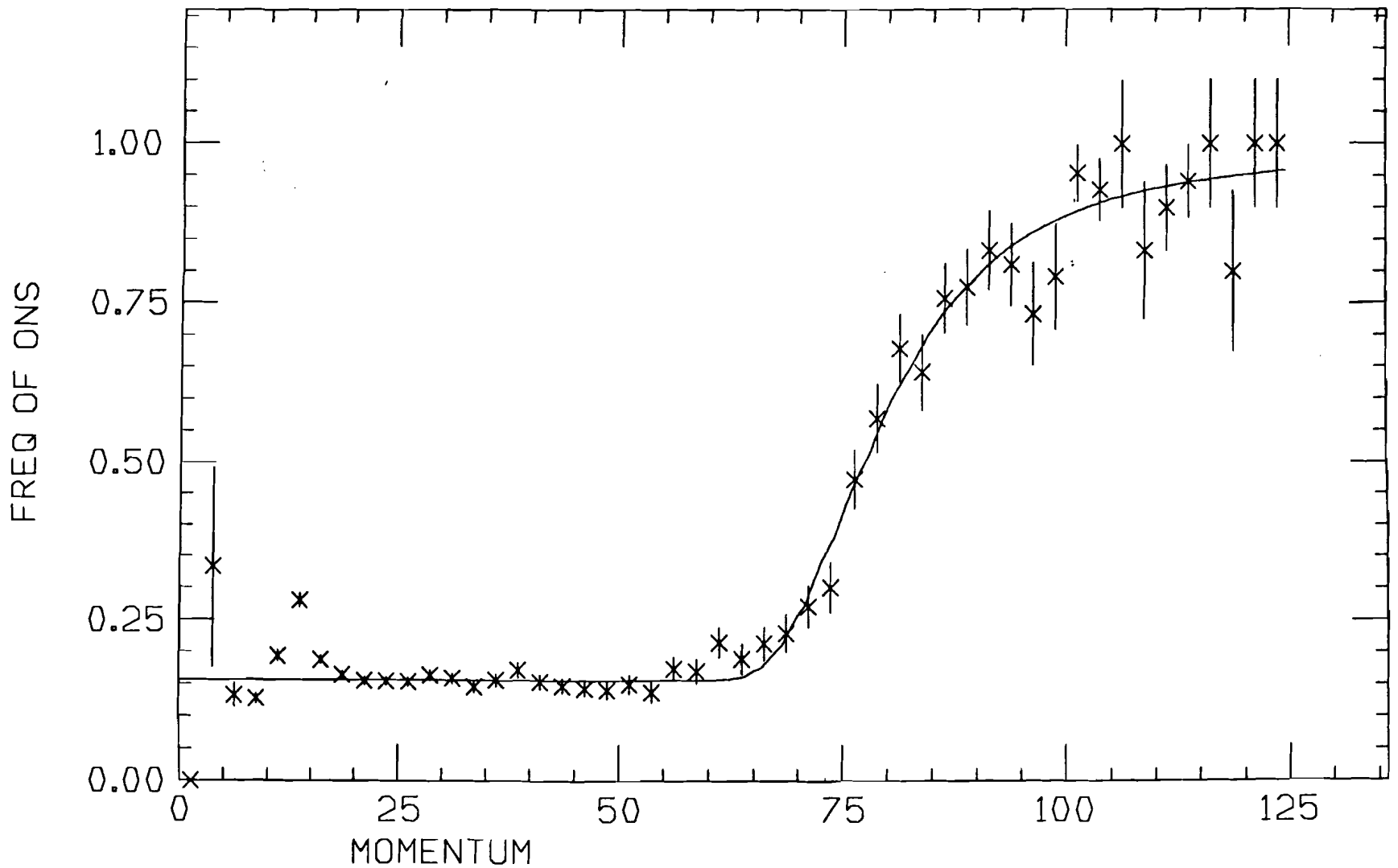

Figure 3.3 C2 threshold curve for data.

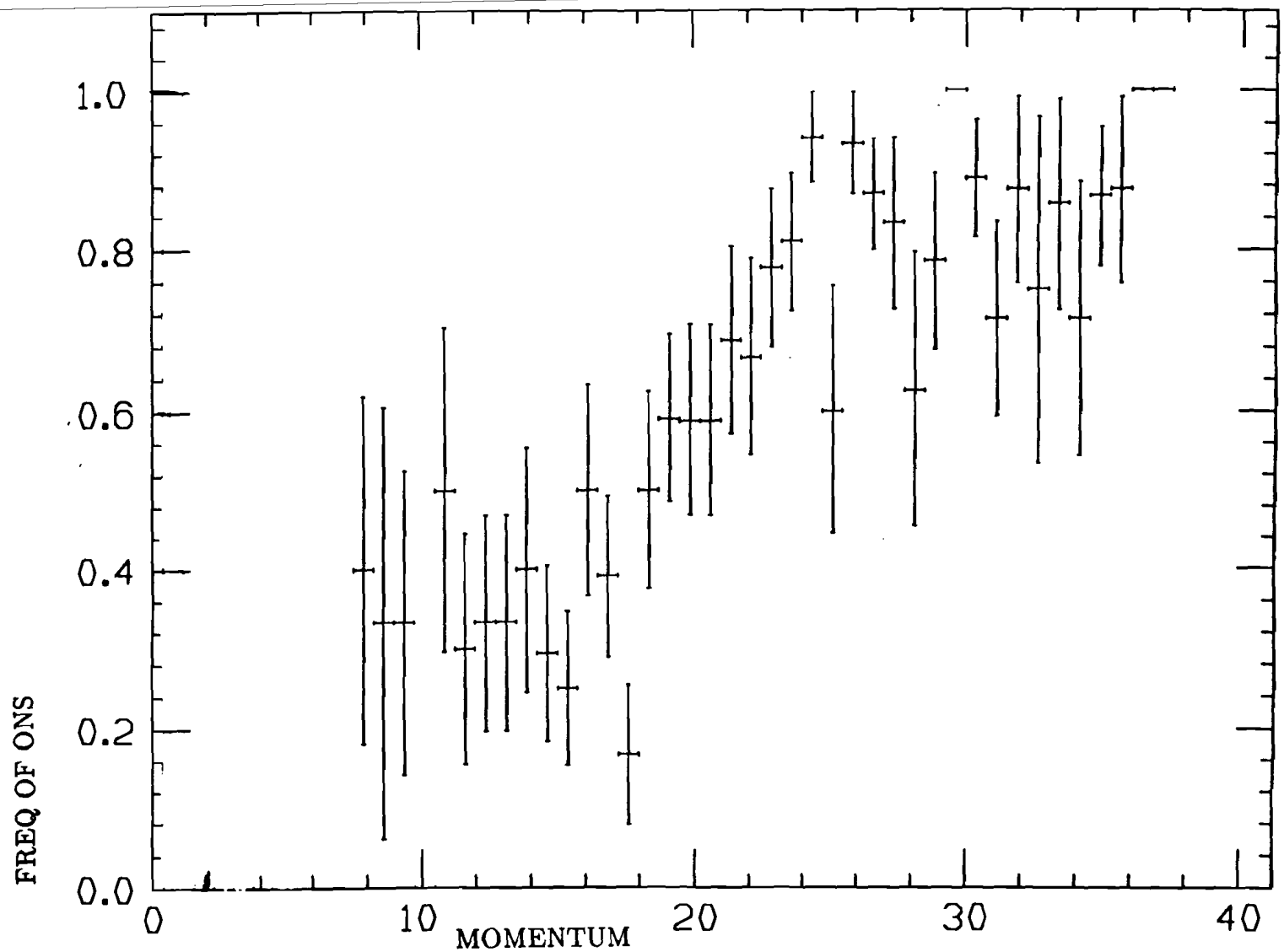

Figure 3.4 C0 threshold curve for MC.

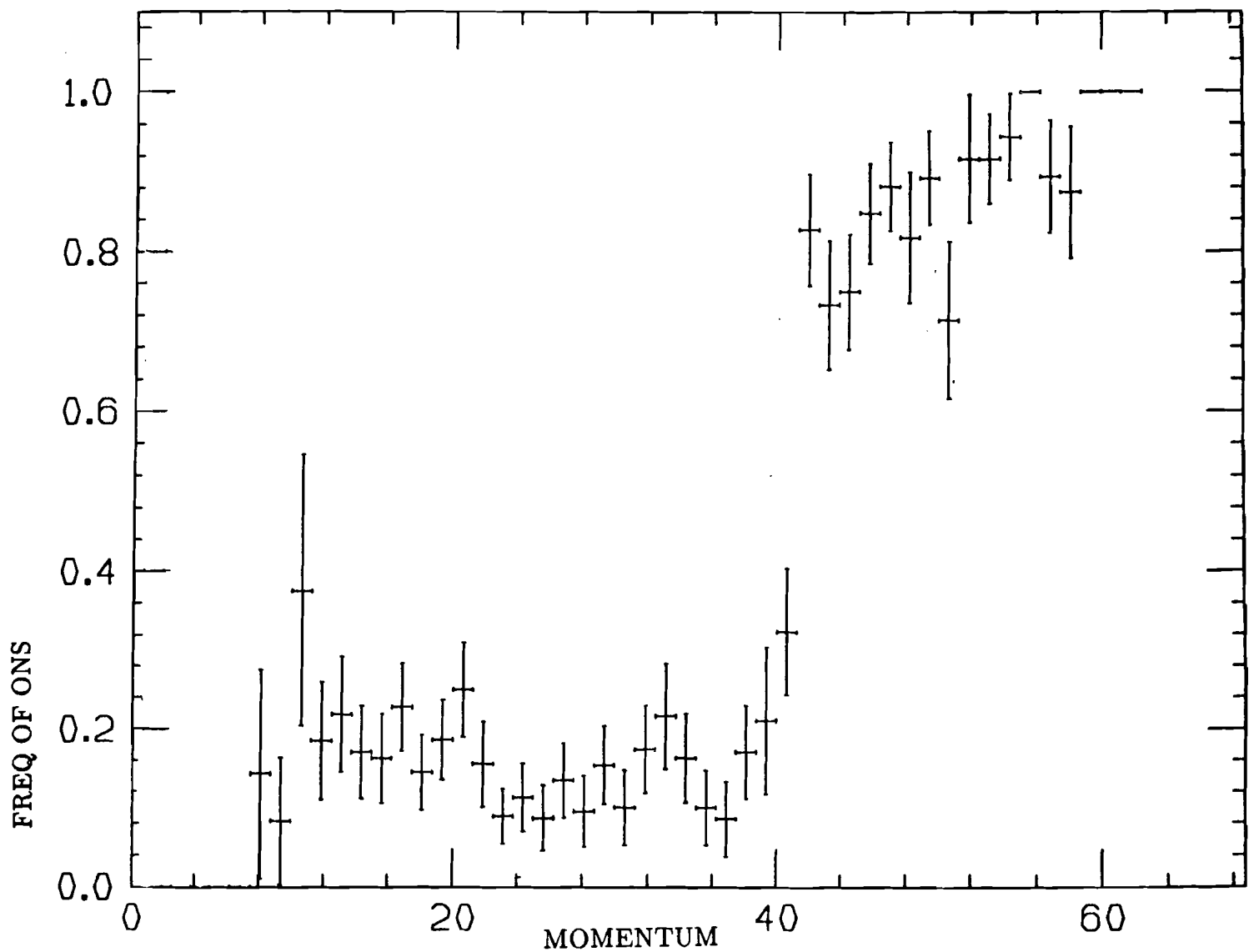

Figure 3.5 C1 threshold curve for MC.

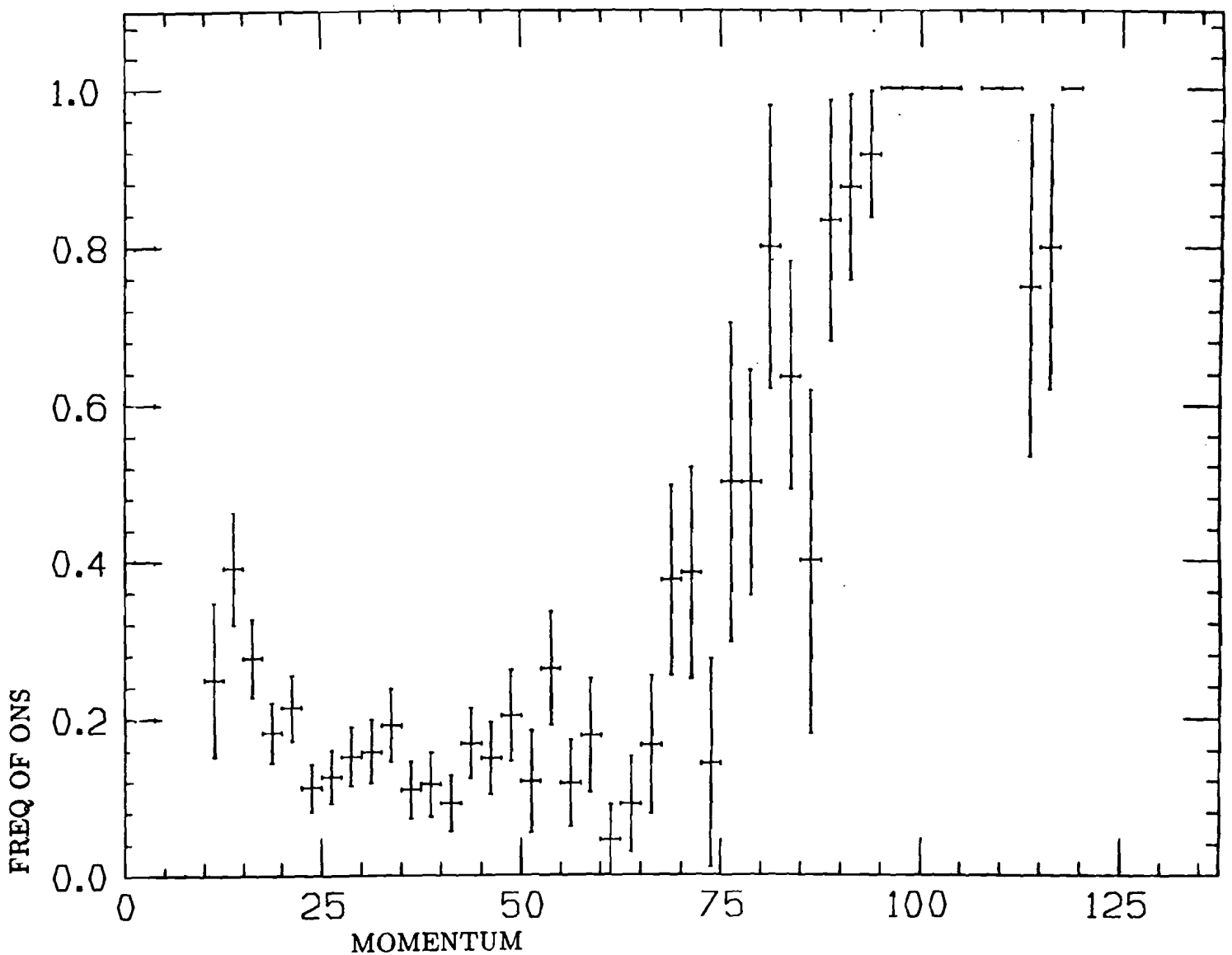

Figure 3.6 C2 threshold curve for MC.

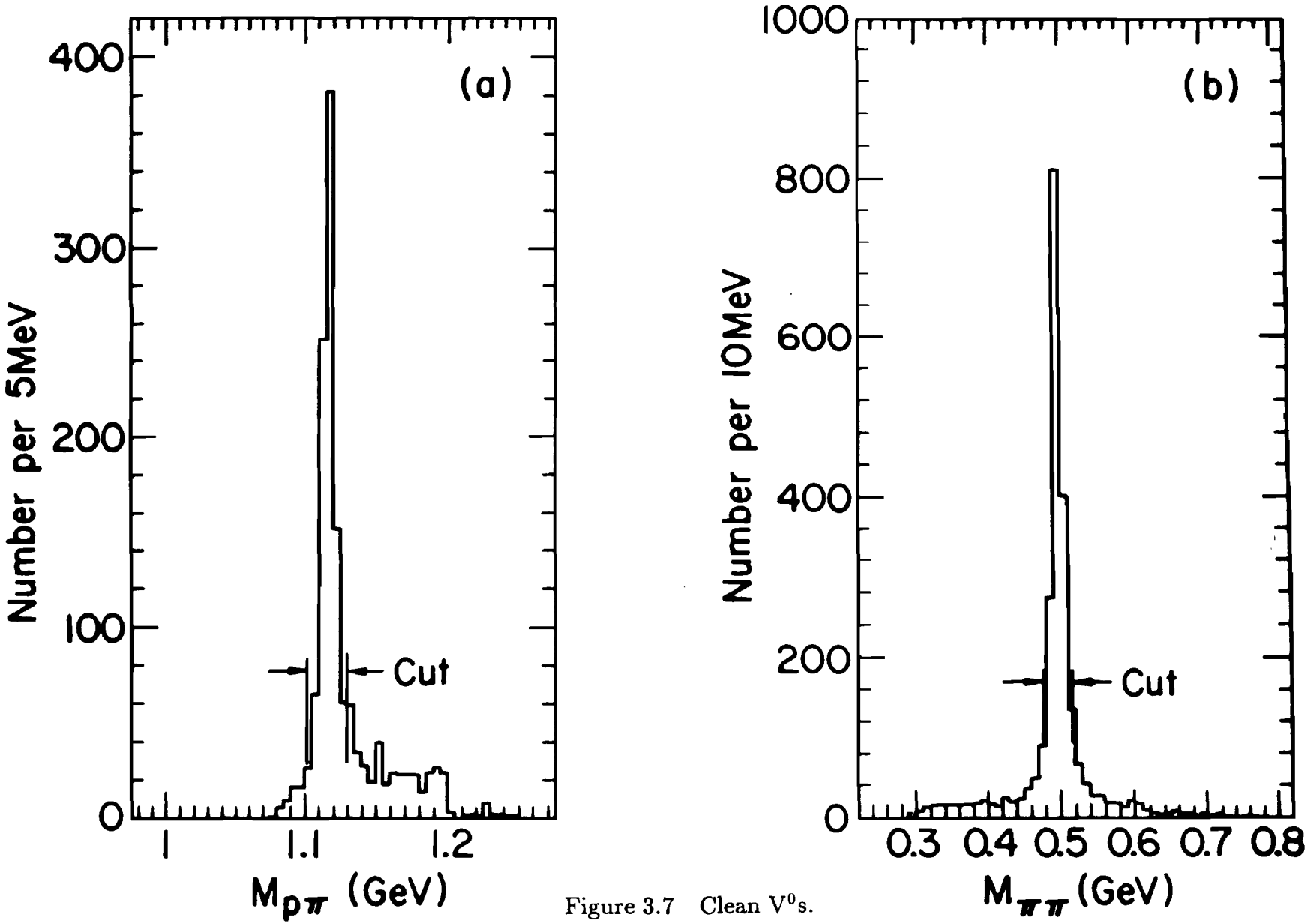

Figure 3.7 Clean V^0s.

CHAPTER 4

The $D^{*\pm}$ Signal

4.1 Introduction

The physics skim described in the previous chapter includes the selection of the charmed meson, $D^{*\pm}$, for the case in which it decays to a D^0 charmed meson with the subsequent decay of the D^0 to a pair of oppositely charged particles. I observe a $D^{*\pm}$ signal in the medium-energy, high multiplicity trigger (run numbers 4450 to 4973) of our 800 GeV run by application of an analysis cut based on the mass difference between the $D^{*\pm}$ and the D^0. The use of this type of cut is a common procedure[28] in charm meson analysis. The particular D^0 decay mode which I observe is $D^0 \rightarrow K^+K^-$. The kaons are identified by application of the Čerenkov analysis program. In particular, I allow the kaon to be either uniquely identified or to be in the K/P ambiguous category described in the previous chapter. The logical "or" of LOGIC and CERAL is used. The pion from the $D^{*\pm}$ decay is not required to be uniquely identified, but must be consistent with the pion hypothesis.

Figures 4.1(a), 4.1(b), and 4.1(c) are mass plots for $(K^+K^-)\pi^\pm$, (K^+K^-), and $(K^+K^-)\pi^\pm - (K^+K^-)$ combinations, respectively, selected from the physics skim data set. It is observed that these plots present no significant evidence for a signal. Thus, the Čerenkov selection alone does not have the sensitivity in E400 to isolate, for instance, the inclusive $D^0 \rightarrow K^+K^-$. Evidence for a signal does appear, however, when I cut one of these plots with the known charm mass region from another of the plots.

Figure 4.2 is a mass difference plot with the requirement that the $(K^+K^-)\pi^\pm$ invariant mass be in the range 1.995 to 2.03 GeV/c^2. I use throughout this chapter an adaptation of the CERN program MINUIT to fit the data with a third-order

polynomial background and a gaussian signal. It is found that an enhancement in the mass difference occurs at 145.1 ± .5 MeV/c^2 (the world average[16] is 145.45 ± .07 MeV/c^2 for the $D^{*\pm} \rightarrow D^0\pi^\pm$ decay) when the $(K^+K^-)\pi^\pm$ invariant mass is cut from 1.995 GeV/c^2 to 2.030 GeV/c^2, a range about the known $D^{*\pm}$ mass (2.0101 ± .0007 GeV/c^2), but that other choices for the $(K^+K^-)\pi^\pm$ invariant mass do not produce an enhancement in the $(K^+K^-)\pi^\pm - (K^+K^-)$ mass plot. The number of events found for Figure 4.2 is 82 ± 16 and the width is 1.1 ± .5 MeV/c^2.

Figure 4.3(a) is the corresponding (K^+K^-) invariant mass plot subject to the requirement that the $(K^+K^-)\pi^\pm - (K^+K^-)$ mass difference be in the range 144 to 147 MeV/c^2. As expected, there is an enhancement in the vicinity of the world average[16] D^0 mass (1.8646 ± .0006 GeV/c^2). The fit to Figure 4.3(a) yields 134 ± 19 events, which gives a statistical significance in excess of seven standard deviations. The fit yields a mean mass of 1.872 ± .005 GeV/c^2, which is consistent within errors with the known mass of the D^0. The width of this signal is 18 ± 3 MeV/c^2.

Figure 4.3(b) is a plot for the $(K^+K^-)\pi^\pm$ invariant mass subject to the same mass difference cut as in Figure 4.3(a). The mean mass for the $D^{*\pm}$ signal found in the fit is 2.017 ± .004 GeV/c^2, which is consistent with the known value. The number of $D^{*\pm}$ events found is 129 ± 21, which is consistent with the number of events found for Figure 4.3(a) and has a significance of 6.1 standard deviations. The width, 19 ± 5 MeV/c^2, is similar to the width found for the $D^{*\pm}$, which would be expected because the width of the mass difference plot is tiny compared to 19 MeV/c^2. The $(K^+K^-)\pi^\pm$ mass cut which has been imposed on Figure 4.2 covers approximately ± 1 standard deviation from the mean mass found for the $D^{*\pm}$ in Figure 4.3(b), and thus it is expected that the size of the signal in Figure 4.2 should be 68 % of 129 ± 21, or 88 ± 14 which is consistent with the observed fit result to Figure 4.2 of 82 ±

16 (less than $\frac{1}{2}\sigma$ discrepancy).

Figures 4.4(a) and 4.4(b) are D^{*+} and D^{*-} mass plots with yields 57 ± 12 and 69 ± 15, mass means 1.872 ± .006 GeV/c^2 and 1.873 ± .006 GeV/c^2, and widths 19 ± 5 MeV/c^2 and 18 ± 4 MeV/c^2, respectively. This yields the charge ratio $\frac{N(D^{*+}\to D^0\pi^+)}{N(D^{*-}\to D^0\pi^-)} =$ .83 ± .25, which is consistent with equal production of particle and antiparticle.

The only analysis cuts which are necessary to either the $D^{\pm}$ or the D^0 signal are the Čerenkov and mass difference cuts described above. It was not necessary, for instance, to restrict the multiplicity (other than the upper value of 19 already imposed by the size of arrays in our reconstruction program). The tracks which enter this sample have been "cleaned" by the skim requirements (the χ^2 requirements in the tracking and vertexing).

4.2 The Monte Carlo

The E400 simulation routines were used in the analysis of the cross sections by unfolding triggering effects as well as the geometric and analysis cut effects on the acceptance of particular charmed states. The trigger was not on the total neutron energy, but the energy of particles outside the central hole of the calorimeter and within the solid angle accepted by the apparatus, so the model used to generate the particles which accompanied the charmed state affected the acceptance calculation. The analysis cut effects depended primarily on the energy of the state, but also on the assumptions about the types of particles that were accompanying the charmed particle (which affected the Čerenkov confusion and the reconstruction program).

The simulation was divided into two programs:

1. HADNEW – the event generator, coded at University of Illinois.
2. GEANT – a simulator of track interactions with the detector, a generalized CERN simulation program.

HADNEW was generally run on a VAX at the user institution. Because of the time it required to process an event (order one minute on a VAX), GEANT was run on the faster CYBERs at FNAL.

I now give an overview of the event generation. The simulation of charmed particle production by HADNEW was based on a gluon-gluon fusion model[29] of the differential cross section in which the incident projectile neutron emitted a parton (gluon in this model) which fused with a parton (gluon) emitted by the target. The parton energies were then removed from the generated event energy, and the remaining energy was fragmented into two Feynman-Field jets. The charm-anticharm quark pair produced by gluon-gluon fusion were hadronized into charmed particles (e.g., $D^{*\pm}$ plus a recoil). The recoil particle to the charmed state under study was (in my case) chosen to be a charmed meson distributed under a variety of expected decay modes according to the probability (branching fraction) of the decay mode. I used such a generic charm recoil particle for all charmed meson states I studied.

There were three inputs to this model:

1. G(x) – the gluon momentum distribution within the nucleons,

$$x \cdot G(x) \propto (1-x)^N \tag{1}$$

   where N was chosen to have a value between three and six and x ranged from zero to one.
2. M_c – the mass of the charm quark, chosen to be 1.5 GeV/c^2.
3. f(z) – the dressing function, described by a variable $z \equiv$ momentum fraction of the charm quark going to a meson; E400 used a dressing which goes as z^2, where z ranged from 0 to 1.

When choosing N=5 for the parton distribution, HADNEW produced charmed particles with a soft x_f distribution:

$$\frac{d\sigma}{dx_f} \propto (1-|x_f|)^8 \tag{2}$$

A high multiplicity distribution is produced (the multiplicity of regular 800 GeV collisions is superimposed), which grows as $\sqrt{s}$ – the partons are soft and take little out of the event energy. In the next chapter, the agreement between the background multiplicity and the simulated multiplicity will be shown. This agreement made possible Monte Carlo simulations of multiplicity cuts for those states which required such cuts to reduce the combinatoric background (which was not necessary for this signal).

The GEANT simulation tracked the generated particles through the detector according to a user-supplied tracing program which implemented the appropriate device geometries and magnetic field distributions.

A simulated data tape which was generated was then processed through the E400 data reduction programs described in chapter three. When an event was generated, the wire hits were stored in a common block which was passed through the analysis chain. This allowed tracks found by the reconstruction program to be matched against those which were generated in HADNEW, by checking the number of hits which overlapped. The background could then be suppressed by requiring tracks entering a mass plot histogram to be the original tracks produced by the Monte Carlo. A resulting clean Monte Carlo charm signal could then be analyzed to determine the acceptance of a particular decay mode as a function of the charmed particle's energy or x_f, or to compare the properties of the candidate signal observed in data with the expected properties from the Monte Carlo (e.g., the widths should be comparable).

Figure 4.5 is representative of the resulting simulated D^0 signal. It should be noticed that the mean of the mass is five MeV/c^2 above the world average (the events were generated at the level of HADNEW with mass 1865 MeV/c^2) – I find 1.870 GeV/c^2 from the Monte Carlo. This is consistent with 1.872 $\pm$ 3 GeV/c^2, the result from the data. The various types of charm states I investigated had slightly high

masses, as did the Monte Carlo simulations of those states. Because of various state dependent effects, some signals investigated by other researchers had a larger offset from the relevant world-average mass. The Monte Carlo width of the D^0 is 15 MeV/c^2 and agrees well with the data.

Figure 4.6(a) is the acceptance curve as a function of the energy of the $D^{*\pm}$ and Figure 4.6(b) is the acceptance curve as a function of the x_f of the $D^{*\pm}$. The curves fall off as the energy approaches 100 GeV because of the upper momentum limit of 40 GeV/c for Čerenkov identification of kaons. The first step in generating these curves was to histogram the total number of events formed (without requiring that they be geometrically accepted) by HADNEW, subject to a cut which required that the neutron energy be above 300 GeV in order to simulate the minimum energy requirement of our hardware trigger. The second step was to create a GEANT based PASS3 tape from these events, and histogram the charm state subject to analysis cuts and the energy bussline (neutron energy requirement) of the trigger. The analysis cuts in this Monte Carlo study are the same as those described in section 4.1 which were used in the data to observe the $D^{*\pm}$ signal.

E400 parameterized the acceptance two ways. One was in terms of the energy of the state, the other was in terms of the x_f of the state. The two methods were employed as checks against each other in finding the cross section. In the x_f method, the x_f was measured on an event by event basis using calorimetry and thus the event yield was divided by the acceptance parameterized in terms of x_f. In the energy weighting method, a similar event by event examination of the state energy resulted in the acceptance in bins of energy (to which a smooth curve could be fit as for the x_f case) and the parameterization was thus in terms of the state energy. In order to express the energy weighting method as a differential cross section in x_f, the measured

state energy was related to x_f by means of an effective neutron energy, E_{eff}^{neutron} which best expresses the correlation between state energy and x_f in the Monte Carlo. Figure 4.7 is a Monte Carlo generated plot of the $D^{*\pm}$ energy versus its x_f. For high energies (above 100 GeV) there is difficulty getting events because of the Čerenkov acceptance of our detector, but the fit is generally a good one. The resulting best value of E_{eff}^{neutron} varies from one charm state to another (they have different acceptance properties) so this number should be determined for each state independently. On this simulated data I have overlaid three curves (for three values of E_{eff}^{neutron} - 450, 550, and 625 GeV), which have been generated by the relation:

$$x_f = E^{D^*}/E_{eff}^{\text{neutron}} - M_\perp{}^2/(2 \times M_{\text{neutron}} \times E^{D^*}) \tag{3}$$

$$\text{where } M_\perp{}^2 = M_{\text{D}^*}{}^2 + P_\perp^2 \tag{4}$$

for several effective values of the neutron energy. A typical value for $P_\perp$ of the charm particles is found to be .75 GeV/c. I find that using 550 GeV for the effective neutron energy gives a close fit.

4.3 Determination of the Nuclear Dependence

It is interesting to measure the relative charm production rate of the three targets as a fit to the form A^α, where a measurement of α close to 2/3 indicates a predominately diffractive model while α close to "1" is indicative of hard parton collisions. It is also necessary to understand this dependence in order to make an absolute measurement of the cross section. I can compare the number of charm events N_i^{measured} that I observe to be produced in each target material in order to derive the value of α by forming a χ^2 fit to the hypothesis that $N_i \propto A^\alpha$:

$$\chi^2 = \sum \left((N_i^{\text{predicted}} - N_i^{\text{measured}})^2/\sigma_i^2 \right) \tag{5}$$

The predicted number of charm events, $N_i^{\text{predicted}}$, is dependent on the density ρ_i, thickness t_i, and atomic weight A_i of the three target materials (W, Be, and Si) as

given by the following relation:

$$N_i = \frac{N_{\mathrm{tot}} \cdot \rho_i t_i A^{(\alpha-1)})}{(\sum_i \rho_i t_i A^{(\alpha-1)})} \tag{6}$$

where N_{tot} is the sum of the events observed for the three target materials. The error used to calculate the χ^2 is the observed error on the area of the $D^{*\pm}$ or D^0 signal from a given target material. In this sample, the bin which represents the tungsten target is the one with the least significance – there are 45 ± 14 events for Be, 39 ± 9 for Si, and 31 ± 10 events for W. Figures 4.8(a), 4.8(b), and 4.8(c) are charm signals in Be, Si, and W, respectively.

The χ^2 depends on two parameters – N_{tot} and α. When the minimization of χ^2 is performed, the best values of these parameters are found to be $N_{tot} = 114$ (which is consistent with the observed sum of 115) and $\alpha \approx 1$. Figure 4.9(b) shows the variation of χ^2 with respect to α. It is found that the χ^2 increases above minimum by one unit for $\alpha = .96 +/- .17$. The minimum χ^2 is small, but that is because there is one degree of freedom (three bins from the three target materials, and the two parameters).

The result that $\alpha \approx 1$ suggests that $D^{*\pm}$ production is consistent with incoherent hard scattering off individual partons rather than the coherent diffractive process. Although the error on this measurement is uncomfortably large and by itself is not extremely strong evidence against consideration of the diffractive mechanism, a number of other measurements[30] of α have been made by E400 researchers for production of particular charm decay modes other than the $D^{*\pm}$, and the mean measured value of α is typically in the range $.9 \leq \alpha \leq 1.$ with an error of ± .1. We cannot dispute the possibility of some exotic process which would give a value for α in excess of 1.

4.4 Determination of the $D^{*\pm}$ Cross Section

I will compare several estimates of the the branching ratio × cross section for $D^{*+} \rightarrow D\pi^+ \rightarrow (K^+K^-)\pi^+$. Basically, the approach (for further explanation see

Appendix B) computes the acceptance corrected event yield by fitting a (reciprocal) acceptance weighted mass histogram for all events with non-negligible acceptance. The acceptance includes a portion derived from Monte Carlo which includes geometrical acceptance,Cerenkov and other analysis cuts, and the energy busline as determined from Monte Carlo . An additional acceptance factor for the M7 efficiency correction is applied using the antecedent method which is deduced from the number and types of observed particles within an event. The resulting acceptance probabilities from the M7 subject to these input antecedents is summarized in Table B.1 of Appendix B. The cross section estimates differ in both the parameterization of the acceptance in terms of either state momentum or state x_f (utilizing calorimetry information), and in the choice of kinematic range over which there is "reasonable" acceptance for this state. My conclusion is that the cross section estimates are robust against changes in both the kinematic range and acceptance parameterization.

Figure 4.10 is a fit to the x_f weighted K^+K^- mass. On an event by event basis I have corrected for the M7 and the acceptance as determined by the fit to Figures 4.6. The average efficiency is 5.2 %. The relative error in the acceptance weighted yield is 20.5 % while the relative error in an unweighted yield is 14.4 % which indicates that the weighting procedure introduces additional uncertainties in the yield as one would expect but there is not a significant degradation over the x_f range employed (there is little observable data in the regions excluded, and upper and lower cuts are necessary to keep some fluctuations in the low acceptance regions from influencing the cross section estimates). The acceptance corrected yield is 2598 $\pm$ 533 events, hence the resulting cross section ($\times$ branching fraction) from $0 < X_f < .14$ is:

$$\sigma \cdot BR = \frac{1}{2}\, 13.722 \times 10^{-3} \text{ barns} \cdot \frac{2598}{(183.22 \times 10^6)(.39896)(.82)} = 0.299\mu b \quad (7)$$

The choice of these factors is explained in Appendix B. The factor of $\frac{1}{2}$ represents

the fact that we are averaging over the D^{*+} and D^{*-} cross section, and are reporting on the D^{*+} inclusive cross section under the assumption of symmetric particle and antiparticle production. The 13.722 mB factor represents the portion of the target averaged inelastic neutron cross section which will fire the master gate under an A^1 nuclear dependence assumption. The various denominator factors represent the total targeted luminosity (183.22×10^6), livetime (.39896), and spectral factor (fraction of the neutron spectrum above 300 GeV – .82 in our case).

This can be compared to the method using the acceptance as a function of state energy. To facilitate comparison, I have cut on the energy to be 37→92 GeV which corresponds to the previous x_f range according to the x_f versus E curve (which gives an effective mean neutron energy of 550 GeV). The acceptance corrected yield now becomes 2187 which implies a $BR \cdot \sigma(0 < X_f < .14)$ of 0.252 μB representing a discrepancy of about 17 % which is well within the errors of the separate measurements.

I have also investigated the effects of choosing different energy ranges on the energy weighting method cross section estimates. The data is presented as the differential cross section $BR \cdot \frac{d\sigma}{dx}(\bar{x})$ where $\bar{x}$ is the x_f value which is in the center of our acceptance. The value $BR \cdot \frac{d\sigma}{dx}(\bar{x})$ is nearly independent of the presumed x_f dependence of the charm cross section. In the range N=0 to N=8, the variation is 10%. This allows a comparison of the method with different x_f ranges in a reasonable way. The differential cross section is computed using the formula:

$$BR \cdot \frac{d\sigma}{dx} = BR \cdot \sigma_{tot} \left(\frac{N+1}{2} \right) (1 - |\bar{x}|)^N \quad \text{where} \quad \bar{x} = \frac{x_2 + x_1}{2} \tag{8}$$

$BR \cdot \sigma_{tot}$ is deduced from $BR \cdot \sigma(x_1 \rightarrow x_2)$ by appropriate integration of the $(1 - |x|)^N$ form. Table 4.1 summarizes $BR \cdot \frac{d\sigma}{dx}$ measurements for four energy ranges and for the one x_f range used in the x_f weighting scheme. Agreement is rather impressive.

Figure 4.9(a) demonstrates the variation of the cross section with the choice of α. It is seen that this dependence is quite dramatic and gives a systematic error on the order of 30 % when α is varied from 1 by about 10 %. As will be seen in the next chapter, the other systematic effects combine to give a comparable error.

The cross section found above using the x_f method has been compared[14] to the cross section found independently for another decay mode of the D^0 in which the observed form of the decay products is a pair of K^0_s's. The motivation for this comparison was noted in chapter 1. The resulting ratio $\frac{\Gamma(D^0 \to K^0 \bar{K}^0)}{\Gamma(D^0 \to K^+ K^-)}$ is 0.4 ± 0.3, which is consistent with the theoretical estimate given by Pham[15]. The two decay modes were compared over the same x_f region for consistency. The error on the ratio is large because of the more limited x_f region which my state has due to the upper energy acceptance imposed by the Čerenkov requirements for the charged kaons. This reduced the size of the other decay mode sample used in the comparison.

Table 4.1 $D^{*+} \rightarrow D\pi^+ \rightarrow (K^+K^-)\pi^+$.

$BR \cdot \sigma$ Estimates at $< E_{neut} >= 550\ GeV$.

P range	X range	$BR \cdot \sigma(X_1 \rightarrow X_2)$	$BR \cdot \frac{d\sigma}{dX}(\bar{X})$	$\bar{X}$
(GeV)		(μB)	(μB)	
30 - 100	(-.03 → .16)	.275 ± .06	1.49 ± .33	.065
40 - 80	(.01 → .12)	.179 ± .05	1.72 ± .47	.063
45 - 75	(.03 → .10)	.147 ± .04	1.92 ± .56	.066
37 - 92	(0. → .14)	.252 ± .06	1.79 ± .43	.071
X_f Method	0. → .14	.299 ± .06	2.11 ± .43	.070

1. All errors quoted are statistical only.
2. All cross sections quoted assume A^1 dependence.
3. Cross sections are average of D^{*+} and D^{*-} cross sections.
4. The branching ratio (BR):

$$BR \equiv BR(D^* \rightarrow D\pi) \times BR(D \rightarrow K^+K^-)$$

is defined relative to all possible decay modes.

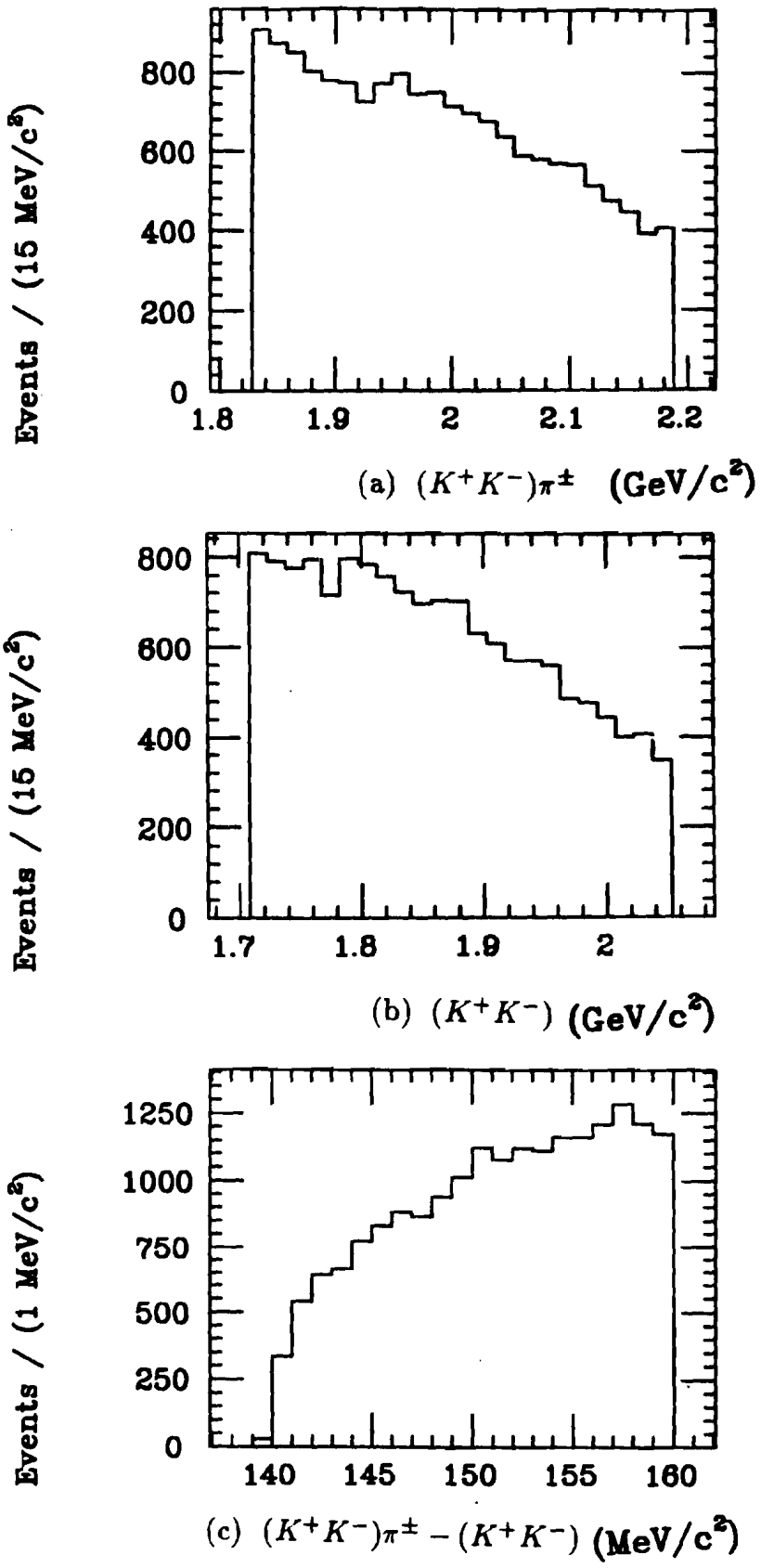

Figure 4.1 Mass plots from skim, no analysis cuts.

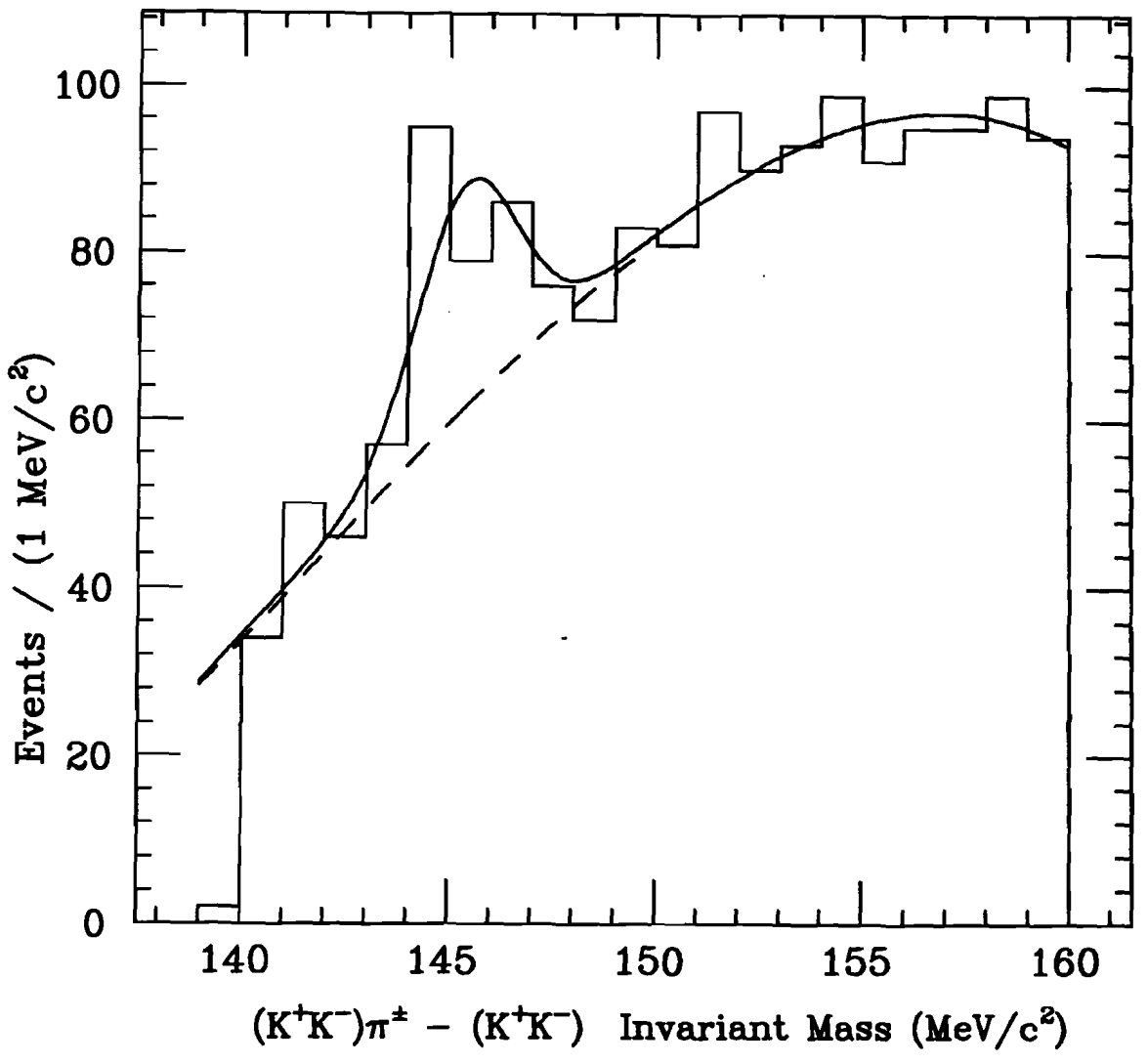

Figure 4.2 $(K^+K^-)\pi^\pm - (K^+K^-)$ invariant mass subject to analysis cuts.

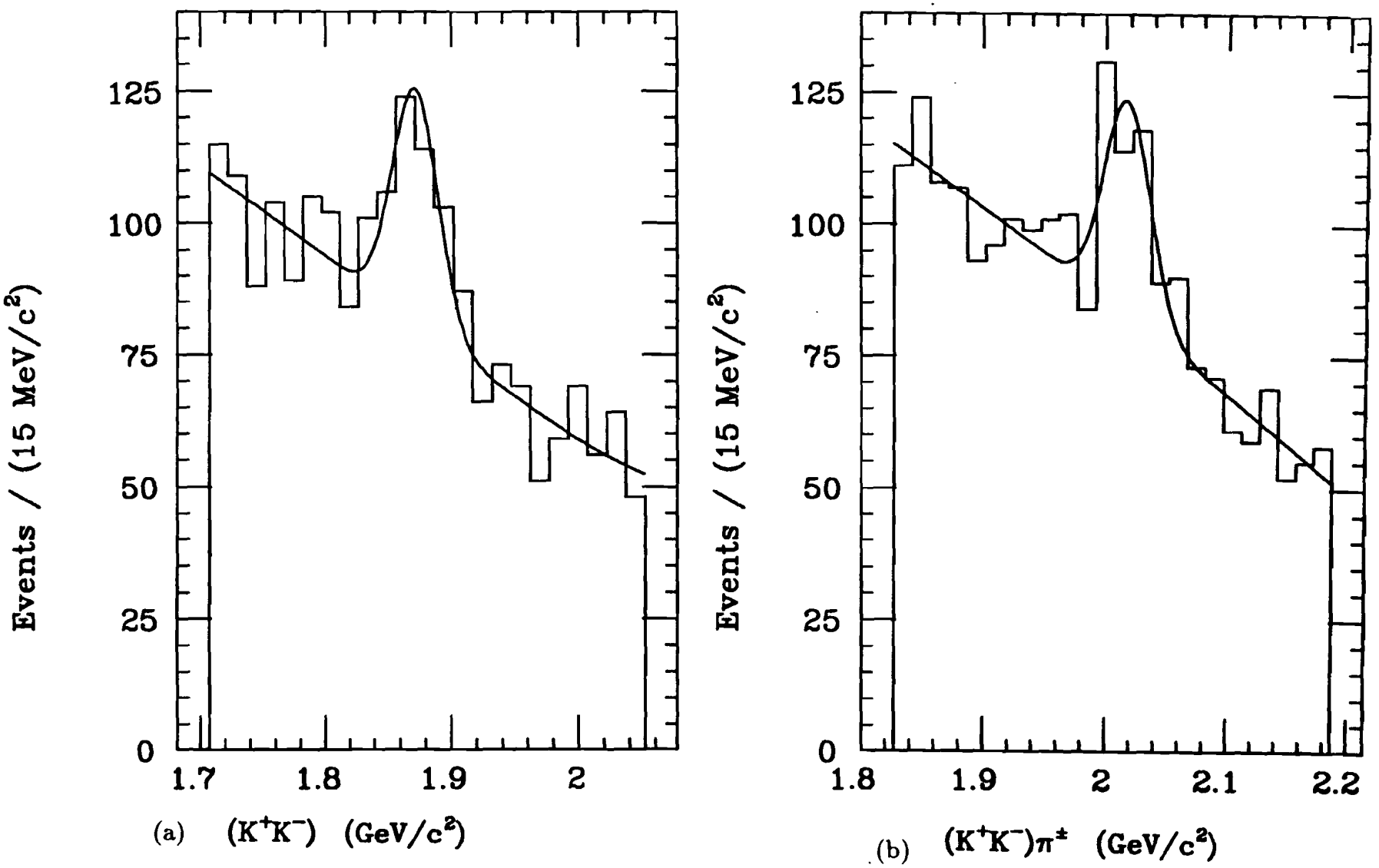

Figure 4.3 Mass plots subject to analysis cuts.

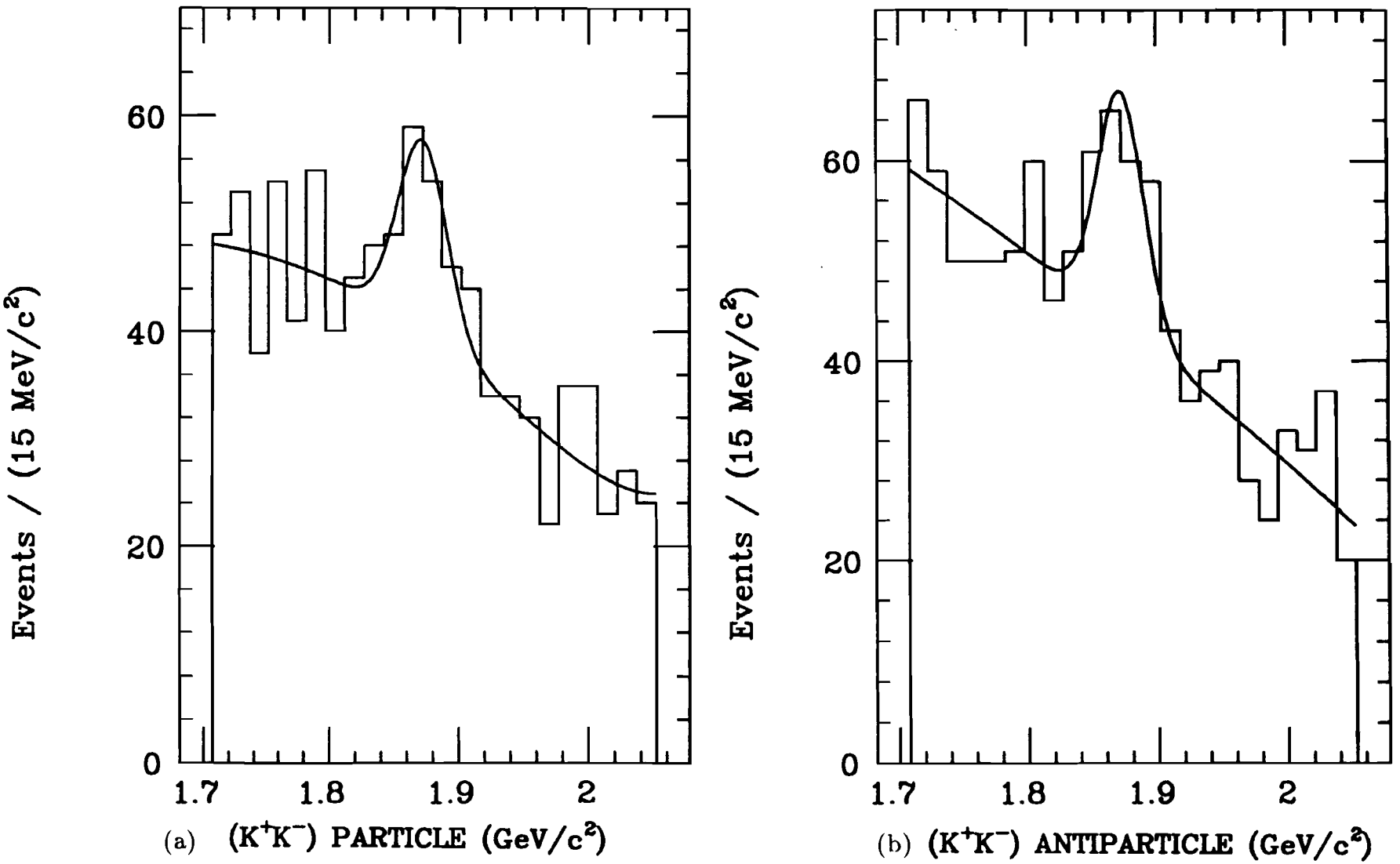

Figure 4.4 $(K^+K^-)\pi^\pm$ analysis plots according to charge.

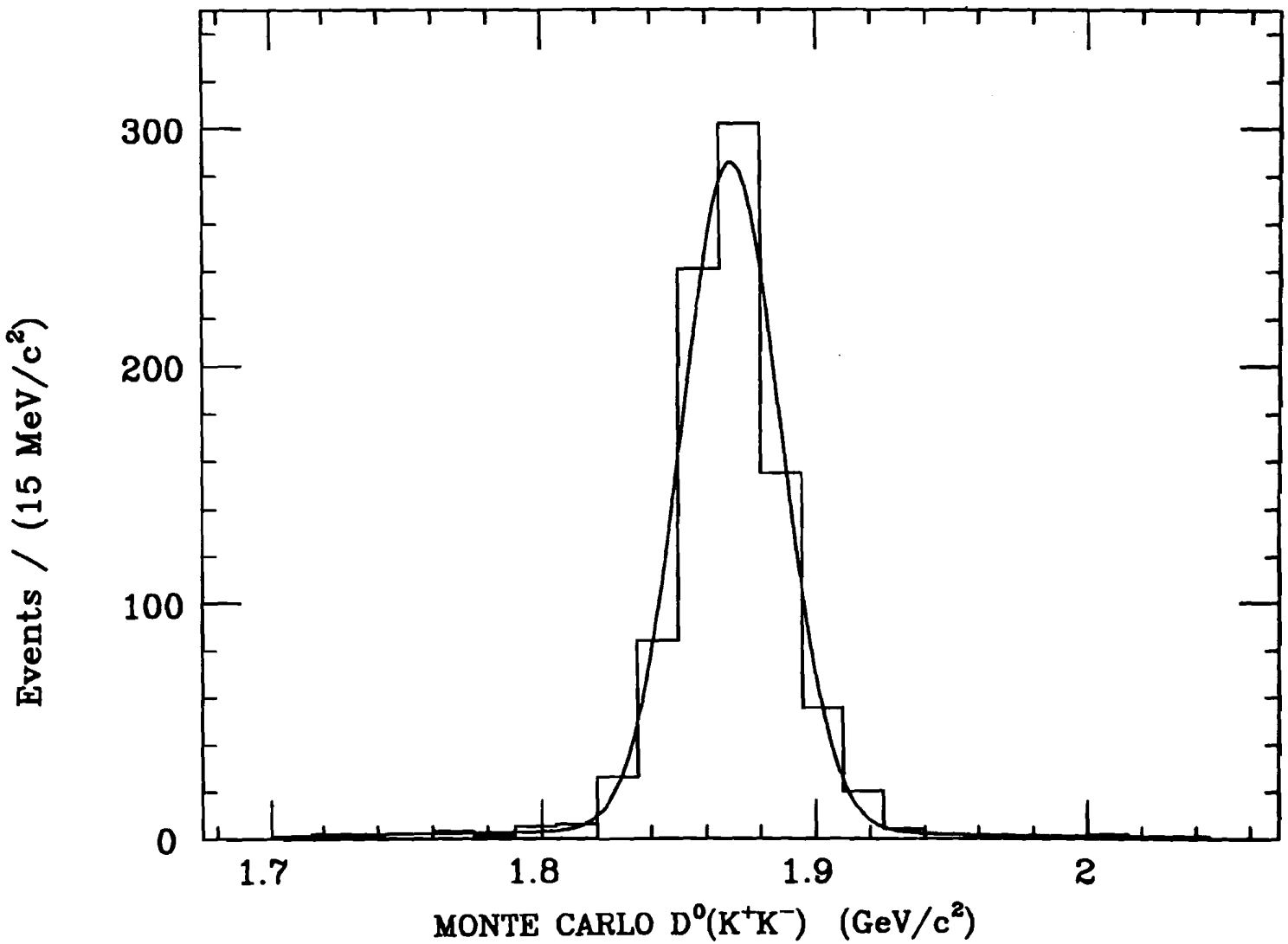

Figure 4.5 D^0 generated by Monte Carlo.

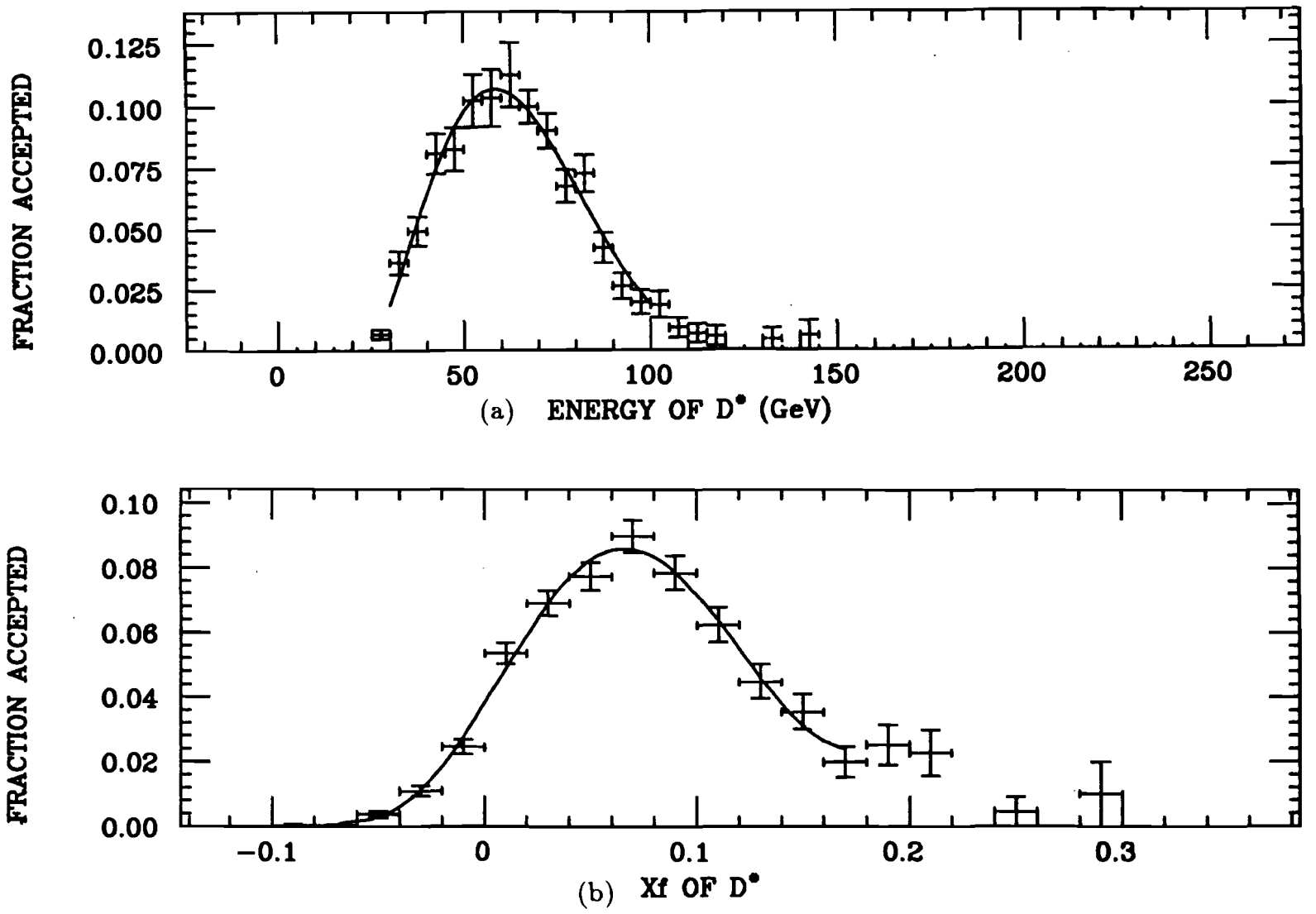

Figure 4.6 $D^{*\pm}$ acceptance curves generated by Monte Carlo.

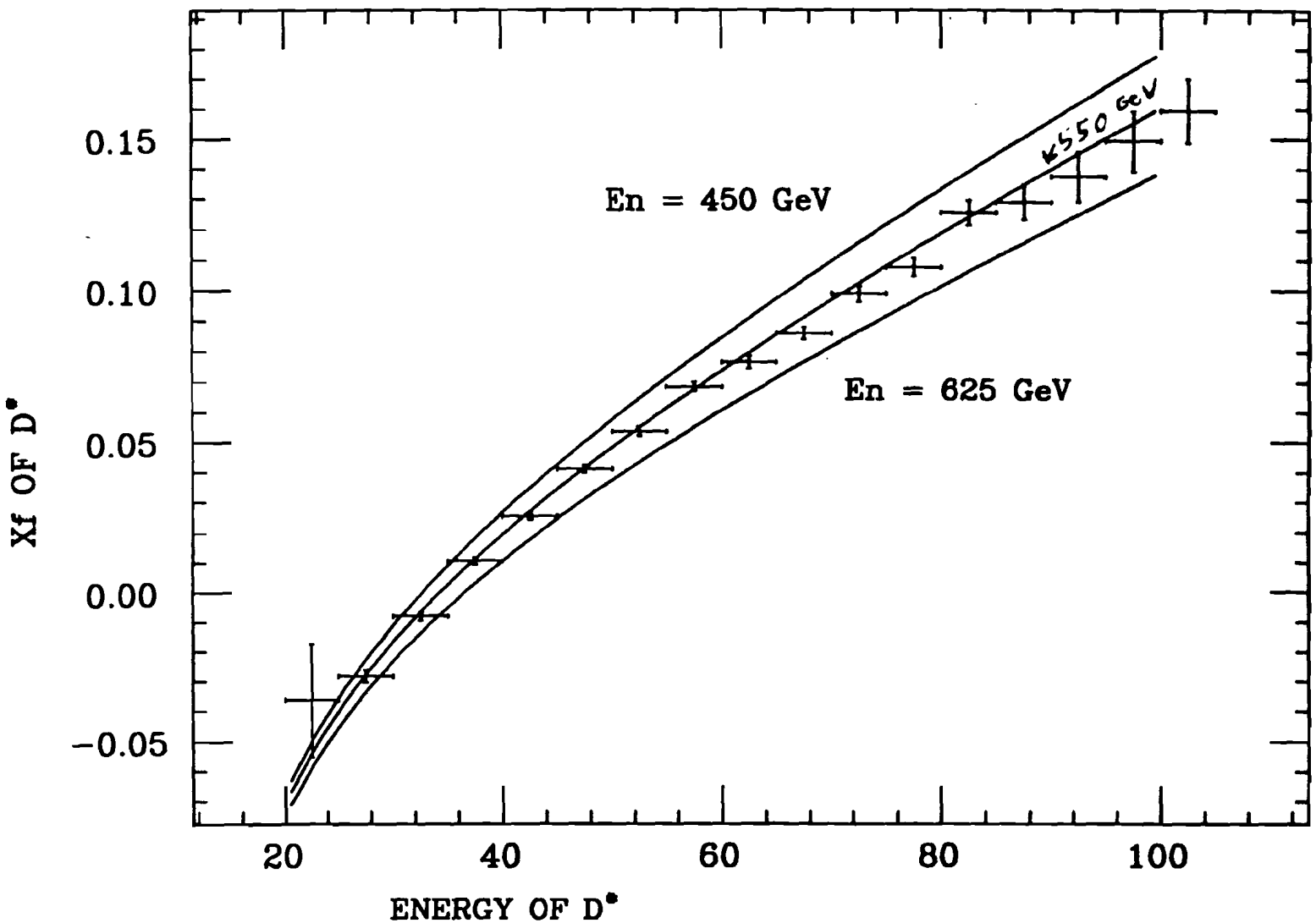

Figure 4.7 Simulation of state energy vrs x_f.

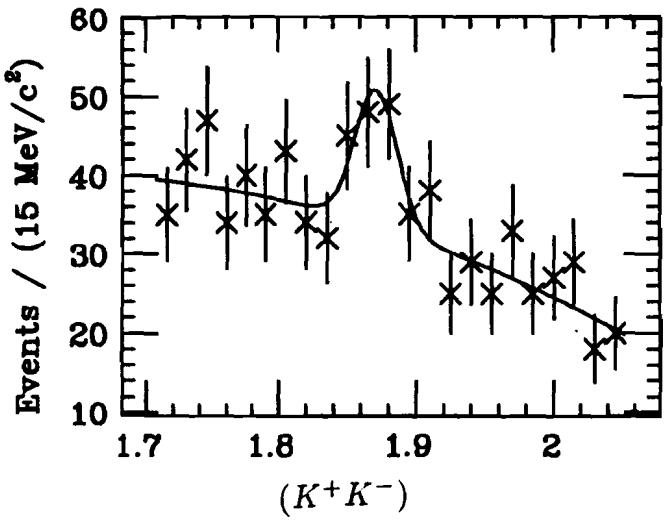

(c) Charm signal – beryllium.

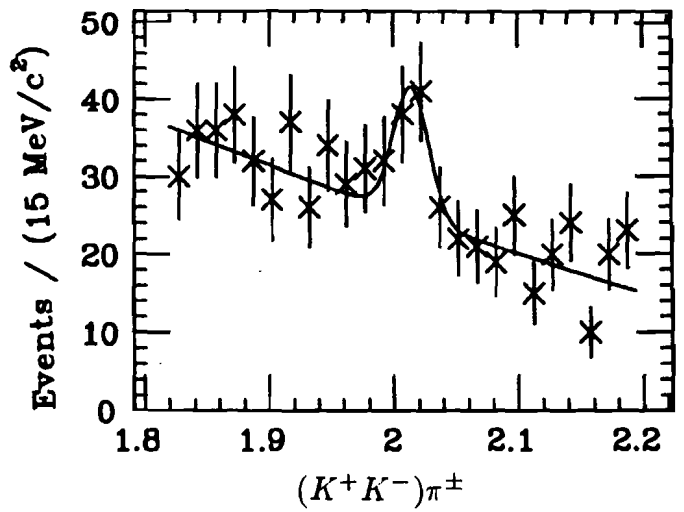

(b) Charm signal – silicon.

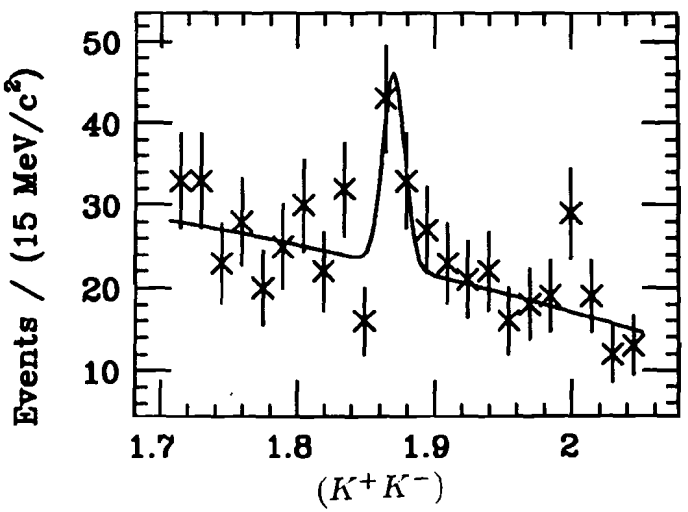

(a) Charm signal – tungsten.

Figure 4.8 Signals in various targets.

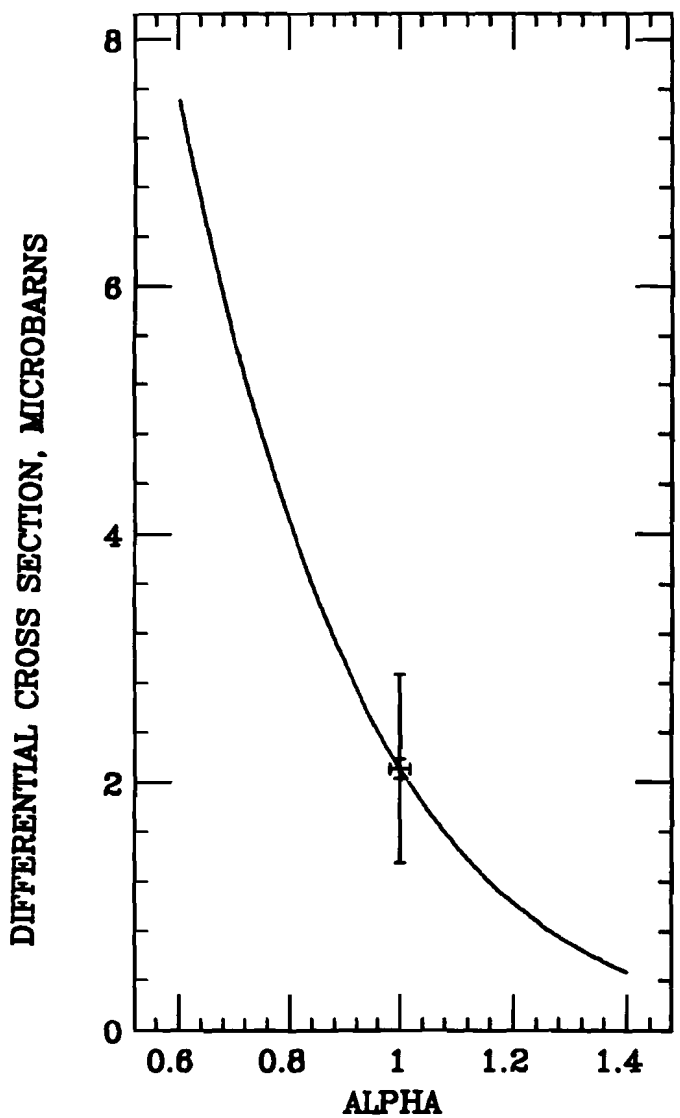

(a) Cross section variation with α.

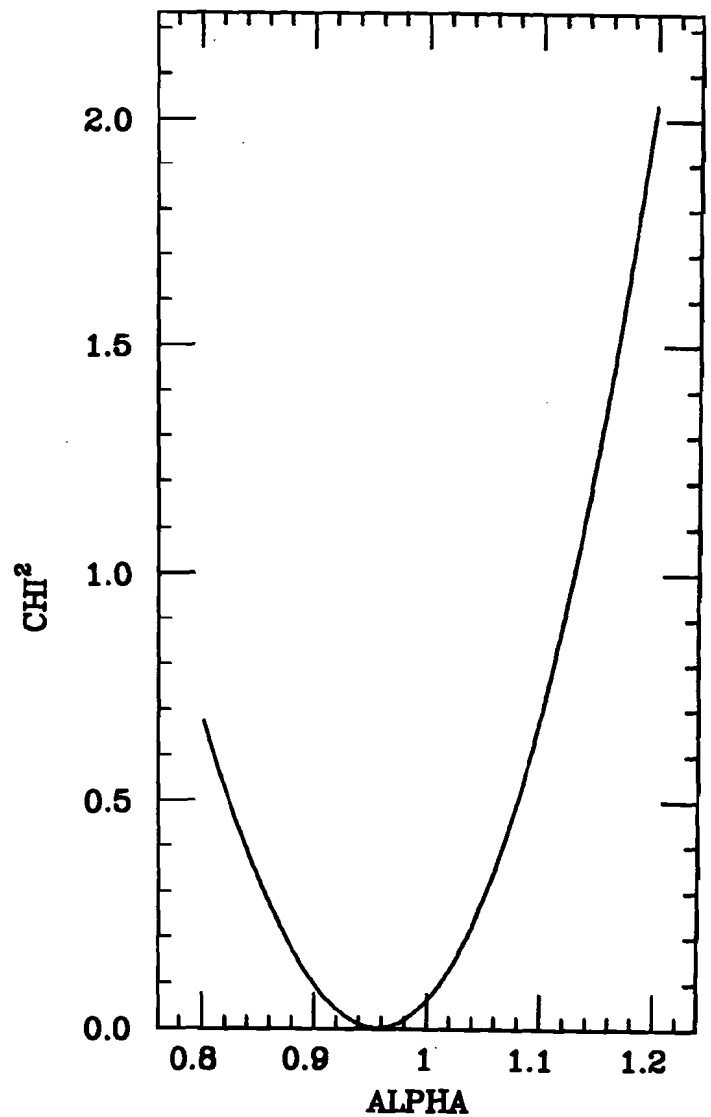

(b) Determination of α.

Figure 4.9 α functions.

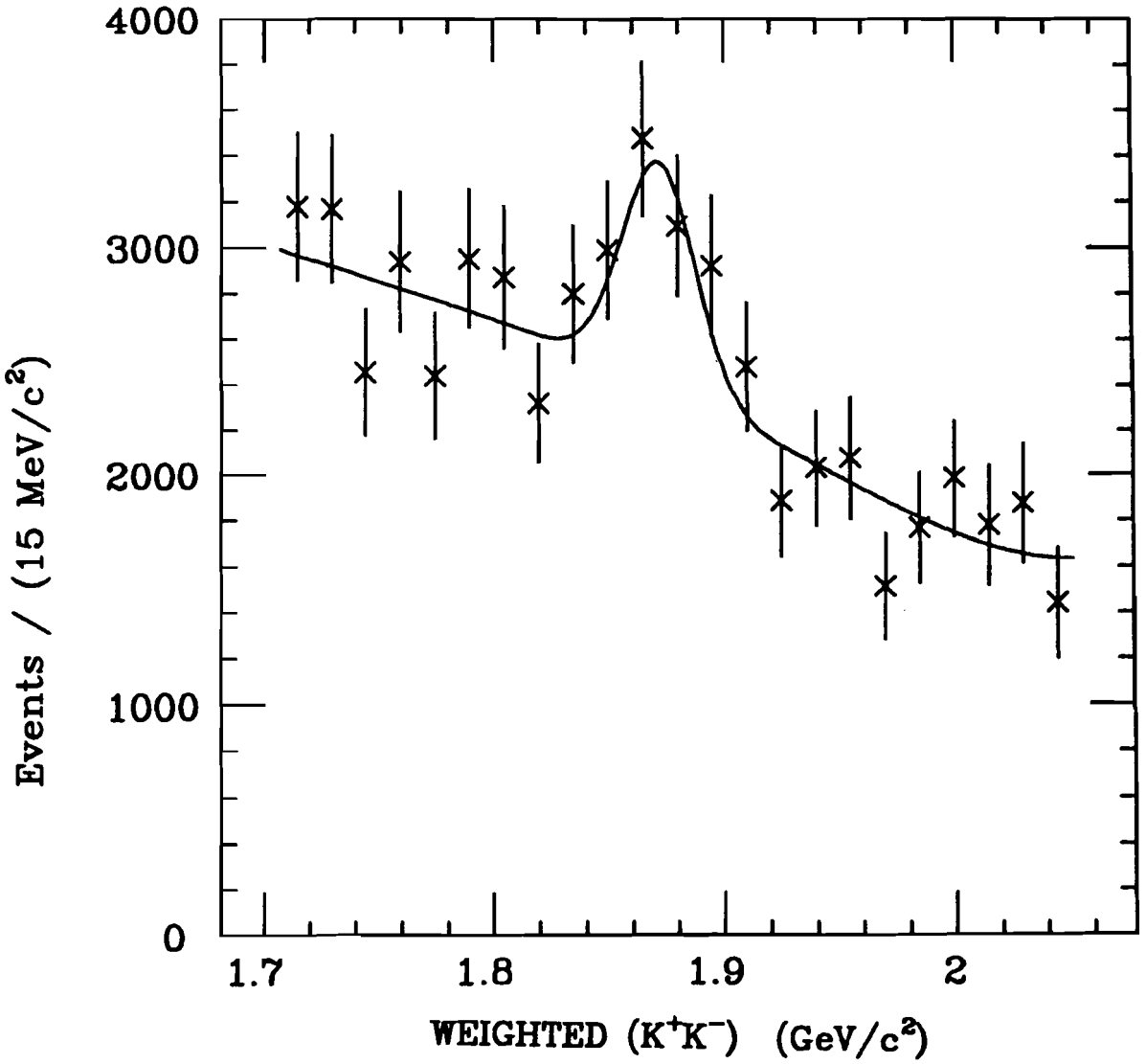

Figure 4.9 x_f weighted K^+K^- invariant mass.

CHAPTER 5

The $D_s^{\pm}$ Signal

5.1 Introduction

In this chapter I present the results of my observation of the $D_s^{\pm}$. The charmed meson states $D_s^{\pm}$ are observed in the decay modes $D_s^{\pm} \rightarrow \phi\pi^{\pm}$ and $\phi \rightarrow K^+K^-$. Figure 5.1 shows a K^+K^- invariant mass distribution with a prominent ϕ signal. Each kaon candidate is required to be uniquely Čerenkov identified (i.e., unambiguous with either the pion or proton hypothesis) by the logical "or" of LOGIC and CERAL to make the fullest use of the particle identification analysis. Because this state has a natural width comparable to our spectrometer resolution, I have performed the fit to the signal by the convolution of a Breit-Wigner shape, of fixed width[16] 4.22 MeV/c^2, with a Gaussian distribution, found to be of width 1.73 $\pm$ .05 MeV/c^2. The background has been fit by a third-order polynomial. The result is a very strong, very clean sample of 33,000 candidates with a mean mass at 1.0195 $\pm$ .00003 GeV/c^2. The ϕ candidates for the charm search are selected by applying a K^+K^- mass cut of 1.0195 $\pm$ .0035 GeV/c^2. This cut passes the majority ($\approx$ 75%) of the ϕ candidates while maintaining a strong signal-to-noise ratio.

To perform the $D_s^{\pm}$ search , these ϕ candidates were combined with charged tracks, assuming a $\pi^{\pm}$ mass. Tracks positively identified as either a kaon or proton using information from the Čerenkov counters were excluded. The resulting $\phi\pi^{\pm}$ invariant mass histogram is shown in Figure 5.2. A multiplicity requirement of less than 14 tracks has been applied to reduce the combinatoric background. This distribution has been fit with a Gaussian peak representing $D_s{}^{\pm} \rightarrow \phi\pi^{\pm}$ decay over a smooth background. I have included an additional peak located near the known

D^+ mass in order to represent the $D^\pm \rightarrow \phi\pi^\pm$ process. The width of the $D_s^\pm$ and $D^\pm$ peaks were constrained to be identical. The fit gives 65 ± 29 $D_s^\pm$ candidates with a mass of 1.981 ± .005 GeV/c^2 and a width of 8.5 ± 2.7 MeV/c^2 , and also 69 ± 38 $D^\pm$ candidates with a mass of 1.873 ± .008 GeV/c^2.

For the decay $D_s^+ \rightarrow \phi\pi^+$, the angle θ between the K^+ and the π^+, when viewed in the ϕ rest frame, is expected to follow the distribution given by $\frac{dN}{dcos\theta} \propto cos^2\theta$. The rather significant forward-backward peaking present in the $cos\theta$ distribution (see Appendix C) can be exploited to improve the signal to background ratio in the $D_s^\pm$ search, because our spectrometer has flat acceptance in θ.

Figure 5.3 is a fit to the $\phi\pi^\pm$ invariant mass histogram requiring that $|\cos\theta| \geq .5$. The result of this fit to the observed signal is 64 ± 16 $D_s^\pm$ events for a significance of 4.0 standard deviations. The mass is 1.972 ± .005 GeV/c^2 and the width is 8.4 ± 3.5 MeV/c^2 , which is consistent with our detector resolution for this state. The fit also gives 47 ± 23 $D^\pm$ events at the mass 1.876 ± .004 GeV/c^2. Comparison of the data of Figures 5.2 and 5.3 shows that (98 ± 37)% of the $D_s^\pm$ signal and only 50 % of the background survives the $cos\ \theta$ cut. The survival fraction obtained in the data for the signal is consistent with the expected value of 87.5 % obtained by integrating the $D_s^\pm \rightarrow \phi\pi^\pm$ angular decay distribution.

5.2 Monte Carlo Results

In Figure 5.4, a mass histogram for a small sample of $D_s{}^\pm \rightarrow \phi\pi^\pm$ has been generated by the E400 adaptation of the CERN Monte Carlo program known as GEANT. The same cuts which were used to reveal the signal in the data were applied to the Monte Carlo generated data tape. Specifically, these are the requirements given above for event multiplicity, Čerenkov identification, and the angular distribution of the $\pi^\pm$ with respect to the $K^\pm$ in the ϕ center of mass frame. Figure 5.4 is a

mass histogram for "signal" $\phi\pi^{\pm}$ events which are selected by having a reconstructed chamber hit pattern matched to the generated hit pattern contained in the GEANT God's block.

The multiplicity distribution of the Monte Carlo events are compared with the data in Figures 5.5(a) and 5.5(b). Figure 5.5(a) is the multiplicity distribution of the data, and is subject to all of the analysis cuts (excluding the multiplicity cut) and is also cut on the $D_s^{\pm}$ mass, over the range 1.960 to 1.980 GeV/c^2, in an effort to make the histogram demonstrate the characteristics of the $D_s^{\pm}$ signal rather than just show the distribution of the multiplicity of the background. Figure 5.5(b) is the distribution of a large sample of simulated $D_s^{\pm}$ events, and has the same analysis cuts which have been applied to Figure 5.5(a).

It is found that the Monte Carlo generated signal has a resolution width of approximately 10 MeV/c^2, which is consistent with that of the experimentally observed candidate signal. The mean mass of the $D_s^{\pm}$ signal in the data is observed to be only a few MeV/c^2 higher than the currently accepted world-average for this value[16], as is also the case for the fit to the Monte Carlo signal of Figure 5.4 (mean mass 1.977 GeV/c^2) which has been generated assuming a world-average value (1.970 GeV/c^2). Thus, the value of the mass in the data is consistent with the value found by the Monte Carlo (which employs the same description of the magnetic field as is used in the analysis of the data). The slight increase observed in the mean mass, from the world-average, could be a result of any light systematic error introduced by the magnetic tracing programs used in the analysis of the actual data multiple scattering, or bias introduced by the analysis cuts as is indicated by the difference in mean mass of the $D_s^{\pm}$ between Figure 5.2 and 5.3. This effect is probably dependent on the event topology and state momentum, and may affect some signals more than others. The

value of the mean mass found in the $D_s^{\pm}$ signal in the data is well within the systematic error, 20 MeV/c^2, which is estimated from the numerous other observations of charm signals which researchers in the E400 collaboration have reported. In general, those observations have depended on more severe cuts than has been necessary for this analysis, and they could therefore be expected to deviate more from their respective accepted world-averages than is the case for the $D_s^{\pm}$.

In order to calculate the cross section for $D_s^{\pm} \rightarrow \phi\pi^{\pm}$, it is necessary to know what fraction of the $D_s^{\pm}$ events generated in the neutron-nucleus collisions has been reconstructed by our analysis package after traversing the E400 experimental detector. This acceptance fraction is a function not only of the detector geometry but also of the decay particles' momenta. The acceptance for this state can be found from the Monte Carlo by dividing the results of the above Monte Carlo generated histogram by another Monte Carlo histogram with the same binning but which now represents the total number of $D_s^{\pm}$ particles which have been generated prior to the application of the analysis cuts. In the process of doing this, one must be careful to apply a cut to both histograms which mimics the effects of the E400 trigger on the data. Specifically, this amounts to reproducing the results of the pin which has been formed from the hardware busslines described in Chapter 2. As described there, this includes the energy trigger as well as the multiplicity requirements, and therefore a cut must be imposed which requires that the minimum neutron energy is above 300 GeV. The acceptance can be calculated as a function of either the energy or the x_f of the $D_s^{\pm}$ candidates. The result is shown in Figure 5.6.

Figure 5.7 is a determination of the average neutron energy for the state $D_s^{\pm}$. In chapter 4 I have explained the general use of this quantity, and the weighting methods. I have generated a plot of energy versus x_f for a Monte Carlo sample of $D_s^{\pm}$. I then

overlaid this plot with curves described by the following relation:

$$X_f = \frac{E_{Ds}}{E_n} - \frac{M_\perp^2}{2M_n E_{Ds}} \tag{1}$$

where $M_\perp = \sqrt{M_{Ds}^2 + P_\perp^2}$, $M_n = .939GeV$,and E_n , E_{Ds} are the lab energy of the neutron and $D_s^\pm$, respectively. By superimposing such curves for neutron energies of 350, 450, and 550 GeV I find that 450 GeV is the most reasonable choice of average neutron energy for this state to use when performing the cross section measurement.

5.3 Determination of the $D_s^\pm$ Cross Section

I have obtained an estimate for $BR \cdot \sigma$ for the $D_s{}^\pm \rightarrow \phi\pi^\pm$ process in the region $0.05 < x_f < 0.30$ by dividing the acceptance corrected event yield (4734 ± 1333) of Figure 5.8 by the luminosity determined by counting relatively unbiased inelastic neutron interactions originating in the target. The details of how this method is implemented in general for this experiment are given in Appendix B. For reference, the number of neutrons on target for this analysis is 2.58×10^8 with a livetime of .43650. It should be noted here that the effects of the M7 trigger, described in Chapters 3 and 4, have been included in this acceptance correction. The x_f for a given combination was computed from the measured energy of a $D_s^\pm$ candidate, and the incident neutron energy as reconstructed through calorimetry. Here $BR \equiv \Gamma(D_s{}^\pm \rightarrow \phi\pi^\pm)/\Gamma(D_s{}^\pm \rightarrow \text{all})$, and the cross sections are presented with the value .495 for the branching fraction $\Gamma(\phi \rightarrow K^+K^-)/\Gamma(\phi \rightarrow \text{all})$ incorporated. A relatively model independent measurement of the corrected event yield was made by fitting a weighted $\phi\pi^\pm$ invariant mass distribution for all combinations which satisfy the particle identification, angular distribution, and multiplicity cuts. The combinations entering this histogram were individually weighted by the reciprocal of the $D_s^\pm$ acceptance, which was parameterized as a function of $x_f(D_s^\pm)$ alone, and in this way averaged over all other relevant production and decay variables.

As a check, I obtained an alternative acceptance corrected event yield by fitting a weighted $\phi\pi^{\pm}$ mass distribution for $D_s^{\pm}$ candidates with weights parameterized in terms of the measured the $D_s^{\pm}$ energy rather than x_f. I required events to have a $D_s^{\pm}$ energy between 45 and 145 GeV – an energy range chosen to correspond to the previous x_f range at our average neutron energy of 450 GeV. This alternative yield estimate was found to be completely consistent but 15 % lower than the yield estimate from the x_f parameterized acceptance correction technique. The consistency of these two methods was extensively demonstrated by Table 4.1 using the case of the $D^{*\pm}$ signals I studied in the previous chapter. Table 5.1 presents several results for the D_s^{+}.

The sample luminosity was measured by counting the number of unbiased neutron interactions as recorded by the coincidence between the target region scintillation counter and downstream scintillation hodoscope and dividing by the previously measured[31] topological cross sections averaged over our target materials after correction for triggering losses (0.15) and livetime (0.40). I find a partial cross section of $BR \cdot (\sigma(D_s^{+}) + \sigma(D_s^{-})) = 1.51 \pm .43$ μb/nucleon in the range $0.05 < x_f < 0.30$, where I have assumed a linear A dependence for the hadronic charm cross section. This assumption is based on the results found in Chapter 4 for the A dependence of the $D^{*\pm}$. It is not feasible to perform the same analysis on the $D_s^{\pm}$ sample due to the much smaller number of observed events.

Figures 5.9(a) and 5.9(b) are the $D_s^{\pm}$ signals (with all the analysis cuts applied) broken down according to negative or positive charge of the pion, respectively. Under the negative charge sign I find 22 $\pm$ 16 events with a mean mass of 1.974 $\pm$ .007 GeV/c^2 and a width of 9 $\pm$ 5 MeV/c^2, while under the positive charge sign I find 42 $\pm$ 15 events with a mean mass of 1.972 $\pm$ .005 GeV/c^2 and a width of 9 $\pm$ 4

MeV/c^2. These results are consistent with the fit of Figure 3, which represents the sum of charges. Therefore, within the kinematic region covered by the x_f cut, I find the ratio of charges to be:

$$\frac{N(\mathrm{D}_s^+ \to \phi\pi^+)}{N(\mathrm{D}_s^- \to \phi\pi^-)} = 1.9 \pm 1.5 \tag{2}$$

which is consistent with symmetric particle and antiparticle production. This uncertainty reflects the growing problem of fluctuations as one subdivides a small sample of events, and is indicative of the difficulties encountered when trying to divide the sample into three parts to attempt a straightforward analysis of the A dependence. Under this symmetric production assumption , the D_s^+ inclusive production cross section would be $BR \cdot \frac{1}{2}(\sigma(\mathrm{D}_s^+) + \sigma(\mathrm{D}_s^-)) = .76 \pm .21$ μb/nucleon. Correcting for the x_f range, the differential cross section is:

$$BR \cdot \frac{1}{2}\left(\frac{d\sigma(D_s^+)}{dx_f} + \frac{d\sigma(D_s^-)}{dx_f}\right) = 2.85 \pm 0.80 \ \pm .86 \ \mu\mathrm{b/nucleon \ at} \ x_f = 0.175$$

In addition to the statistical error ($\pm$ .80) I have included a systematic uncertainty in the cross section of $\approx$ 30% due to errors in the luminosity ($\pm$20%), model dependence ($\pm$20%), and differences due to the parameterization of the acceptance ($\pm$10%). This value assumes a nuclear dependence of the form $\mathrm{A}^{1.0}$. As was shown in Chapter 4, the cross section is sensitive to the value of α assumed for the nuclear A^α dependence. I did not measure α for this signal, but it would be expected that, as was the case for the $\mathrm{D}^{*\pm}$, a $\pm$10% change of α about 1.0 would result in a $\pm$30% change in σ.

5.4 Comparison of the $\mathrm{D}_s^\pm$ with other Charm Mesons

Although the significance of the $\mathrm{D}^\pm \to \phi\pi^\pm$ signal present in Figure 3 is only $\approx$ 2 standard deviations, it may be of interest to compare the yield of $\mathrm{D}_s^\pm$ and $D^\pm$ events. Correcting the raw number of signal events obtained from the fit of Figure

3 for possible differences in $D_s^{\pm}$ and $D^{\pm}$ acceptance and triggering efficiencies using the weighting method described earlier in this chapter, an acceptance corrected event fraction is found: $N_{D^{\pm}}/(N_{D^{\pm}} + N_{D_s^{\pm}}) = .38 \pm .17$, where both $N_{D^{\pm}}$ and $N_{D_s^{\pm}}$ refer to the number of decays observed in the $\phi\pi^{\pm}$ decay mode over the x_f range from 0.05 to 0.30. Use has been made of the result that Figure 5.8 has been fit for the $D^{\pm}$ as well as the $D_s^{\pm}$, and it was found that there are 2848 ± 1919 and 4734 ± 1333 events, respectively.

If I use $BR(D_s) = 3.6\%$ and introduce a correction factor of 3.26 to account for the limited x_f range, I get a crude estimate of the total cross section for $D_s^+ \rightarrow \phi\pi+$:

$$\frac{1}{2}(\sigma(D_s^+)+\sigma(D_s^-)) = \frac{1}{2}(3.26/.036)(BR(D_s)\cdot\sigma(D_s^{\pm})) = 68\pm19 \ \pm20 \ \mu\text{b/nucleon} \quad (4)$$

I have used the assumption that $\frac{d\sigma}{dx_f} \propto (1-|x_f|)^{4.5}$. Using this cross section, our ratio $N_{D^{\pm}}/(N_{D^{\pm}} + N_{D_s^{\pm}})$, and $BR(D) = 1\%$ I make a very crude estimate of the $D^+ \rightarrow \phi\pi+$ cross section:

$$\sigma(D^+) = (68)\cdot\frac{N_{D^{\pm}}}{N_{D_s^{\pm}}}\cdot(.036/.01) = 148 \pm 77\mu\text{b/nucleon} \quad (5)$$

where the large error is due to the low significance of the $D^{\pm}$ signal. This cross section is only approximately two standard deviations from zero and therefore has low significance.

It is interesting to compare the value for the hadronic D_s^+ production cross section to the hadronic cross section for other charmed particles. The value presented in Chapter 4 for the measured average of the D^{*+} and D^{*-} inclusive cross sections was found to be $BR\cdot\frac{d\sigma}{dx_f} = 2.11 \pm .43 \pm .63$ μb/nucleon at $x_f = 0.07$ in the decay sequence $D^{*+} \rightarrow D^0\pi^+$, $D^0 \rightarrow K^+K^-$. Extrapolating both the $D_s^{\pm}$ and $D^{*\pm}$ differential cross sections to $x_f = 0$ by assuming a common x_f dependence of the form $d\sigma/dx_f \propto$

$(1-|x_f|)^N$ with N=4.5, the following ratio is obtained:

$$\frac{B(D_s)\cdot\frac{d\sigma}{dx_f}(D_s)}{B(D^*)\cdot\frac{d\sigma}{dx_f}(D^*)} = 2.18 \pm 1.08 \text{ at } x_f = 0 \tag{6}$$

After correcting by the measured D^* branching ratio[16], $BR(D^*) = 0.314\%$, and a composite of estimates for the D_s , $BR(D_s) = 3.6\%$, the following ratio estimate is obtained:

$$\frac{\frac{d\sigma}{dx_f}(D_s)}{\frac{d\sigma}{dx_f}(D^*)} = 0.19 \pm 0.09 \text{ at } x_f = 0 \tag{7}$$

Errors have not been included on the relevant charm branching ratios since there is no reliable estimate of these errors for the $D_s \rightarrow \phi\pi$ decay mode.

5.5 Correlation of the $(\phi\pi^+)$ Submass with Antiprotons

An interesting observation I have made is the presence of statistically suggestive enhancements in the $\bar{P}(\phi\pi^+)$ invariant mass plot. Figure 5.10(a) is such a histogram over all 800 GeV triggers, subject to a cut on the $(\phi\pi^+)$ submass in the range 1.940 to 1.980 GeV/c^2 corresponding roughly to the D_s^+ mass. In addition to a possible enhancement of 85 $\pm$ 19 events centered at 2.966 GeV/c^2 with a width of 21 $\pm$ 4.4 MeV/c^2, there is also a bin at 3.200 to 3.220 GeV/c^2 which deviates suggestively from the background. Figure 5.10(b) is the same mass plot with several clean-up cuts imposed. These are:

1. The mass range is now centered better around the world-average; i.e., it is now 1.950 to 1.990 GeV/c^2.
2. The multiplicity has been required to be less than 15 to reduce the combinatoric background.
3. All of the decay particles have been required to have a clean-up radial attachment of within .15 inch of the vertex.
4. The data sample chosen has been restricted in 5.10(b) to the high multiplicity trigger within which the beam targeting was best stabilized (runs 4600 to 4973), although this removes only about 25 % of the runs.
5. The angular distribution cut was set at $|\cos\theta| \geq .6$ to remove more than half the background.

The peak around 3.200 GeV/c^2 now appears prominent, although the sample is admittedly small. The FWHM appears to be around 20 MeV/c^2. Effects which are very close to the threshold (below 3 GeV/c^2) are hard to distinguish from merely being some peculiarity in the behavior of the peak of phase space. I will therefore concentrate on looking for supporting behavior to the second mass (3.200 GeV/c^2) peak in the $\bar{P}(\phi\pi^+)$ plot. If I attempt to look for corroborating enhancements either in other decay modes of the $D_s^\pm$ or in other states which decay into $(\phi\pi^+)$, I also can find some enhancements.

There is evidence of enhancements in the case in which I cut on the $(\phi\pi^+)$ mass to be in a range (1.850 to 1.880 GeV/c^2) about the known D^+ mass; see Figure 5.11(a)). There may be an enhancement near the threshold, but there is strong indication of a peak around 3.050 GeV/c^2. This is interesting because it is 100 - 150 MeV/c^2 lower than the peak observed in Figures 5.10(b), and the D^+ has a mass 100 MeV/c^2 lower than the D_s^+. Figure 5.11(b) is a $(\phi\pi^+)$ mass plot which shows a strong enhancement near the D^+ mass after cutting on a $(\bar{P}(\phi\pi^+)) - (\phi\pi^+)$ mass difference (1.15-1.19 GeV/c^2) which corresponds to the peak near 3.050 GeV/c^2 (the 3.100 peak may also be used as the cut). This plot has been cleaned up by the multiplicity, angular, beam stability, and radial attachment cuts of Figure 5.10(b).

Cutting on the the second peak in Figures 5.10 (3.2 GeV/c^2), a statistically suggestive enhancement in the $(\phi\pi^+)$ histogram near the D_s^+ is revealed in Figure 5.12(a). In Figure 5.12(b) the mass difference between the $\bar{P}(\phi\pi^+)$ and $(\phi\pi^+)$ invariant masses is shown. This shows the narrowness of the state. The peak from 1.16 to 1.20 GeV/c^2 corresponds to the peak near 3.200 GeV/c^2 in Figures 5.10. Varying the mass difference cut slightly varies the emphasis on D_s^+ or D^+.

Figure 5.13(a) is the mass histogram for $\bar{P}(K_S^0K^+)$ cut around the D_s mass, and

5.13(b) is the $(K^0_S K^+)$ submass cut around 3.2 GeV/c^2 on the $\bar{P}K^0_S - K^+$ mass. A weak enhancement can be seen near 3.200 Gev/c^2 in 5.13(a), and possible indication of an enhancement near the D^+_s mass in 5.13(b). The K^0_S candidates in Figures 5.13 can fall within any of the V^0 attachment topologies possible under the physics skim requirement of being a "clean" K^0_S (described in chapter 3).

Figures 5.14 are the result of applying tighter analysis cuts (they demand that the K^0_S candidates have zero attached tracks to the vertex). In Figure 5.14(a), the $\bar{P}(K^0_S K^+)$ is cut with a $(K^0_S K^+)$ mass from 1.960 to 1.980 GeV/c^2. In Figure 5.14(b) there is a tight $\bar{P}(K^0_S K^+)$ mass cut from 3.210 to 3.220 GeV/c^2. In both 5.13 and 5.14 I have used all 800 GeV triggers to remove the possibility of run bias.

Figures 5.15(a) and 5.15(b) show Monte Carlo simulations of the $\bar{P}(\phi\pi^+)$ cut on the D^+ and the D^+_s, respectively. They match the shape of the background but the enhancement effect away from threshold is not distinguishable. This may be evidence that the $\bar{P}(\phi\pi^+)$ enhancement in the data is not a subtle kinematic trick of the detection efficiencies.

These $\bar{P}(\phi\pi^+)$ enhancements do not have a clear explanation. Although attempts to interpret the near-threshold enhancements as other than peculiarities associated with the peak of phase space may be difficult, the correlations seen for $\bar{P}(\phi\pi^+)$ and $(\phi\pi^+)$ plots around a mass difference of 1.15 - 1.2 GeV/c^2 are intriguing. Mutually correlated enhancements cannot be seen for all choices of the $(\phi\pi^+)$ submass. Although the number of events is small, it is somewhat difficult to dismiss these correlations entirely as just a fluctuation.

I began such a search when Bjorken suggested to E400 that the experiment search for certain "bound states" (or "molecular states") consisting of a charmed particle with another hadron with a low binding energy. Bjorken was motivated in part for his

model by the apparently large cross section E400 was reporting for a charm-strange baryon. I chose to look for the case I describe above ($\bar{P}(D^{+} or D_s^{+})$) because I had already begun planning a skim for the $D_s^{\pm}$.

I do not claim an explanation for the resulting observations described. One possibility is that they represent a hadron with some exotic combination of quarks ($\bar{q}\bar{q}\bar{q}q\bar{q}$), however because the existence of exotics would be a very important and unexpected discovery, one must be very conservative in making such claims. We do not intend to make such claims on the basis of the evidence presented here. The results are presented because they are tantalizing. We have had the tendency to dismiss the near threshold enhancements because threshold effects are tricky and we believe they could well be kinematic effects. Since the background is not really understood, estimating the significance is not possible. There do appear to be large standard deviation effects, which would be rare as fluctuations but not unheard of. The fact that a cut around the enhancements seems to show a rather clean charm signal seems to provide impressive additional evidence, but one must be careful that cross cutting on a bump seen in one is not circular evidence of one for the other. Since there is no definite apriori prediction of where to look for the mass, the significance of these effects would need to be quite large to be tenable.

Table 5.1 $D_s^+ \rightarrow \phi\pi^+$

$BR \cdot \sigma$ Estimates at $< E_{neut} >= 450\ GeV$

P range	X range	$BR \cdot \sigma(X_1 \rightarrow X_2)$	$BR \cdot \frac{d\sigma}{dX}(\bar{X})$	$\bar{X}$
(GeV)		(μB)	(μB)	
X_f Method	.05 → .3	.76 ± .21	2.85 ± .80	.175
X_f Method	.08 → .26	.48 ± .16	2.56 ± .87	.17
55 - 135	(.08 → .28)	.60 ± .19	2.83 ± .88	.18
45 - 145	(.05 → .3)	.66 ± .22	2.38 ± .78	.175

1. Statistical errors only.
2. Assumes A^1 dependence.
3. Cross sections are average of D_s^+ and D_s^- cross sections.
4. Branching ratio (BR) defined as:

$$BR \equiv BR(D_s \rightarrow \phi\pi)$$

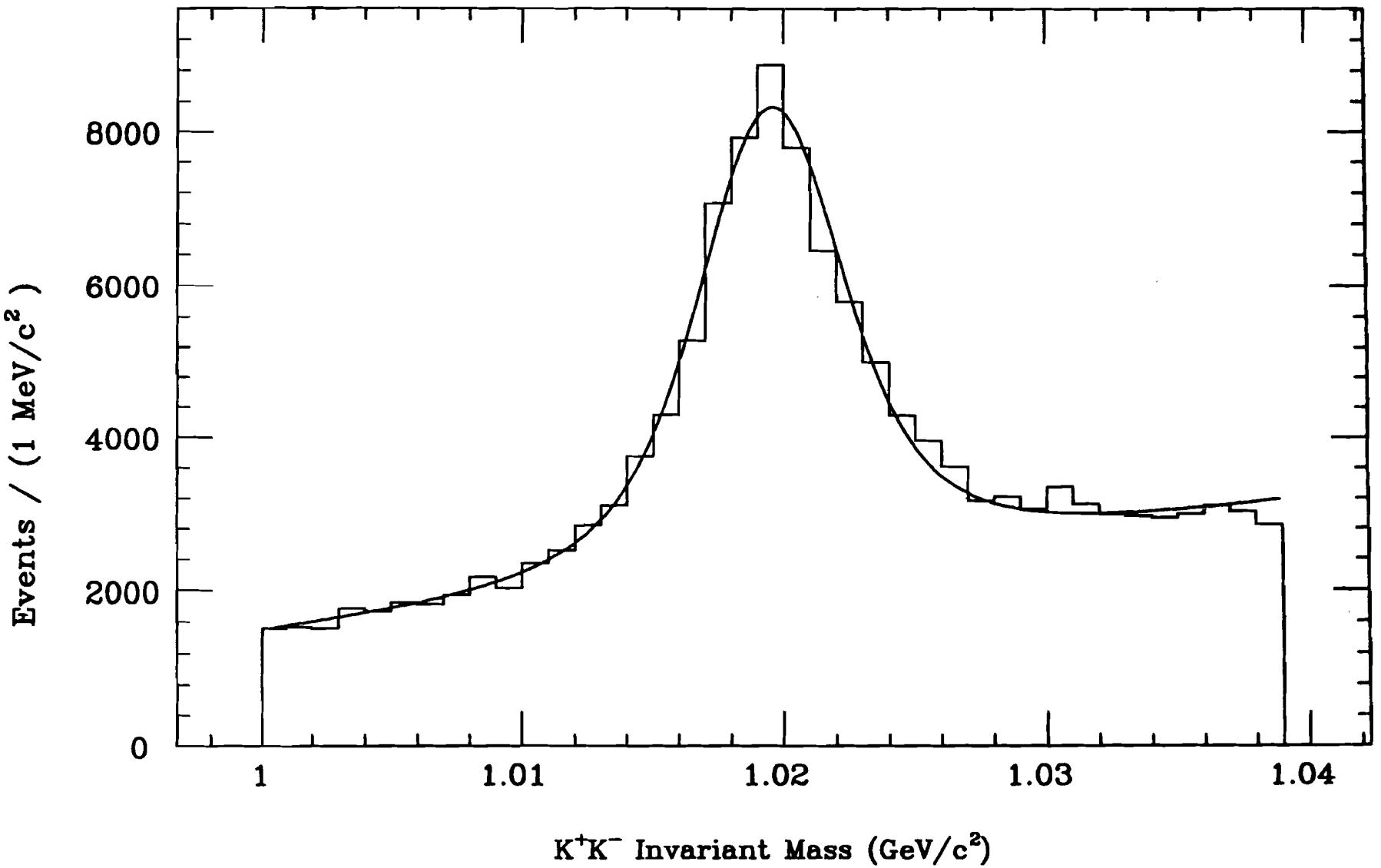

Figure 5.1 K^+K^- invariant mass.

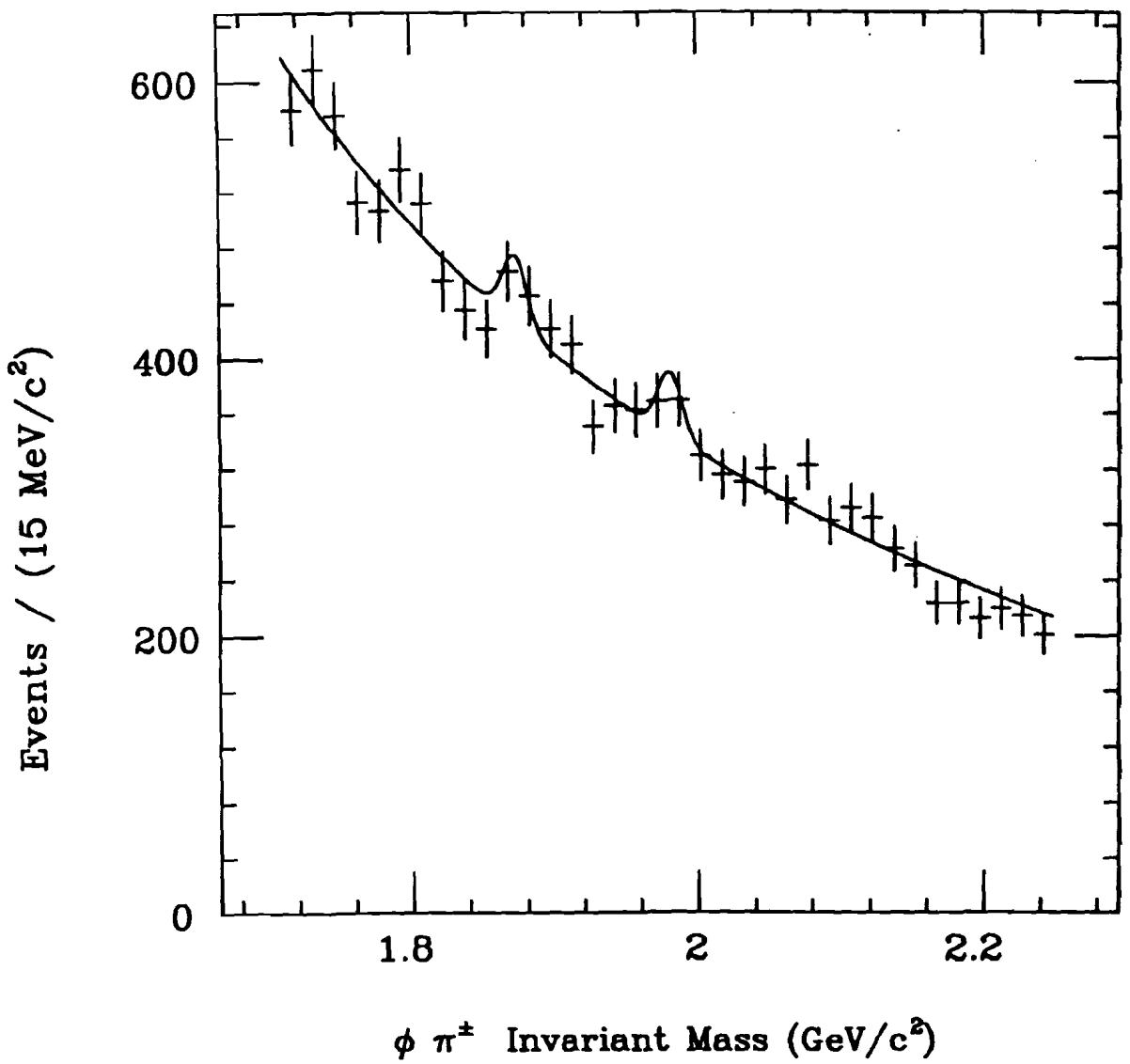

Figure 5.2 $\phi\pi^{\pm}$ invariant mass subject to analysis cuts except angular distribution.

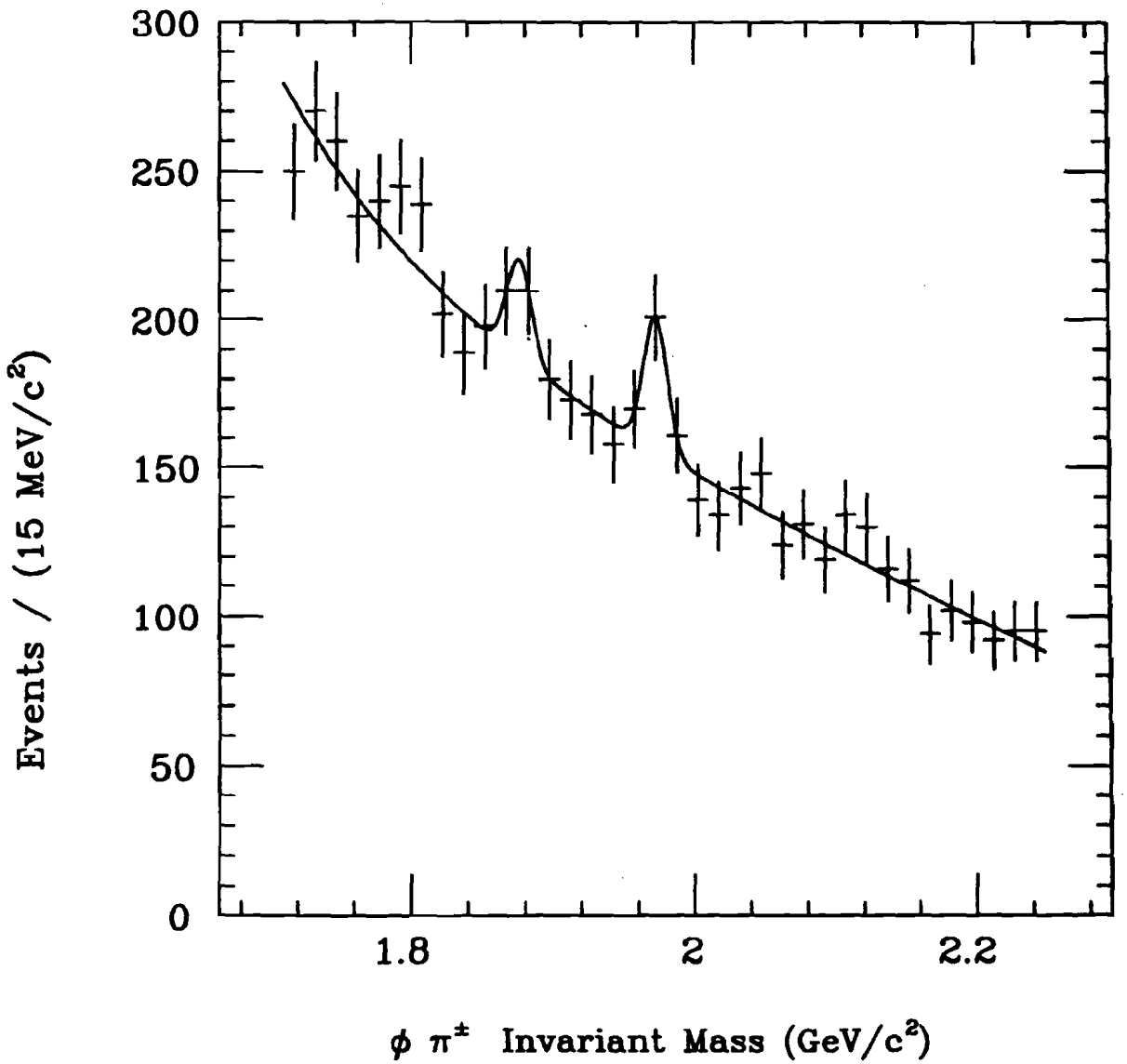

Figure 5.3 $\phi\pi^{\pm}$ invariant mass subject to analysis cuts including angular distribution.

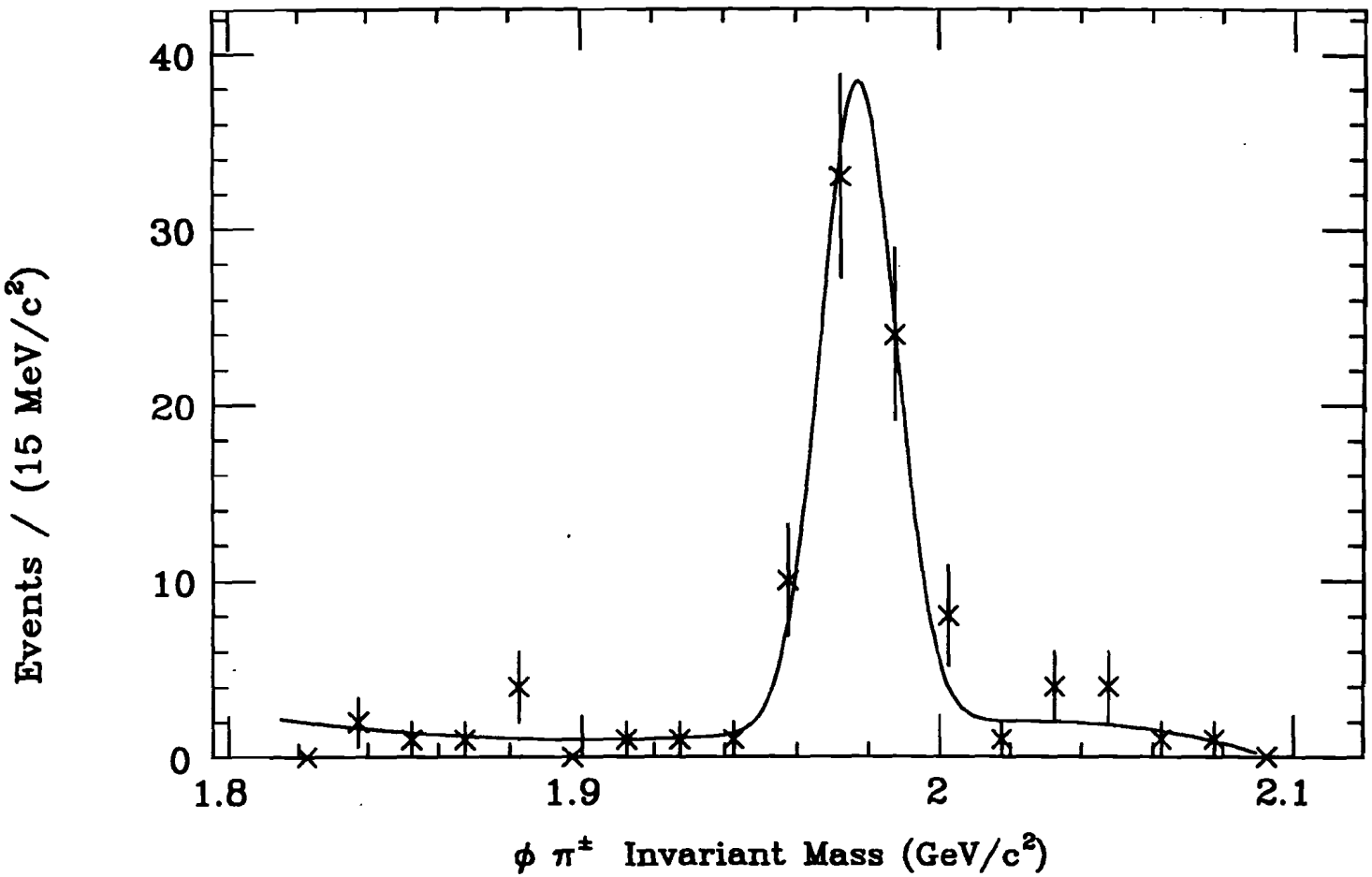

Figure 5.4 Monte Carlo $D_s^{\pm}$ invariant mass plot.

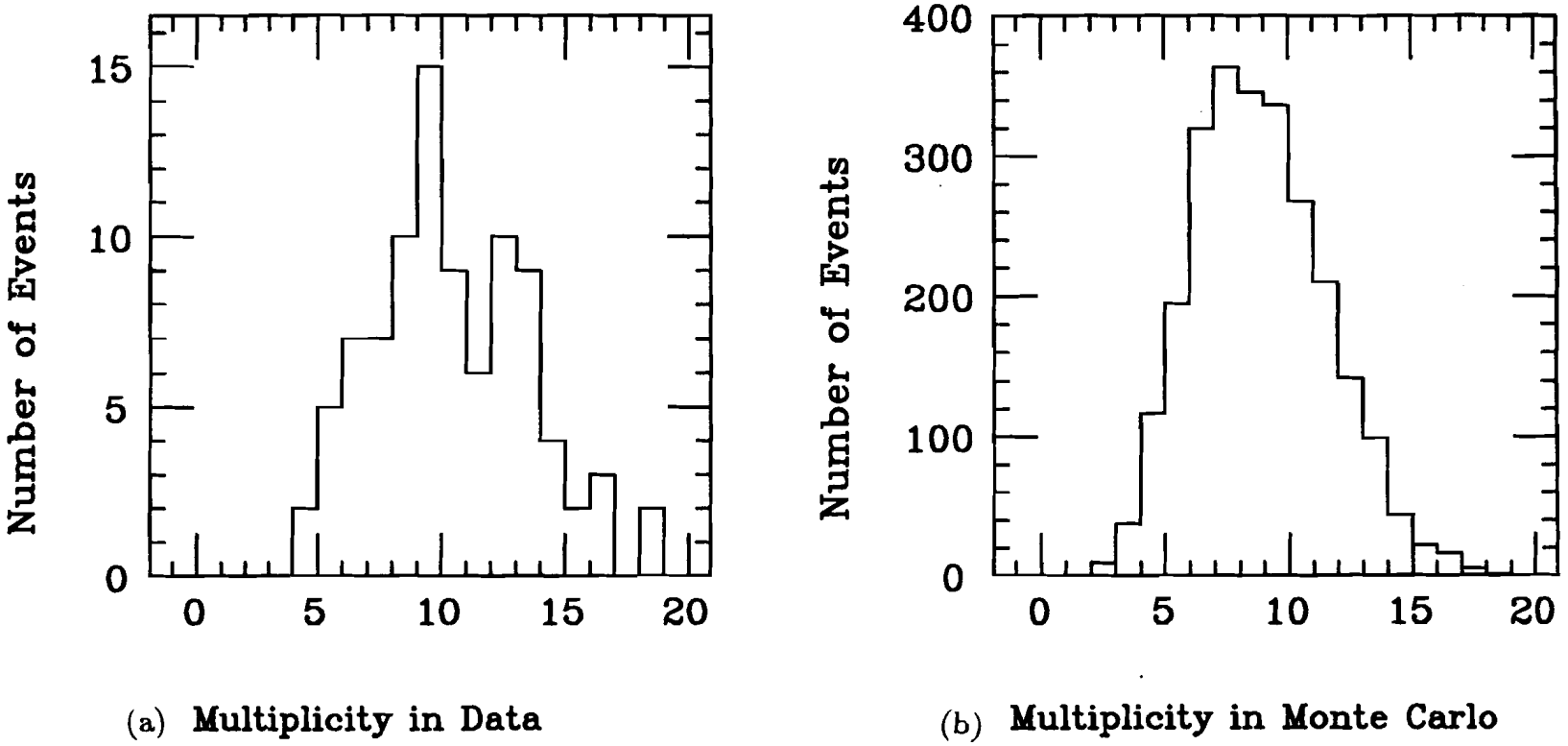

(a) **Multiplicity in Data**

(b) **Multiplicity in Monte Carlo**

Figure 5.5 Multiplicity distributions.

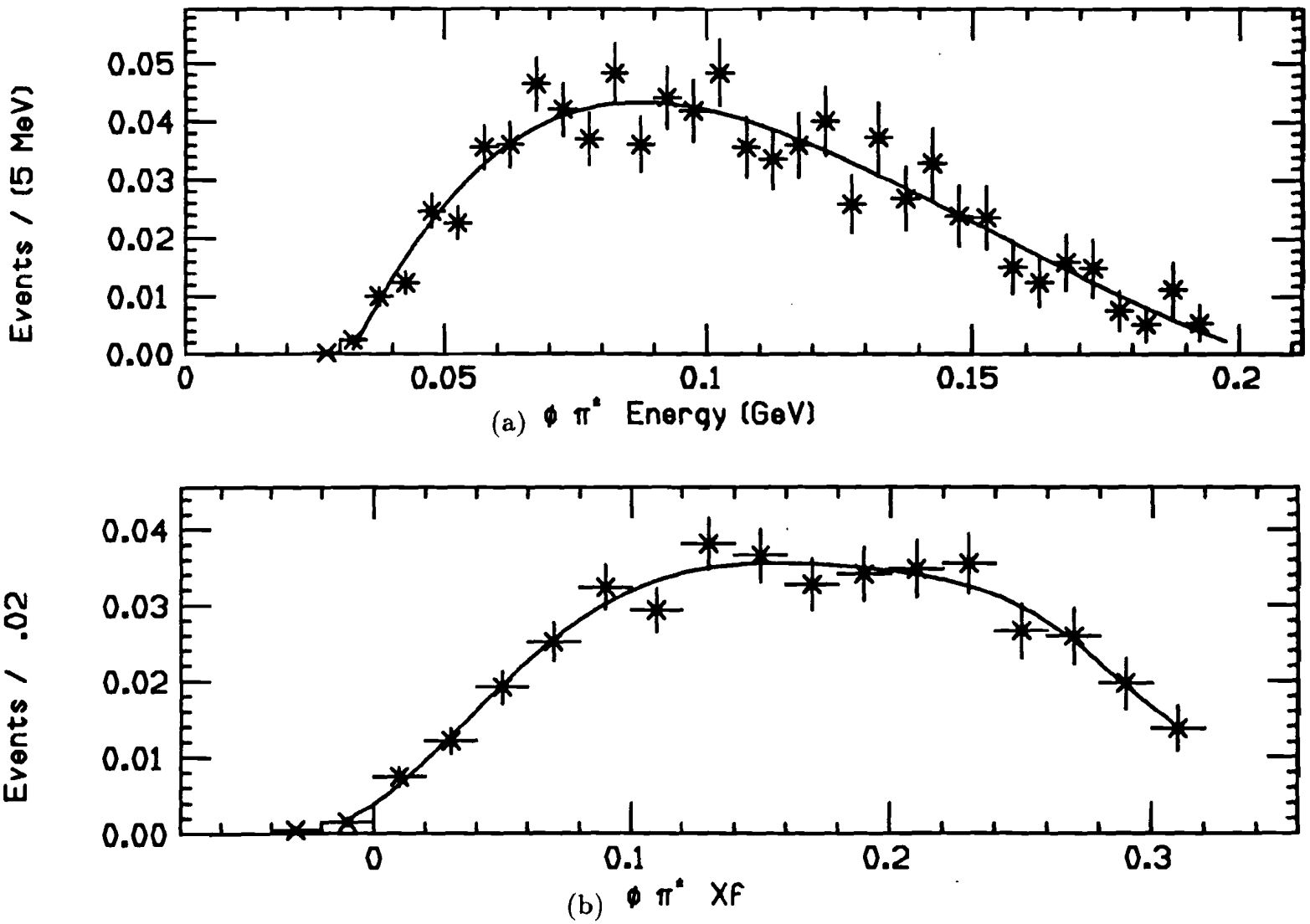

Figure 5.6 $D_s^{\pm}$ acceptance curves generated by Monte Carlo.

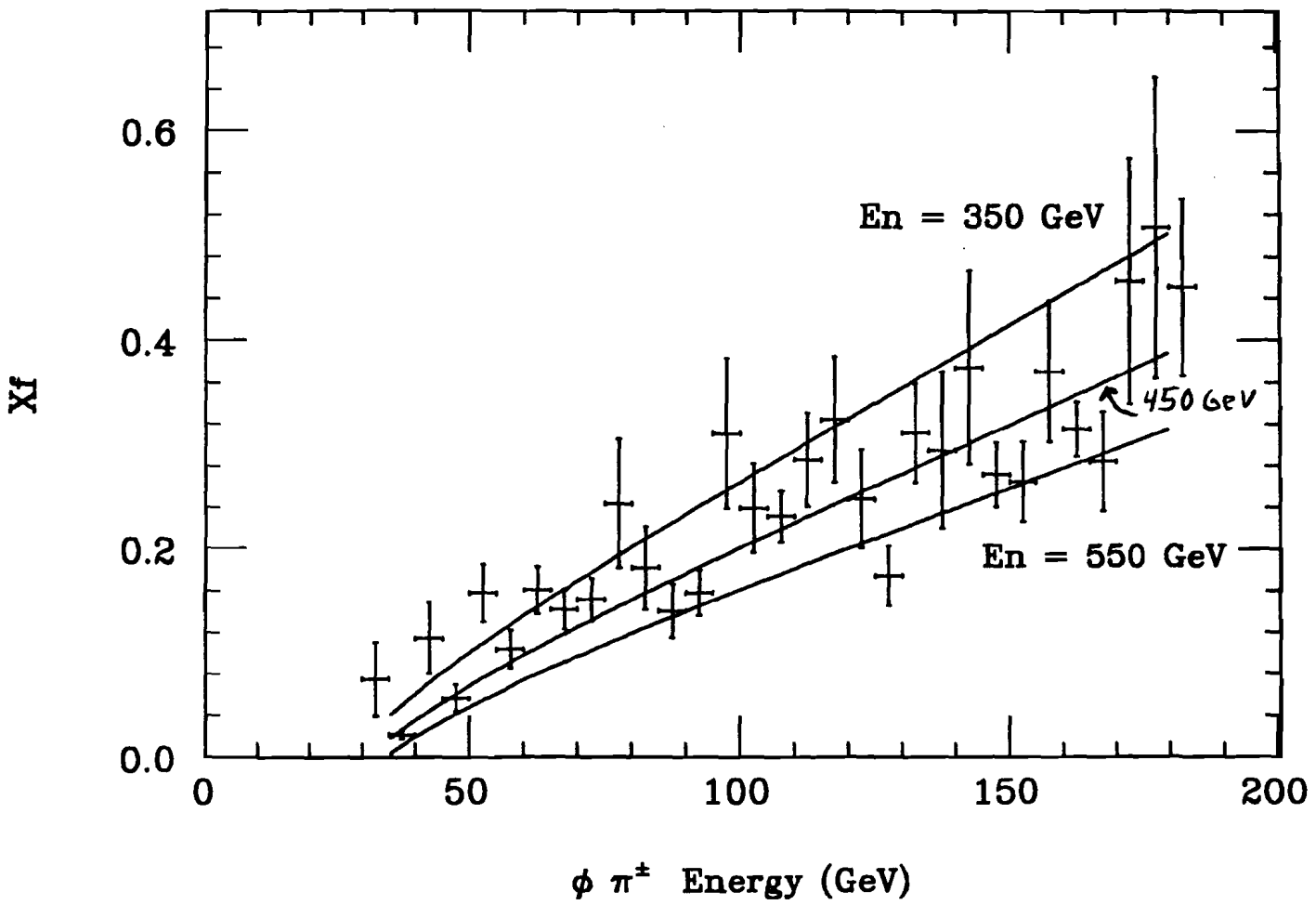

Figure 5.7 Simulation of state energy vrs x_f.

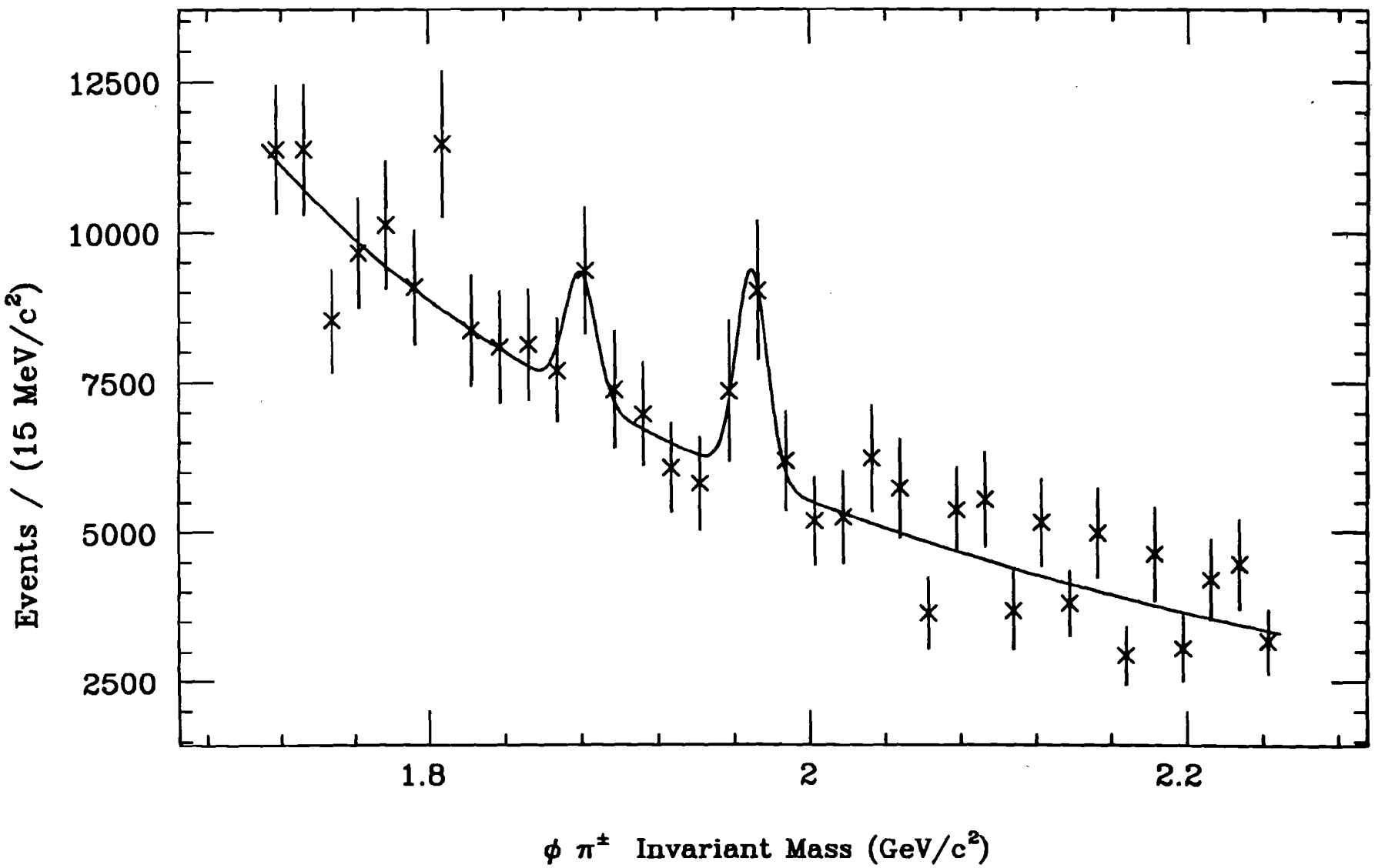

Figure 5.8 x_f weighted $\phi\pi^{\pm}$ invariant mass plot.

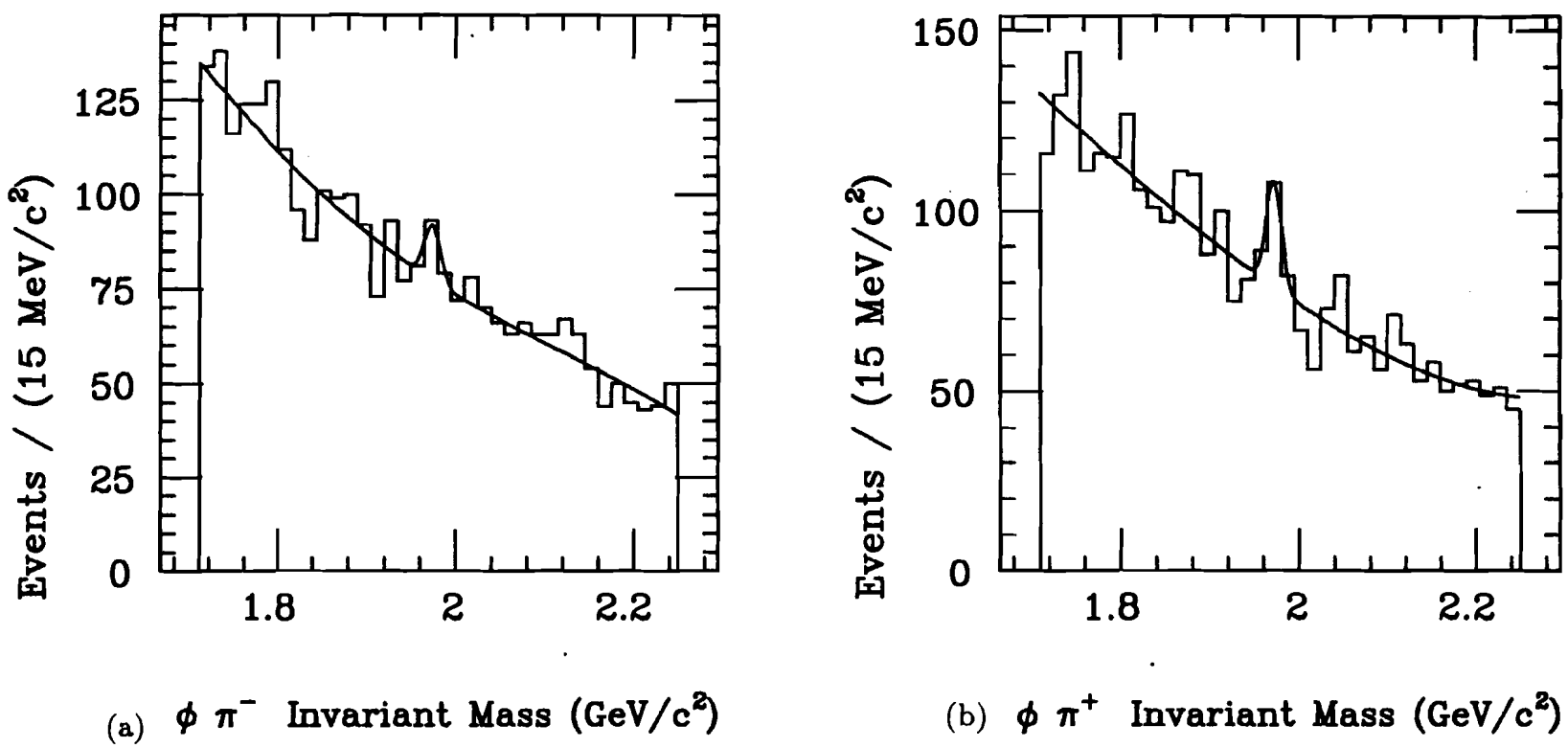

Figure 5.9 $\phi\pi^{\pm}$ invariant mass according to charge.

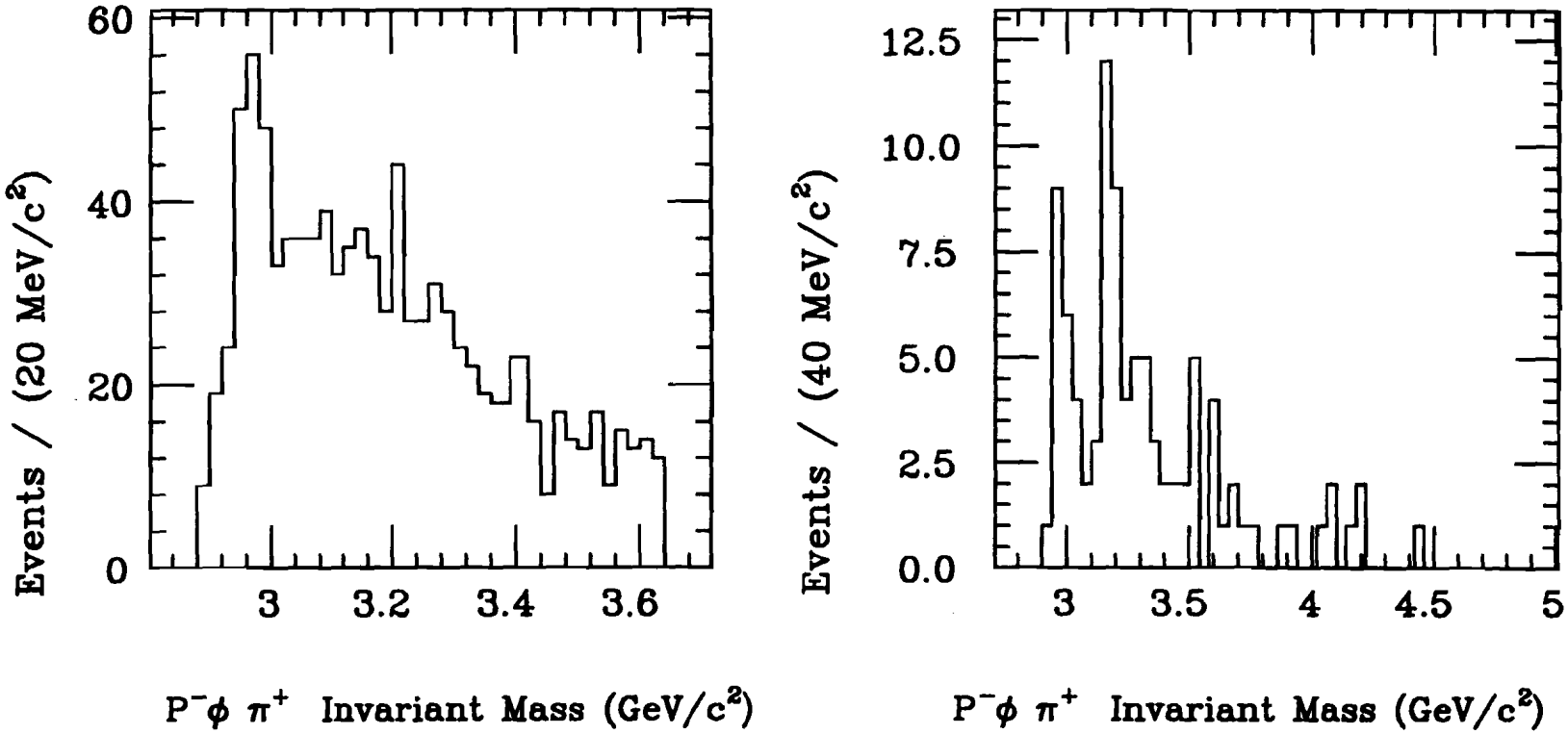

(a) Broad cuts.

(b) Tight analysis cuts.

Figure 5.10 $\bar{P}\phi\pi^+$ invariant mass

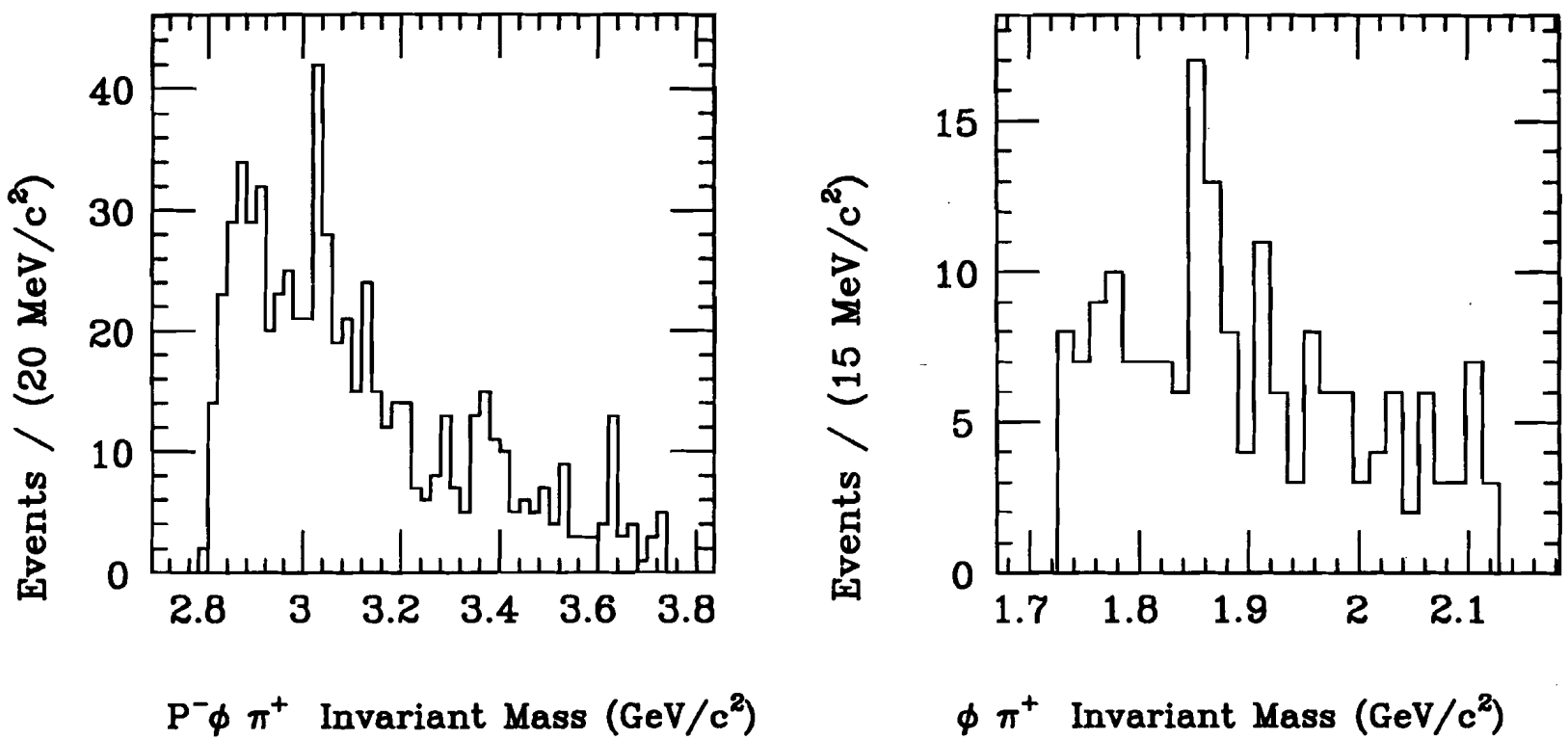

Figure 5.11 Using the D^+.

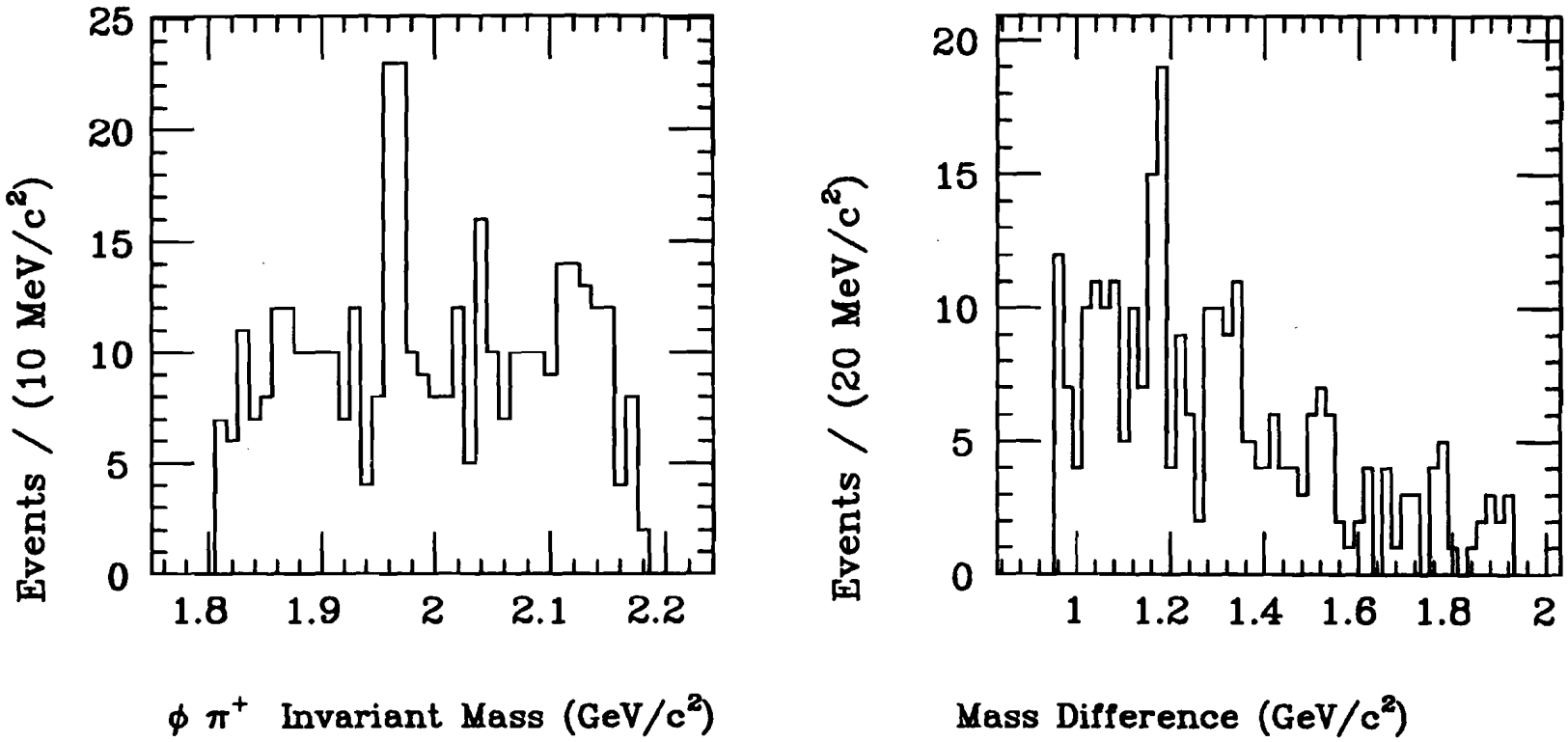

Figure 5.12 Using the mass difference.

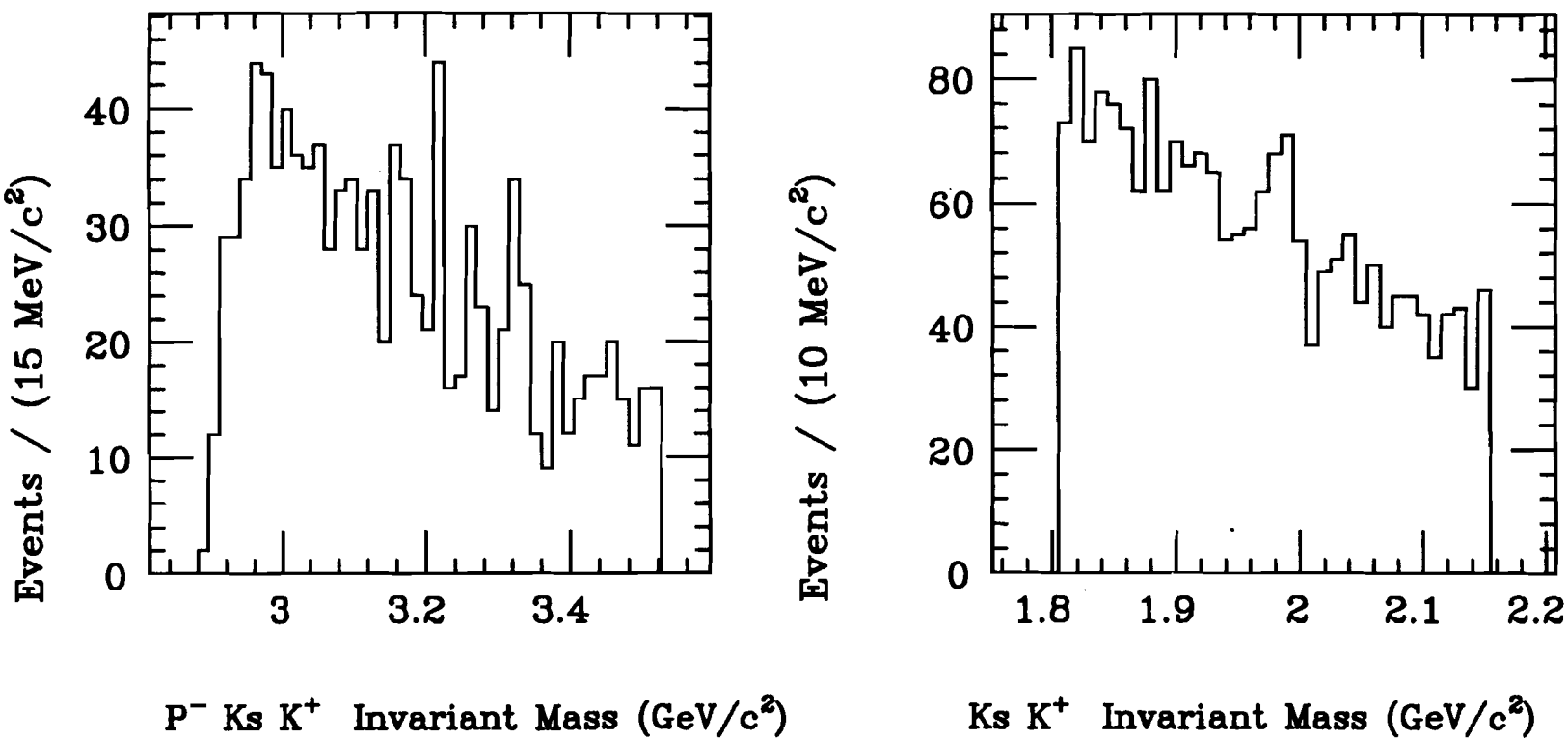

Figure 5.13 Alternate submass plots.

FERMILAB LIBRARY

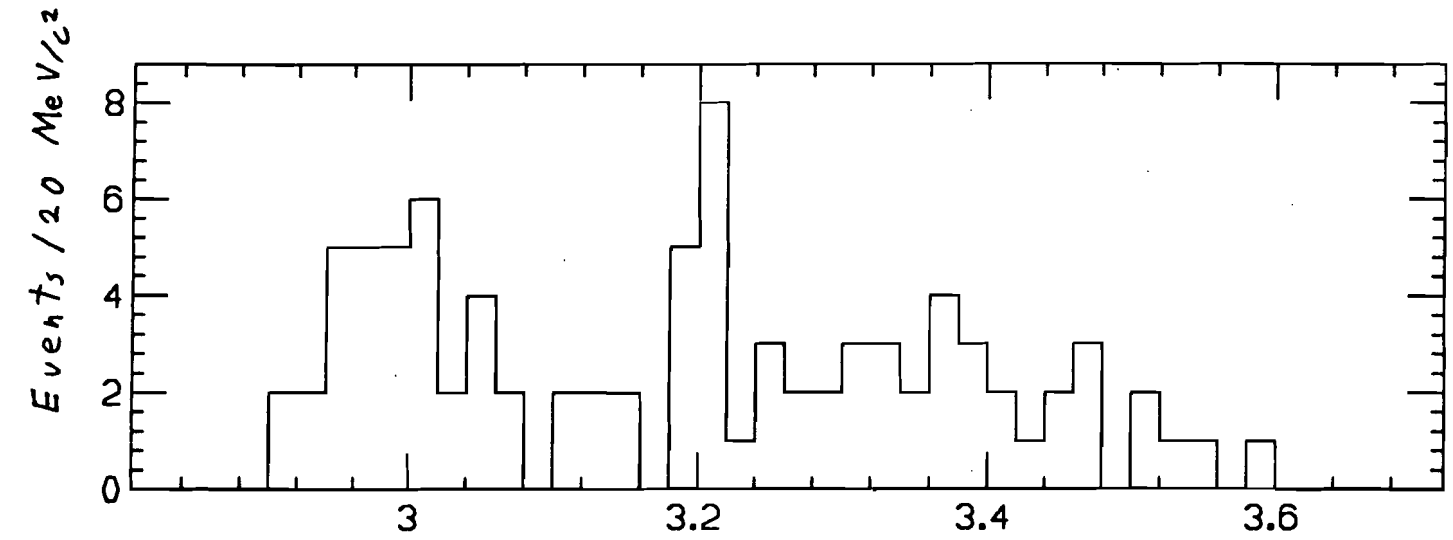

(a) $\bar{P}(K_s^0 K^+)$ GeV/c^2.

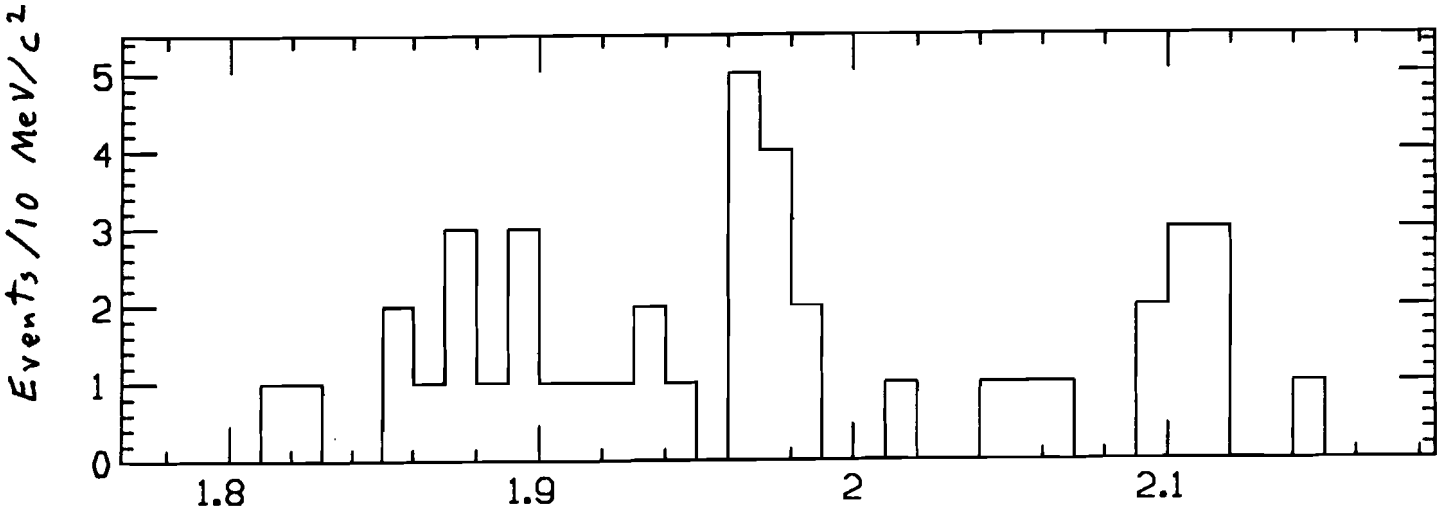

(b) $(K_s^0 K^+)$

Figure 5.14 $\bar{P}(K_s^0 K^+)$, tighter cuts.

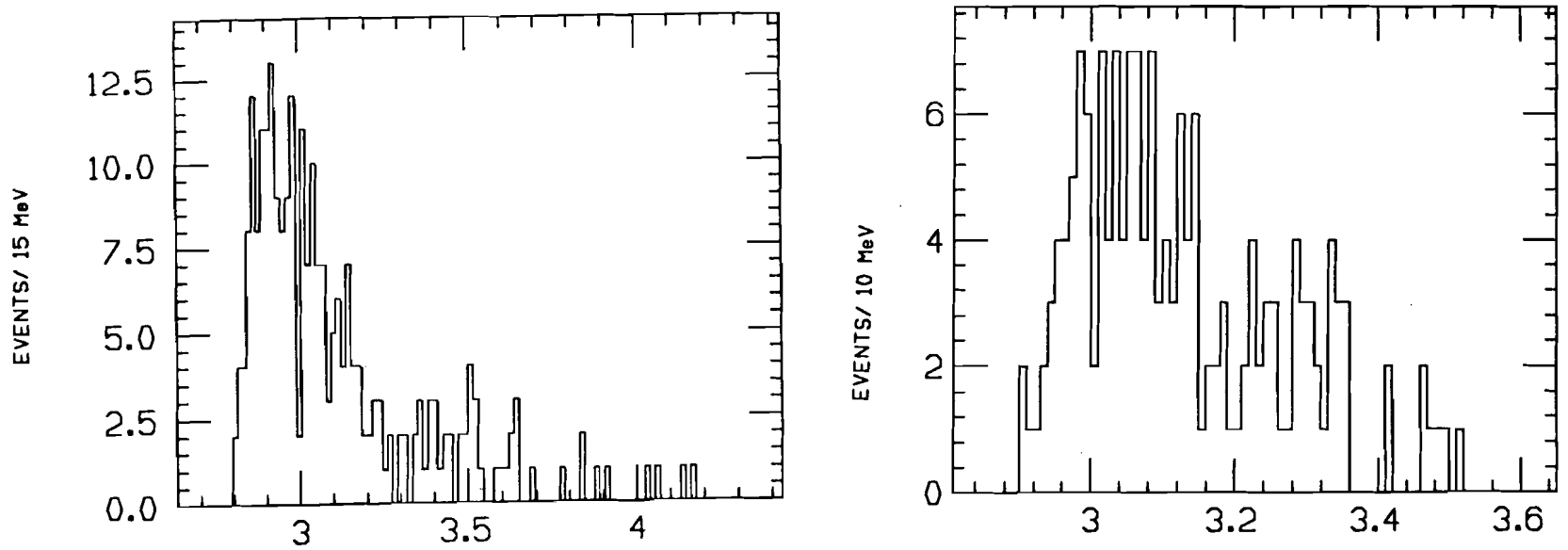

(a) (b)

Figure 5.15 Monte Carlo $\bar{P}\phi\pi^+$.

CHAPTER 6

Conclusions

I have observed strong evidence of the hadroproduction of several species of charm mesons – $D^{*\pm}$, D^0, and $D_s^{\pm}$. I have also observed evidence for the $D^{\pm}$. These observations were made during the 800 GeV run of E400 at FNAL.

A $D^{*\pm}$ signal was observed with a mean mass of $2.017 \pm .004$ GeV/c^2 with width 19 ± 5 MeV/c^2. This signal was observed with a significance in excess of six standard deviations (against being a statistical fluctuation) – the size of the sample was 129 ± 21 events. This $D^{*\pm}$sample was selected to decay by the mode $D^{*\pm} \rightarrow D^0, \pi^{\pm}$ with the subsequent Cabibbo-suppressed decay $D^0 \rightarrow K^+K^-$. The D^0signal was observed at a mean mass $1.872 \pm .005$ GeV/c^2 with a width 18 ± 3 MeV/c^2. The significance of the D^0signal was in in excess of seven standard deviations – the size of this sample was 134 ± 19 events. The $D^{*\pm} - D^0$ mass difference plot was observed to be at a mean mass of $145.1 \pm .5$ MeV/c^2 with a width of $1.1 \pm .5$ MeV/c^2.

The ratio of particle to antiparticle for the $D^{*\pm}$was found to be:

$$\frac{N(D^{*+} \rightarrow D^0\pi^+)}{N(D^{*-} \rightarrow D^0\pi^-)} = .83 \pm .25 \tag{1}$$

where the number of D^{*+} events was 57 ± 12 and the number of D^{*-} events was 69 ± 15. The D^{*+} signal was at a mean mass of $1.872 \pm .006$ GeV/c^2 with a width of 19 ± 5 MeV/c^2. The D^{*-} signal was at a mean mass of $1.873 \pm .006$ MeV/c^2 with a width of 18 ± 4 MeV/c^2.

The cross section per nucleon for $D^{*\pm}$, at most probable energy $\sqrt{s} = 35$ GeV, was measured to be:

$$\frac{d\sigma(\bar{X})}{dX} \cdot BR \;=\; 2.11 \;\pm\; .43\,(\pm .63)\mu\text{b/nucleon} \tag{2}$$

for $0.0 < x_f < 0.14$ ($\bar{X} = .07$). The first error is statistical and the second error is systematic. The branching ratio (BR) is defined as:

$$BR \equiv BR(D^* \rightarrow D\pi) \times BR(D \rightarrow K^+K^-) \tag{3}$$

The A dependence has been assumed to be of the form $A^{1.0}$. After correcting for the limited x_f range and inserting the branching fractions, the total cross section $\sigma(\mathrm{D}^{*+})$ is 337 ± 69 ± 101 microbarns.

The A dependence of the cross section was determined by fitting the $\mathrm{D}^{*\pm}$production for tungsten, silicon, and beryllium to a form A^α. The value of α was found to be $\alpha = .96 \pm .17$.

The $\mathrm{D}_s^\pm$signal had a significance of four standard deviations – the size of the sample was 64 ± 16 events. This statistical significance is derived by making the conservative estimate in which the ratio of the area to the error on the area is used. The signal is observed at a mean mass of 1.972 ± .005 GeV/c^2 with a width of 8.4 ± 3.5 MeV/c^2.

The decay in which the $\mathrm{D}_s^\pm$signal is observed is $\mathrm{D_s}^\pm \rightarrow \phi\pi^\pm$ in which the ϕ is observed in the decay mode $\phi \rightarrow K^+K^-$. The ϕ sample contains 33,000 events and has a mean mass of 1.0195 GeV/c^2 ± .00035 MeV/c^2 with a Gaussian distribution width of 1.73 ± .05 MeV/c^2 which was convoluted with a Breit-Wigner shape of fixed width 4.22 MeV/c^2.

The number of $\mathrm{D_s}^+$ events was found to be 42 ± 15. This signal was at a mean mass of 1.972 ± .005 GeV/c^2 with a width of 9 ± 4 MeV/c^2. The number of $\mathrm{D_s}^-$ events was found to be 22 ± 16. This signal was at a mean mass of 1.974 ± .007 GeV/c^2 with a width of 9 ± 5 MeV/c^2. The ratio of particle to antiparticle was:

$$\frac{N(\mathrm{D_s}^+ \rightarrow \phi\pi^+)}{N(\mathrm{D_s}^- \rightarrow \phi\pi^-)} = 1.9 \pm 1.5 \tag{4}$$

The differential cross section for $D_s^{\pm}$production averaged over the particle and antiparticle states is:

$$\mathrm{BR} \cdot \frac{1}{2}\left(\frac{d\sigma(D_s^+)}{dx_f} + \frac{d\sigma(D_s^-)}{dx_f}\right) = 2.85 \pm 0.80 \ \pm .86 \ \mu\mathrm{b/nucleon \ at} \ x_f = 0.175 \qquad (5)$$

where the first error is statistical and the second error is systematic. The branching fraction is defined to be:

$$BR \equiv BR(D_s \rightarrow \phi\pi) \qquad (6)$$

A linear A dependence was assumed. If a branching ratio of .036 is used the total cross section $\sigma(D_s^+)$ after correcting for the limited x_f range is 68 ± 19 ± 20 microbarns.

The ratio of $D_s^{\pm}$to $D^{*\pm}$cross section is found to be:

$$\frac{BR(D_s) \cdot \frac{d\sigma}{dx_f}(D_s)}{BR(D^*) \cdot \frac{d\sigma}{dx_f}(D^*)} = 2.18 \pm 1.08 \text{ at } x_f = 0 \qquad (7)$$

After correcting for the world average $D^{*\pm}$and $D_s^{\pm}$branching fractions:

$$\frac{\frac{d\sigma}{dx_f}(D_s)}{\frac{d\sigma}{dx_f}(D^*)} = 0.19 \pm 0.09 \text{ at } x_f = 0 \qquad (8)$$

Evidence was observed for a $D^{\pm}$signal of 47 ± 23 events. This signal had a mass of 1.876 ± .004 GeV/c^2 with a width of 8.4 ± 3.5 MeV/c^2. A comparison of the acceptance weighted number of $D^{\pm}$and $D_s^{\pm}$events yields:

$$N_{D^{\pm}}/(N_{D^{\pm}} \ + \ N_{D_s^{\pm}}) = .38 \pm .17 \qquad (9)$$

Another E400 researcher observed a signal for $D^0 \rightarrow K_s^0 K_s^0$ using the $D^{*\pm} - D^0$ mass difference. The production ratio of that state to the D^0decay mode I observe gives the result:

$$\frac{\Gamma(D^0 \rightarrow K^0 \bar{K}^0)}{\Gamma(D^0 \rightarrow K^+ K^-)} = .4 \pm .3 \qquad (10)$$

It is of importance in studies of hadroproduction to improve the significance of

the signals by reducing the naturally large backgrounds (compared to other production mechanisms; e.g., photoproduction). Particle identification is a powerful tool in hadronic production experiments for improving the ratio of signal to background in decay modes involving strange particles. In particular, I have used the power of the E400 Čerenkov identification to distinguish kaons from pions as a tool in observing a number of charm states. Other analysis cuts than Čerenkov identification are also necessary to enhance the signal-to-noise ratio to an acceptable level of statistical significance. In the case of the D^0, I did not see a statistically significant signal without application of the $D^{*\pm} - D^0$ mass difference cut. For the $D_s^{\pm}$signal, it was important to use an analysis cut based on the properties of the angular distribution of the decay products.

It is necessary to accumulate large statistical samples of charmed events in order to make meaningful measurements of charm hadroproduction. The previous measurements of the D by LEBC-MPS at FNAL at 800 GeV have been severely hampered by poor statistics, as has previous measurements of the hadronic production of the $D_s^{\pm}$(described in the introductory chapter). The LEBC measurements[8], which find a $D/\bar{D}$ cross section of $59 \pm 29 \pm 15$ μB, used a sample of topologically sorted bubble chamber vertices of several dozen events unspecified as to particular decay mode. Any previous hadronically produced $D_s^{\pm}$sample has had substantially less than 50 events.

E400 has aimed to improve the situation by accumulating a larger volume of relatively unbiased events. In the case of the $D^0 \rightarrow K^+K^-$ I have observed a large signal (134 ± 19 events). I have also observed the largest hadronically produced sample of $D_s^{\pm}$(64 ± 16 events).

The fraction of all D^0production which we observe to come from the $D^{*\pm}$signal can be explored with the ratios of the several charm species I have found. The ratio

of the number of D^+ to $D_s{}^+$ is found by combining a symmetric particle-antiparticle assumption from Eqn. (4) with the fraction of Eqn. 9 to be:

$$\frac{N_{D^+}}{N_{D_s^+}} = .61 \pm .44 \tag{11}$$

If I use a branching fraction of .01 for $D^+ \rightarrow \phi\pi^+$ and a branching fraction of .035 for $D_s{}^+ \rightarrow \phi\pi^+$ I can get the relative production ratio:

$$\frac{D^+}{D_s{}^+} = 2.14 \pm 1.54 \tag{12}$$

Using the result of Eqn. 8 I find:

$$\frac{D^+}{D^{*+}} = .41 \pm .35 \tag{13}$$

There is now enough information presented to consider the problem of determining what fraction of the D's come from $D^{*\pm}$and what fraction of D's are directly produced. For this purpose I define a fraction f in terms of directly produced charm particles:

$$f \equiv \frac{D^*}{(D^* + D)} \tag{14}$$

where the charm symbols in Eqn (14) represent direct production of the positive charge and neutral *particle*. I must invoke an assumption of "isotopic democracy" about the relative amounts of the charge states for the same charm meson species of particle (the same principle would apply for the antiparticle). That is, I assume there are $\frac{f}{2}D^{*+}$'s, $\frac{f}{2}D^{*0}$'s, $\frac{(1-f)}{2}D^{+}$'s, and $\frac{(1-f)}{2}D^{0}$'s directly produced. I use the branching fractions:

$$BR(D^{*+} \rightarrow D^0) = .49 \text{ and } BR(D^{*+} \rightarrow D^+) = .51 \tag{15}$$

to now find the contribution to D's from *both* direct production and D^* decays:

$$D^+ = \frac{(1-f)}{2} + \frac{f}{2} * .51 \tag{16}$$

and the D^{*+} of course has only direct production. The ratio of all production routes of these two charm particles is then:

$$\frac{D^+}{D^{*+}} = \frac{\frac{(1-f)}{2} + \frac{f}{2} * .51}{\frac{f}{2}} \tag{17}$$

which gives the result:

$$\frac{D^+}{D^{*+}} = \frac{1}{f} - .49 \tag{18}$$

which can be compared to Eqn. 13 to get the result:

$$f = 1.11 \pm .43 \tag{19}$$

which would imply that nearly all of the D's are produced by D^* decay. The branching fraction of the $D_s^{\pm}$is not well known, so the errors on the branching fractions are not included. That is certainly a significant source of error for the measurement. In conclusion to this part of the discussion, the relative production rates of the $D_s^{\pm}$and $D^{*\pm}$appear to be consistent although not well determined because of the large error bars resulting from the weakness of the D^+ signal.

I now wish to compare the above finding with results from an experiment using another type of beam. The thesis of Peter Kim on ARGUS, an e^+e^- annihilation experiment, gives cross sections $\sigma(D^0) = 1.48 \pm .28\, nb$, $\sigma(D^+) = .48 \pm .10\, nb$, and $\sigma(D^{*+} = .73 \pm .18\, nb$. For the model of isotopic democracy given above, it would be expected that $\sigma(D^0)$ was equal to the sum of the other two cross sections given. The observation is consistent with that expectation. As a more detailed check, we have performed a χ^2 minimization with respect to two independent parameters which describe the situation – the fraction f, and the sum of charm production for the three particles. It was found that $f = .89 \pm .145$ with a χ^2 at the minimum (for the one degree of freedom) of .61. The goodness of the fit of the isotropic democracy model to the ARGUS numbers gives confidence in the assumption of isotopic democracy. The value found for f is consistent with ours, and allows room for direct D production.

Reference 32 has compared the results of NA11 and NA27 to get an A dependence in which $\alpha = 1$ at $x_f = 0$, and $\alpha \approx .8$ for high x_f, and claims "excellent agreement" with the results of E613, WA78 and BIS-2. The A dependence I find is similar to results found[33] for the J/ψ using 300 GeV neutrons on beryllium, which claim $\alpha = .93 \pm .04$ independent of x_f. The x_f range I used was near 0.

Open-charm experiments using such multinucleon targets such as beryllium (or in our case beryllium, tungsten, and silicon) have been compared with charm experiments performed in a bubble chamber or at storage rings in which the target is hydrogen. This comparison has been done assuming that the cross section per nucleon scales by some power of the number of nucleons in the target nucleus. Cross section studies of strangeness production[34] have indicated that although a simple scaling works well among various multinucleon targets, there is disparity by a factor of approximately two when extrapolating the results of such a measurement to the unique case of a hydrogen target. This might also be true for charm. The situation could be resolved by a future experiment in which the target region can contain either hydrogen or heavier elements, and have the same beam and the same experimental detectors as scientific controls.

In summary, I measure the A-dependence of open-charm hadroproduction to be consistent with a hard parton collision model, and observe large cross sections for charm meson production in several decay modes at levels which are consistent with what could be expected to be the relative production rates. Other E400 researchers[30,35] have measured large cross sections for charmed baryon hadroproduction. The cross section for ϕ production has been measured by E400 to be consistent with the measurement by ACCMOR[36], so although our measurements have a large systematic bias, we are confident that neither our Monte Carlo corrections or our luminosity estimates are

introducing an order of magnitude into the systematic bias – the E400 measurements are consistent with hadronically produced charm cross sections of several hundred microbarns, rather than several tens of microbarns as suggested by LEBC. The charm production model by Ellis and Quigg that we use in the E400 Monte Carlo predicts a charm cross section $\frac{d\sigma}{dx_f}$ of about twenty microbarns at $x_f = 0$ for $M_c = 1.5$ GeV/c^2 and $\sqrt{s} = 38.8$ GeV. This is an order of magnitude below what I observe. Results from the ISR[9] suggest that the cross section is an order of magnitude larger than what QCD theoretical calculations can accommodate. The cross section for hadroproduction of charm is certainly controversial, and in the next several years results from the introduction of microstrip detectors to experiments at existing accelerators may produce the clean, high-statistics signals from several independent experiments needed to verify the hadroproduction characteristics of open-charm. If the results of this thesis are confirmed by future experiments, then QCD based theories will require extensive modifications.

APPENDIX A

Calculation of the Čerenkov Light Function

This appendix describes the method used in E400 to compute the light yield in rectangular light collection cells. For the purposes of this appendix assume that the track (or center of the Čerenkov cone) lies at the origin of a coordinate system and we wish to compute the fraction of Čerenkov light which strikes a rectangle extending from X_1 to X_2 and from Y_1 to Y_2 on some optical plane which is roughly normal to the track image.

The model which considers all tracks to be normally incident was found by Monte Carlo simulation to be appropriate. The effect of incident tracks striking the mirror planes at typical angles on the order of 10 milliradians with respect to the normal was negligible. In principle, this effect results in a non-circular elliptical light pattern; however, in practice the resulting light density in the outer regions of the ellipse and ellipse eccentricity are unimportant distortions to the circular model of the light pattern.

There are four subjects that will be covered. First, I will show how the light fraction within an arbitrary rectangle can by computed from a "corner" function of the coordinates at each of the 4 corners. Then this corner function will be derived. Next, I will describe a method for storing the corner function into a prestored table and performing a two dimensional linear interpolation to rapidly compute light fractions. Finally, I will discuss the modification of these techniques to cover rectangular holes in mirrors , and the effects of plane mirrors inclined at 45 degrees. This last point is important for the Čerenkov counter which was constructed by Illinois.

A.1 Corner Functions

Denote the normalized light density as $\rho(x,y)$. Because the center of the light cone is located at the origin , the density has the symmetry: $\rho(\pm x, \pm y) = \rho(x,y)$ Assume that the coordinates are ordered such that: $X_2 \geq X_1$, $Y_2 \geq Y_1$. The fraction of light within a rectangle is then:

$$F = \int_{X_1}^{X_2} dx \int_{Y_1}^{Y_2} dy\ \rho(x,y)$$

These integrals can be referenced to the origin via:

$$f = \left(\int_0^{X_2} dx - \int_0^{X_1} dx \right) \left(\int_0^{Y_2} dy - \int_0^{Y_1} dy \right) \rho(x,y)$$

Defining the corner function $I(X,Y)$ as follows:

$$I(X,Y) \equiv \int_0^X dx \int_0^Y dy\ \rho(x,y)$$

one can write the fraction as:

$$F = I(X_2,Y_2) + I(X_1,Y_1) - I(X_1,Y_2) - I(X_2,Y_1)$$

Because of the reflection symmetries of the light density, the corner function for any quadrant can be obtained from the positive X and Y quadrant. As an example consider I (X , Y) with $X < 0$:

$$I(X,Y) = \int_0^{-|X|} dx \int_0^Y dy\ \rho(x,y)$$

one can change variable ($x \rightarrow -x$) to obtain:

$$I(X,Y) = -\int_0^{|X|} dx \int_0^Y dy\ \rho(-x,y) = -I(|X|,Y)$$

In general then:

$$I(X,Y) = S_X\ S_Y\ I(|X|,|Y|)$$

where S_X and S_Y are the sign of X and Y (That is $S_X, S_Y = \pm 1$ depending on the sign of X and Y). Using these formulae one can compute the light yield for an arbitrary rectangle as a sum over corner functions:

$$F = \sum_{m=1}^{2}\sum_{n=1}^{2}(-1)^{m+n}\ S_{X_m}S_{Y_n}\ I(|X_m|,|Y_n|)$$

A.2 Derivation of the Corner Function

To find the light sharing function I($|X|$,$|Y|$) one can work with a light cone of unit radius by defining x=$\frac{|X|}{R}$ and y=$\frac{|Y|}{R}$. I(x,y) is defined to be the amount of light left of and below the corner located at (x,y) as seen in Figure A.1. It is calculated by integrating the normalized light density

$$dI = \frac{d\phi dr}{2\pi}$$

over that area and has a maximum value of $\frac{1}{4}$. There are four distinct cases to be considered when finding I(x,y). These are based on the location of the corner with respect to the cone and are illustrated in Figures A.1(a) through A.1(d). The code was written to calculate the light sharing function (referred to as **FB**) for the appropriate case. I will now derive the formulae used.

The value of I(x,y) in all the cases are found by integrating over two basic shapes. The first of these is marked A_x in Figure A.1(a) and is found to be

$$\begin{aligned} A_x &= \frac{1}{2\pi}\int_0^{\theta} d\phi \int_0^{\frac{x}{\cos\phi}} dr = \frac{x}{2\pi}\int_0^{\theta}\frac{d\phi}{\cos\phi} \\ &= \frac{x}{2\pi}\ln(\sec\theta + \sqrt{\sec^2\theta - 1}) \end{aligned}$$

The second is the arc equal to the sum of A_x and δ_x. Its light fraction is then

$$A_x + \delta_x = \frac{1}{2\pi}\int_0^{\arccos x} d\phi \int_0^1 dr$$

so that

$$\delta_x = \frac{1}{2\pi}\arccos x - A_x$$

For the case where y>1 and x<1, shown in Figure A.1(a), the light sharing fraction is $FB = \frac{1}{4} - \delta_x$ and $\sec\theta = \frac{1}{x}$. Solving for δ_x and substituting:

$$\begin{aligned} FB &= \frac{1}{4} - \frac{1}{2\pi}[\arccos x - x\ln(\sec\theta + \sqrt{\sec^2\theta - 1})] \\ &= \frac{1}{2\pi}\left[\arcsin x + x\ln\left(\frac{1}{x} + \sqrt{\frac{1}{x^2} - 1}\right)\right] \end{aligned}$$

The case where x>1 and y<1, shown in Figure A.1(b), is found, by symmetry, to be

$$\begin{aligned} FB &= \frac{1}{4} - \delta_y \\ &= \frac{1}{2\pi}\left[\arcsin y + y\ln\left(\frac{1}{y} + \sqrt{\frac{1}{y^2} - 1}\right)\right] \end{aligned}$$

When x,y<1 and $x^2 + y^2$ >1, the situation shown in Figure A.1(c) exists such that $FB = \frac{1}{4} - \delta_x - \delta_y$. This gives

$$FB = \frac{1}{4} + \frac{1}{2\pi}\left[x\ln\left(\frac{1}{x} + \sqrt{\frac{1}{x^2} - 1}\right) + y\ln\left(\frac{1}{y} + \sqrt{\frac{1}{y^2} - 1}\right) - \arccos x - \arccos y\right]$$

The final case, shown in Figure A.1(d), exists when $x^2 + y^2$ <1. The overall fraction is just the sum of the two sections so that

$$FB = \frac{1}{2\pi}[x\ln(\sec\alpha + \sqrt{\sec^2\alpha - 1}) + y\ln(\sec\beta + \sqrt{\sec^2\beta - 1})$$

Substituting $\tan\alpha = \frac{y}{x}$ and $\tan\beta = \frac{x}{y}$

$$FB = \frac{1}{2\pi}\left[x\ln\left(\sqrt{1 + \frac{y^2}{x^2}} + \frac{y}{x}\right) + y\ln\left(\sqrt{1 + \frac{x^2}{y^2}} + \frac{x}{y}\right)\right]$$

A.3 Two Dimensional Linear Interpolation of the Corner Function

In order to save time in evaluation of the corner functions a linear interpolation routine was written which used values of the corner function evaluated on a two dimensional lattice, as shown in Figure A.1(e). The coordinates of the corner function were normalized to the Čerenkov radius as described above so that I (X , Y) was stored in 0.1 steps with $0 \leq X \leq 1$ and $0 \leq Y \leq 1$.

The interpolation was performed by finding the lattice cell appropriate to a given (X,Y) argument. The form of the interpolation was assumed to be linear in x , and y which are **coordinates relative to the lattice cell center**:

$$I(X,Y) = \alpha + \beta x + \gamma y$$

where α , β , γ are essentially fits to the function evaluated at four corners of the lattice cell. The fit is to the form:

$$I\pm\pm \;=\; \alpha \pm \beta\,\Delta \pm \gamma\,\Delta$$

where the lattice spacing is 2Δ by 2Δ. This fit has one degree of freedom since their are four function evaluations and three linear parameters. The fit parameters are obtained by minimizing the χ^2 given by:

$$\chi^2 = (\alpha - \beta\Delta - \gamma\Delta - I_{--})^2 + (\alpha + \beta\Delta - \gamma\Delta - I_{+-})^2 + \cdots$$

The results of this fit are:

$$\alpha = \frac{I_{++} + I_{+-} + I_{-+} + I_{--}}{4} \quad \beta = \frac{I_{++} + I_{+-} - I_{-+} - I_{--}}{4\Delta}$$

$$\gamma = \frac{I_{++} + I_{-+} - I_{+-} - I_{--}}{4\Delta}$$

The values of α , β , γ were stored for each lattice cell as a look-up map in order to further accelerate the interpolation procedure.

In addition to the two dimensional interpolation procedure , one dimensional interpolation data was stored for cases where $|X| > 1$ or $|Y| > 1$ and thus $I(X,Y)$ became a function of X or Y only.

A.4 Modifications

The light sharing algorithm was used with several simple modifications to cover the cases of rectangular holes in the light collection cells (to allow uninteracted beam to pass through) and for the case of light collection via thin mirrors inclined at 45 degrees with respect to the beam axis. In both cases one computes the collected light fraction by subtracting an appropriate uncollected fraction of light from that fraction collected in the absence of such effects.

The rectangular hole requires just a simple check on the X-Y intersection in the central mirror region, but the use of 45° mirrors (as in the C0 counter) creates two effects. The first effect is that the active radiator length and hence photoelectron yield depends on the the location (typically $|X|$) of the track intersection with the mirror. The second effect is that the projected light pattern at the mirror plane is a donut rather than a space filling disk. The outer radius of the donut is proportional to the total optical path from the the upstream window to the location of the mirror plane. The inner radius is proportional to the amount of this path which does not form active radiator. This inactive optical path is equal to the distance (for a 45° mirror such as C0) the track travels after it strikes the mirror until it passes through the end of the counter. This effect can be handled by computing the light yield assuming an effective

radiator equal to the total optical path and then subtracting out the light from the inactive optical path. In other words, compute the light from the complete donut and subtract out the light in the donut hole. In most designs the total light in the donut will be independent of the track-mirror intersection, while the light in the donut hole will maximize at the median plane of the counter.

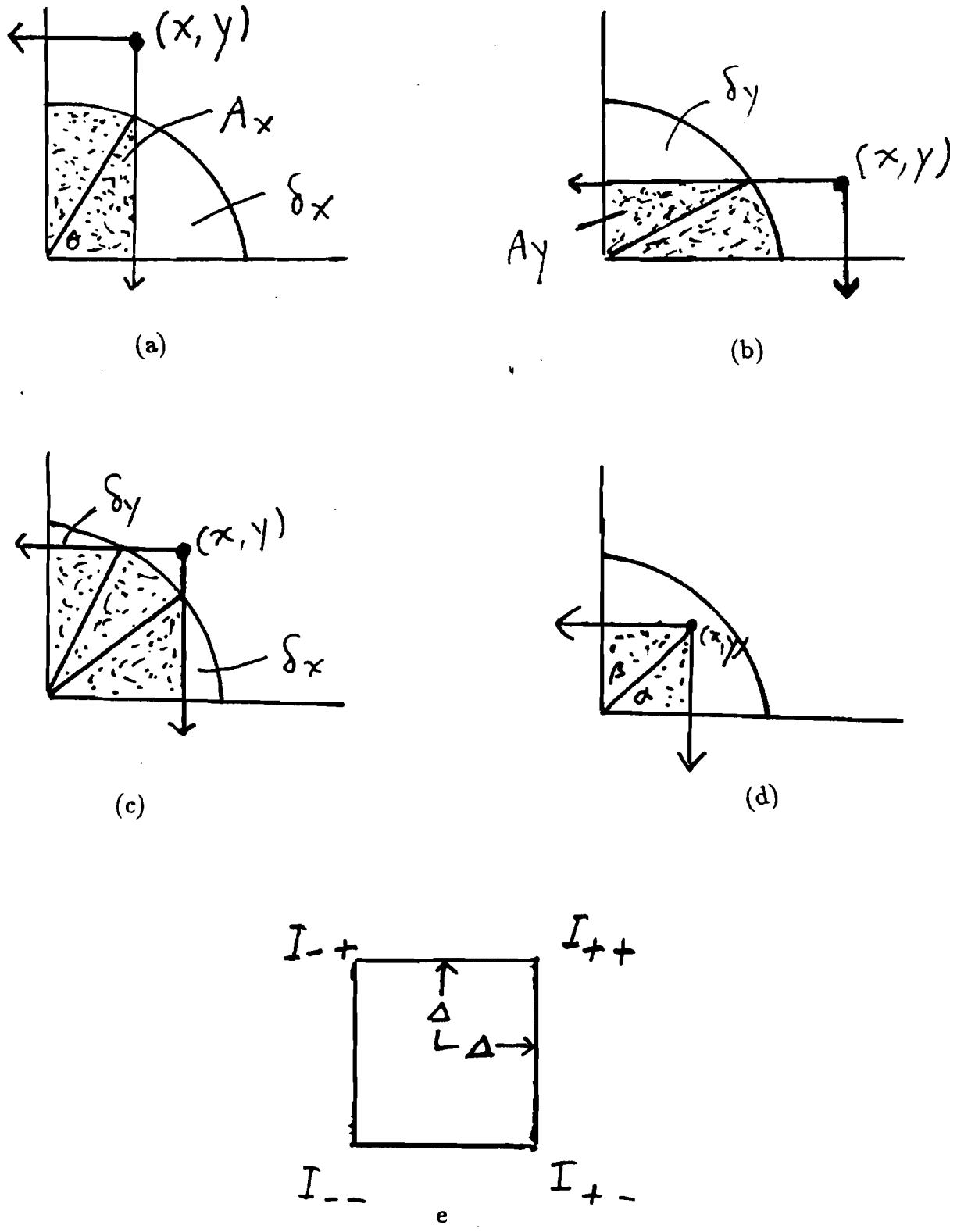

Figure A.1 Symmetry quadrant.

APPENDIX B

Calculation of the E400 Cross Section

The E400 cross section measurement σ_{STATE} for the production of a given charmed particle is derived from a comparison with the known total inelastic hadronic cross section by the relation

$$\sigma_{STATE} = \sigma_{TOTAL} * \frac{Y_{STATE}}{N_{TOTAL}} \tag{1}$$

where N_{TOTAL} is the value of the total integrated luminosity for the data sample and Y_{STATE} the acceptance weighted event yield for the particular state being measured. The total integrated luminosity is in practice a measurement of the number of neutrons which strike the target, and has a value of several hundred million for the E400 800 GeV data run (depending on the particular triggers covered). This is derived from counting the number of master gates which are fired during the run sample and adjusting for the interaction length of the target (two percent). The Master Gate efficiency ϵ_{MG} must also be included. The unweighted event yield is typically on the order of hundreds, and a careful explanation of the acceptances is required.

First I must comment on σ_{TOTAL}. What E400 uses in practice is $\sigma_{EFFECTIVE}$, which is a result of correcting for the use of several nuclear targets. In the absence of acceptance effects , the yield of inelastic neutron events for the i'th target segment $(Y_i^{(in)})$ is:

$$Y_i^{in} = N_n \; t_i \; \sigma_i^{(in)} \; \eta_i \tag{2}$$

where N_n is the number of incident neutrons , t_i is the thickness of the i'th target segment , σ_i is the measured inelastic neutron cross section for the i'th target

segment, and η_i is density of scatterers or nuclei per cm^3 for the i'th target segment. The density of scatters is given by the expression:

$$\eta_i = N_{av}\ \rho_i / A_i \tag{3}$$

where ρ_i is the mass density of target segment, A_i is the atomic weight, and N_{av} is Avogadro's number. Combining Eqn. (2) and (3) gives for the total inelastic yield:

$$Y^{(in)} = N_n\ N_{av} \sum_i \frac{\sigma_i^{(in)}\ \rho_i\ t_i}{A_i} \tag{4}$$

A very similar expression would hold for the yield of charmed particles if one replaced:

$$\sigma_i^{(in)} \rightarrow \sigma^{(chm)}\ A_i^{\alpha} \tag{5}$$

where $\sigma^{(chm)}$ is the charmed cross section per nucleus with the assumption used by E400 that it scales as A^{α}. Hence:

$$Y^{(chm)} = N_n\ N_{av}\ \sigma^{(chm)} \sum_i \rho_i\ t_i\ A_i^{(\alpha-1)} \tag{6}$$

Taking the ratio of the charm to unbiased inelastic yields:

$$\frac{Y^{(chm)}}{Y^{(in)}} = \sigma^{(chm)}\ \frac{\sum_i \rho_i\ t_i\ A_i^{(\alpha-1)}}{\sum_i \sigma_i^{(in)}\ \rho_i\ t_i / A_i} \tag{7}$$

Rearranging Eqn. (7):

$$\sigma^{(chm)} = \sigma_{eff}\ \frac{Y^{(chm)}}{Y^{(in)}} \tag{8}$$

where σ_{eff} is given by the expression:

$$\sigma_{eff} = \frac{\sum_i \sigma_i^{(in)}\ \rho_i\ t_i / A_i}{\sum_i \rho_i\ t_i\ A_i^{(\alpha-1)}} \tag{9}$$

This "effective " cross section would equal the total inelastic cross section per nucleon at high A (roughly 40 mb for elements beyond hydrogen) if charm had the same A - dependence as the total inelastic cross section namely $\alpha \approx .71$. However, as shown

in Figure 1, there is considerable variation in σ_{eff} as a function of α given the target configuration of E400.

I now will explain the efficiencies which are introduced by factors other than the choice of charm state in particular. The Master Gate efficiency, being a measure of the efficiency for secondaries firing certain counters, is dependent on the fraction of the neutron inelastic cross section into a given charge multiplicity, the momentum spectrum charged secondaries, and the efficiency of the T counter individual scintillation counters H×V hodoscopes. The fraction of the hadronic inelastic cross section falling into various multiplicity categories has been summarized by the LEBC-MPS collaboration[31] and has a value which sums to $\sigma_{TOTAL} = 33.6$ mB for all multiplicities. It must be noted that minor differences on the order of 10 % could result due to the fact that E400 had nucleon-nucleus interactions rather than the p-p interactions of the LEBC collaboration. To this level of certainty, the value of ϵ_{MG} can be estimated from the LEBC multiplicity breakdown of the cross section in terms of the independent probability P of a given charged track in the event making it through M2 and thus firing the H×V array:

$$\epsilon_{MG} = \frac{\Sigma(1-(1-P)^N - NP(1-P)^{(N-1)})\sigma(N)}{\Sigma\sigma(N)} \tag{10}$$

Assuming secondaries have a uniform spread in rapidity and that nine GeV/c is required of the average track to make it to the $H \times V$ array, P is calculated to be about .41. This leads to a value of $\epsilon_{MG} = 0.85 \pm 0.15$. This estimate is in excellent agreement with a MC simulation in which tracks were actually traced to see if they fired the $H \times V$ array. The counter efficiencies were known to be in excess of 90 % and were treated as being 100 % efficient in that calculation. Inefficiencies in these counters introduce a bias only to the minor degree that interactions containing charm have different multiplicities than general neutron interactions.

The use of Eqn. 6 to compute charm cross sections has several experimental complications. Since charmed particles are only produced when the apparatus is live, the inelastic yield must also be deadtime corrected. The livetime factor ϵ_{LIVE} is in the vicinity of .45 and the scalar readings of the inelastic events must be corrected by this factor. In addition the neutron beam has a halo, and the charmed particles originate from a targeted interaction. An analysis of unbiased events indicates the Si33 bussline had an overall average efficiency of $\epsilon_{Si33} = .654$ for Pin 2 events with multiplicity in excess of three. This factor also must be applied to the raw scalar reading in order to get the targeted luminosity. Finally, there is the assumption that because of the energy trigger we are only sensitive to the production of charmed particles above 300 GeV incident neutron energy. Therefore we adjust the yield of inelastic events by the factor $\epsilon_{SPECTRUM} = .82$ to correct for the fraction of the spectrum which is above 300 GeV.

The acceptance factor for the charmed state includes not only geometric efficiency $\epsilon_{\mathrm{GMTRY}}$, but also an efficiency ϵ_{ANS} for all the analysis cuts and an efficiency for the trigger ϵ_{M7}. In practice, the weights of the geometric and analysis efficiencies are determined by Monte Carlo simulation in the form of a single acceptance factor $\epsilon_{\mathrm{SIM}} = \epsilon_{\mathrm{GMTRY}} \cdot \epsilon_{\mathrm{ANS}}$ as a function of either the energy E or the Feynman-x x_f of the state. The analysis cuts are the cuts applied to the data to enhance the signal relative to the background. In my signals, this primarily covers Čerenkov identification requirements or upper multiplicity limits. The geometric efficiency approaches one for high energies because the transverse momentum is essentially constant, thus increasing the longitudinal momentum of a secondary which has the effect of making it fall within a smaller angle (and fall within the detector acceptance). The Čerenkov counters have upper limits on particle identification and this is responsible for the drop in the value of ϵ_{SIM} at high energies. The reliability of the Čerenkov simulation is very important

and is assured by the reproduction of the behavior of the threshold curves shown in chapter 3.

The M7 trigger efficiency ϵ_{M7} for each state is a complicated function of the types of particles present and their energies. A study of the effectiveness of the M7 trigger was performed using Pin 2 events which categorized the probability of accepting an event according to the momentum range and Čerenkov identification of pions and certain "heavies" (kaons and protons). Table B.1 shows the complexity of this efficiency, which was coded up according to the firing probability P_{M7} as a function of the number of tracks falling into the appropriate categories. The efficiency for firing the trigger is assumed independent for each track.

All the above factors result in a description of the cross section for producing any given charmed state as:

$$\sigma_{STATE} = \sigma_{EFFECTIVE} * \frac{N_{OBSERVED} \cdot \epsilon_{MG}}{N_{MG} \cdot \epsilon_{LIVE} \cdot \epsilon_{M7} \cdot \epsilon_{SIM} \cdot \epsilon_{Si33} \cdot \epsilon_{SPECTRUM}} \quad (11)$$

where N refers to the numbers observed or counted. In practice, I absorb $\epsilon_{M7} \cdot \epsilon_{SIM}$ into $N_{OBSERVED}$ to give Y_{STATE}, absorb ϵ_{MG} onto $\sigma_{EFFECTIVE}$, and absorb ϵ_{Si33} into N_{MG}.

$$\sigma_{STATE} = \sigma_{EFFECTIVE}^{\epsilon_{MG}} * \frac{Y_{STATE}}{N_{MG}^{\epsilon_{Si33}} \epsilon_{LIVE} \cdot \epsilon_{SPECTRUM}} \quad (12)$$

Table B.1 Parameterization of M7 efficiency.

5 catagories of particles are considered. The individual firing probabilities are denoted p_i. For events with N_i particles of type i the firing probability is:

$$P_{M7} = 1 - \prod_{i=1,5} (1 - p_i)^{N_i}.$$

i	ISTATL	P RANGE	p_i
1	4	$P > 21GeV$	0.33
2	12	$10 < P < 25GeV$	0.082
3	12	$P > 25GeV$	0.29
4	8	$P > 40GeV$	0.25
5	$\tilde{\pi}^*$	All P	$0.03 + 0.00125 \times N_{\tilde{\pi}}$

* A $\tilde{\pi}$ is any particle other than those in entry $1 \rightarrow 4$

Thus:

$$N_5 = NTBIG - \sum_{i=1,4} N_i.$$

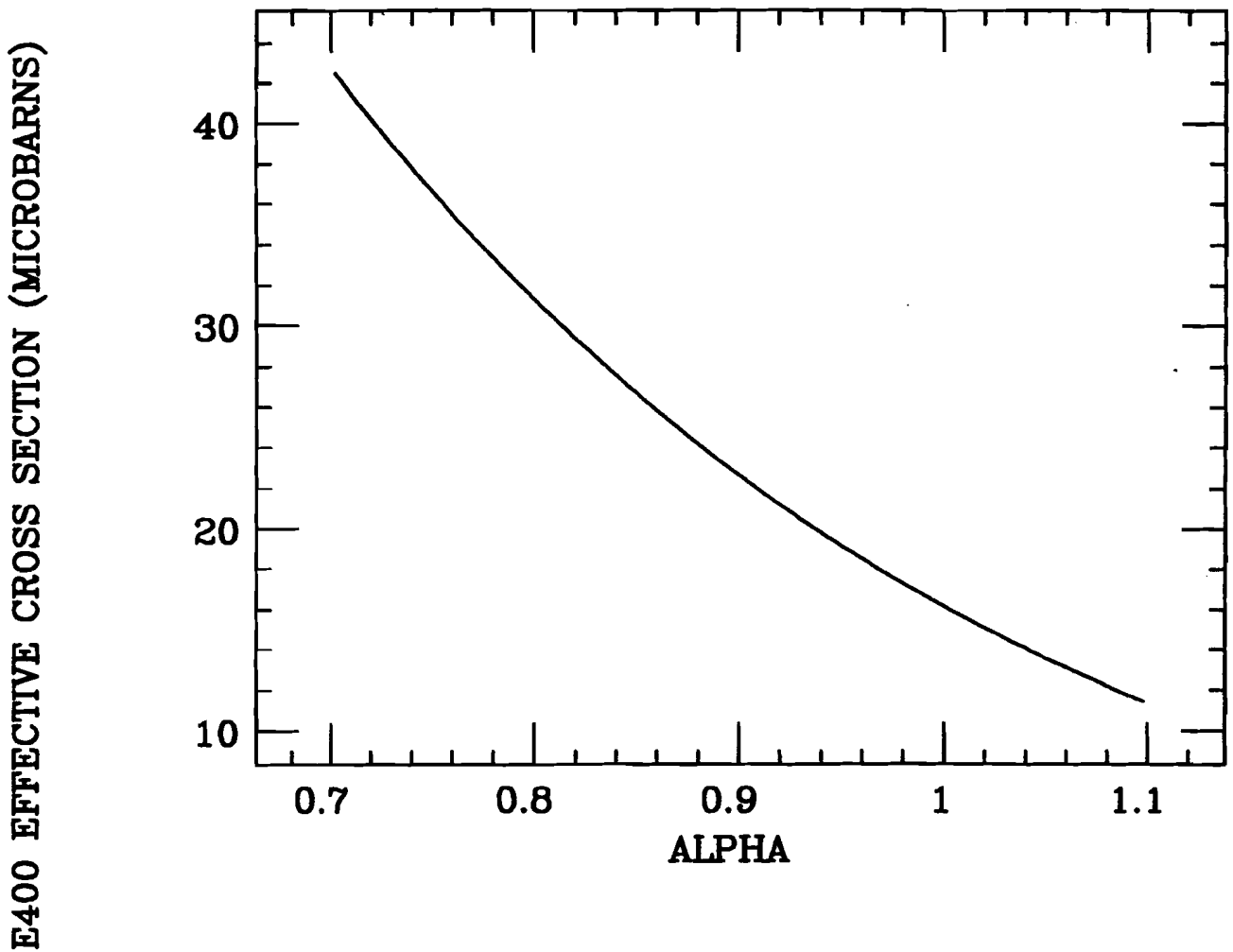

Figure B.1 Variation of cross section with α.

APPENDIX C

Calculation of the $D_s^{\pm}$ Angular Distribution

E400 detected ϕ's by their decay into pairs of oppositely charged kaons, and used this to find the mode $D_s^{\pm} \rightarrow \phi\pi^{\pm}$. Kaons and pions are spin zero particles, but the ϕ is a spin one particle. The D_s is also a spin zero particle. This creates a situation in which there is an angular distribution property of the decay products of the D_s which is not isotropic and can be used therefore to enhance the $D_s^{\pm}$ signal with respect to the background.

Choose a coordinate system in which Z points along the direction of the pion momentum vector in the rest frame of the ϕ. The total angular momentum along this axis is zero because the D_s is a spinless particle. The three possible contributions to angular momentum along the Z axis are the spin of the pion, spin of the ϕ, and their relative orbital angular momentum. The pion is spinless, and so makes no contribution. The orbital angular momentum of the $\phi - \pi$ system is perpendicular to the axis because of the direction of $\vec{R} \times \vec{P}$, so it does not contribute any momentum component to the Z direction. Because the total momentum is zero, the spin of the ϕ cannot contribute either.

Thus the ϕ is in a $l = 1$, $m_z = 0$ state with respect to this Z-axis, so the decay of the ϕ into two kaons gives an angular distribution of the form:

$$\frac{dN}{d\Omega} \propto |Y_1^0|^2 \propto \cos^2(\theta_{K\pi})$$

where $\theta_{K\pi}$ denotes the angle between a pion and kaon in the ϕ rest frame.

REFERENCES

1. B.J. Bjorken and S.L. Glashow, Phys. Lett. **11**, 255 (1984).
2. S.L. Glashow, J. Iliopoulos, and L. Maiani, Phys. Rev. **D2**, 1285 (1970).
3. J.E. Augustin *et al.*, Phys. Rev. Lett. **33**, 1406 (1974).
4. J.J. Aubert *et al.*, Phys. Rev. Lett. **33**, 1404 (1974).
5. G. Goldhaber *et al.*, Phys. Rev. Lett. **37**, 255 (1976).
6. B.L. Combridge, Nucl. Phys. **B151** 429 (1979).
7. L.M. Jones and H.W. Wyld, Phys. Rev. **D17** 1782 (1978).
8. R. Ammar *et al.*, Phys. Lett. **183B** 110 (1987).
9. P. Chauvat *et al.*, submitted to Phys. Lett. **B**.
10. V. Barger and S. Pakvasa, Phys. Rev. Lett. **43**, 812 (1979).
11. L.L.C. Wang and F. Wikczek, Phys. Rev. Lett. **43**, 816 (1979).
12. M. Suzuki, Phys. Rev. Lett. **43**, 818 (1979).
13. H.J. Lipkin, Phys. Rev. Lett. **44**, 710 (1980).
14. J. Cumalat *et al.*, submitted to Phys. Rev. Lett.
15. Xuan-Yem Pham, Phys. Lett. **193B** 331 (1987).
16. PDG, Phys. Lett. **170B** (1986).
17. Tom Kroc, personal communication.
18. G.S. Abrams *et al.*, Phys. Rev. Lett. **43**, 481 (1979).
19. R. M. Baltrusaitis *et al.*, Phys. Rev. Lett. **55**, 150 (1985).
20. A. Chen *et al.*, Phys. Rev. Lett. **51**, 634 (1983).
21. M. Derrick *et al.*, Phys. Rev. Lett. **54**, 2568 (1985).
22. M. Althoff *et al.*, Phys. Lett. **136B**, 130 (1984).
23. H. Albrecht *et al.*, Phys. Lett. **153B**, 343 (1985).
24. R. Bailey *et al.*, Phys. Lett. **139B**, 320 (1984).
25. M. Aguilar-Benitez *et al.*, Phys. Lett. **156B**, 444 (1985).

26. M.J. Lamm, Ph.D. thesis, University of Illinois, Urbana (1983).

27. Discussed at length in many texts; see for instance J.D. Jackson's *Classical Electrodynamics.*

28. P.R. Avery, Ph.D. thesis, University of Illinois, Urbana (1980).

29. R.K. Ellis and C. Quigg, A Pinacoteca of Cross Sections For Hadroproduction of Heavy Quarks, FNAL preprint FN-445/2013.000, January 1987.

30. P. Coteus, *et al.*, Phys. Rev. Lett., **59** 1530 (1987).

31. R. Ammar *et al.*, Phys. Lett. **178B** 124 (1986).

32. M. Macdermott and S. Reucroft, Phys. Lett. **184B** 108 (1987).

33. M. Binkley *et al.*, Phys. Rev. Lett. **34** 1044 (1976).

34. D.S. Barton *et al.*, Experimental Study of the A-Dependence of Inclusive Hadron Fragmentation, Phys. Rev. **D27** 2580 (1983).

35. J. Filaseta, Ph.D. thesis, University of Illinois, Urbana (1987).

36. H. Dijkstra *et al.*, Z. Phys. C **31** 375 (1986).

VITA

Calvin Shipbaugh was born in Huntington, Indiana on August 28, 1958. He attended Huntington North High School, was the recipient of an American Chemical Society award, graduated in May 1976, and received the Bausch and Lomb Medallion for science and math. He entered Rice University in August 1976 as a National Merit Scholar, was selected to teach in the Physics Department's version of the Keller Method *Personalized System of Instruction*, performed a theoretical laser analysis as a senior project, and received a Bachelor of Arts degree in May 1980. He entered the Physics Department at the University of Illinois at Urbana-Champaign in August 1980, held teaching and research assistantships, and received a Master of Science degree in January 1982. Mr. Shipbaugh was accepted in 1986 as a member of the Prometheus Society. In 1987 he joined the American Physical Society, and has co-authored several papers on charm physics.